

LITE AEROSOL RETRIEVALS WITH IMPROVED CALIBRATION  
AND RETRIEVAL APPROACHES IN SUPPORT OF CALIPSO

by

Xiaozhen Wang

---

A Dissertation Submitted to the Faculty of the  
DEPARTMENT OF ELECTRICAL AND COMPUTER ENGINEERING

In Partial Fulfillment of the Requirements  
For the Degree of

DOCTOR OF PHILOSOPHY

In the Graduate College  
THE UNIVERSITY OF ARIZONA

2004

---

UMI Number: 3158165

### INFORMATION TO USERS

The quality of this reproduction is dependent upon the quality of the copy submitted. Broken or indistinct print, colored or poor quality illustrations and photographs, print bleed-through, substandard margins, and improper alignment can adversely affect reproduction.

In the unlikely event that the author did not send a complete manuscript and there are missing pages, these will be noted. Also, if unauthorized copyright material had to be removed, a note will indicate the deletion.

**UMI**<sup>®</sup>

---

UMI Microform 3158165

Copyright 2005 by ProQuest Information and Learning Company.

All rights reserved. This microform edition is protected against unauthorized copying under Title 17, United States Code.

ProQuest Information and Learning Company  
300 North Zeeb Road  
P.O. Box 1346  
Ann Arbor, MI 48106-1346

The University of Arizona ®  
Graduate College

As members of the Final Examination Committee, we certify that we have read the

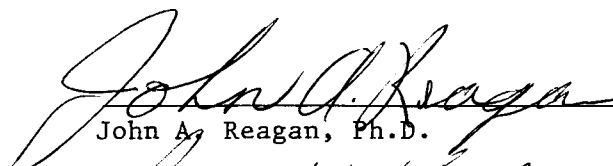
dissertation prepared by Xiaozhen Wang

entitled LITE Aerosol Retrievals with Improved Calibration and

Retrieval Approaches in Support of CALIPSO

and recommend that it be accepted as fulfilling the dissertation requirement for the

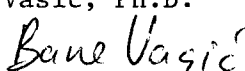
Degree of Doctor of Philosophy

  
John A. Reagan, Ph.D.

7/12/04  
date

  
Raymond K. Kostuk, Ph.D.

7/12/04  
date

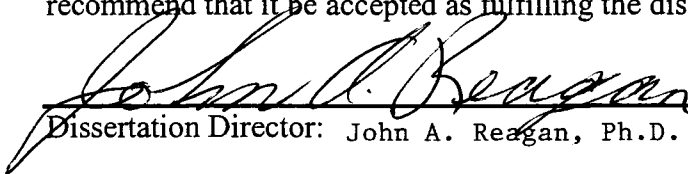
Bane Vasic, Ph.D.  


date  
7/12/04  
date

date

Final approval and acceptance of this dissertation is contingent upon the candidate's submission of the final copies of the dissertation to the Graduate College.

I hereby certify that I have read this dissertation prepared under my direction and recommend that it be accepted as fulfilling the dissertation requirement.

  
Dissertation Director: John A. Reagan, Ph.D.

Nov. 15, 2004  
date

## STATEMENT BY AUTHOR

This dissertation has been submitted in partial fulfillment of requirements for an advanced degree at The University of Arizona and is deposited in the University Library to be made available to borrowers under rules of the Library.

Brief quotations from this dissertation are allowable without special permission, provided that accurate acknowledgment of source is made. Requests for permission for extended quotation from or reproduction of this manuscript in whole or in part may be granted by the head of the major department or the Dean of the Graduate College when in his or her judgment the proposed use of the material is in the interests of scholarship. In all other instances, however, permission must be obtained from the author.

SIGNED: 

## ACKNOWLEDGEMENTS

It hardly seems possible to reach the end of this long process without the support from many others, who have helped me in so many ways.

First of all, I thank my advisor, Dr. John A. Reagan, for his mentoring and support on my research in the Ph.D. program. His insight to scientific research and the way to carry out it have greatly inspired me and will continue to guide me through my career path.

I thank the rest of my dissertation committee: Dr. Raymond Kostuk, Dr. Bane Vasic, Dr. Salim Hariri and Dr. Ralph Martinez for their helpful suggestions and guidance in my study and research.

I am very grateful to my colleagues in NASA Langley Research Center, especially Mary T. Osborn, Kathy Powell, Dr. Dave Winker and Dr. Chris Hostetler for their years of great help and encouragement in my research.

I would like also to thank former and current graduate students in ARSL lab: Hui Fang, for her previous work; Jeremy Dobler, Manuel Rubio, Donna Powell, Anupama Iyengar and Matthew Bolt for their assistance and great discussion during phases of this work.

I'm very indebted to my wife, Yongmei Feng, for her selfless support during the whole course of my Ph.D. study.

This work has been supported by NASA Langley Research Center under contract NAS1-99102.

## TABLE OF CONTENTS

LIST OF FIGURES.....	8
LIST OF TABLES .....	13
ABSTRACT .....	14
<b>1. INTRODUCTION.....</b>	<b>16</b>
1.1 Aerosols in the Atmosphere.....	16
1.2 LIDAR Techniques.....	19
1.2.1 Lidar Calibration at 532/1064 nm.....	25
1.2.2 Cabannes versus Rayleigh Scattering .....	28
1.2.3 Backscatter Ratio for the Terrestrial Atmosphere .....	30
1.2.4 Error Analysis of Aerosol Retrieval .....	31
1.2.5 Two-Wavelength Lidar Aerosol Retrieval Algorithm.....	32
1.2.6 Multiple Scattering Effects in the Lidar Aerosol Retrieval .....	33
1.3 Summary of Contributions .....	35
1.4 Dissertation Organization .....	38
<b>2. LIDAR THEORY AND IMPLEMENTATION.....</b>	<b>40</b>
2.1 Lidar Theory .....	40
2.2 Lidar Equation Solution Approaches.....	42
2.2.1 Two-Type of Scatterers Solution.....	43
2.2.2 One-Type Scatterer Solution .....	46
2.3 Rayleigh Scattering Analysis for Linearly Polarized Light.....	49
2.4 Lidar Technique Implementation .....	54
2.4.1 LITE Mission.....	54
2.4.2 CALIPSO Mission.....	61

## TABLE OF CONTENTS - Continued

3. SPACEBORNE LIDAR CALIBRATION FROM CIRRUS AND MOLECULAR BACKSCATTER RETURNS .....	65
3.1 532 nm Calibration .....	66
3.1.1 Physical Model and Mathematical Description .....	66
3.1.2 LITE Retrieval Results for the 532 nm Calibration Factor.....	70
3.1.3 CALIPSO Simulation Results for the 532 nm Calibration.....	74
3.2 1064 nm Calibration .....	80
3.2.1 Operational 1064 nm Calibration Algorithms .....	80
3.2.2 LITE Retrieval Results for the $C_{1064}/C_{532}$ Calibration Ratio.....	83
3.2.3 1064 nm Channel Calibration for CALIPSO.....	85
3.2.4 Error Analysis of the 1064 nm Calibration Approach.....	88
4. CABANNES VERSUS RAYLEIGH SCATTERING AND TERRESTRIAL BACKSCATTER RATIO REVISITED IN LITE IN SUPPORT OF CALIPSO .....	91
4.1 Spectrum of Light Scattering by Major Species in the Atmosphere .....	92
4.2 Modeling and Analysis of the Depolarization Factor.....	95
4.3 Error Analysis of the Terrestrial Backscatter Ratio in Support of CALIPSO...	101
4.3.1 Error Analysis.....	103
4.3.2 Signal Measurement Error.....	105
4.3.3 Rayleigh Backscattering Coefficient Error.....	108
4.3.4 Errors in the Estimates of $R_{\min}$ .....	109
5. UNCERTAINTY ANALYSIS OF EXTINCTION-TO-BACKSCATTER RATIO IN LITE AEROSOL RETRIEVAL .....	117
5.1 Aerosol Retrieval Uncertainty Analysis .....	117
5.2 Uncertainty Analysis Results and the Investigation of $S_a$ Range .....	120
5.2.1 Saharan Dust Case .....	120

## TABLE OF CONTENTS - Continued

5.2.2 Continental Case.....	124
5.3 Controlled Simulation for the Investigation of the $S_a$ and C Bias Error.....	130
<b>6. SPACEBORNE LIDAR AEROSOL RETRIEVAL APPROACHES BASED ON AEROSOL MODEL CONSTRAINTS .....</b>	<b>138</b>
6.1 A Revised Table-Look up Approach for $S_a$ Selection.....	139
6.2 Lidar Aerosol Retrieval Based on Modeled Constraints .....	142
6.3 Performance Function, Q.....	146
6.4 Results and Discussions.....	147
<b>7. SIMULATION OF MULTIPLE SCATTERING EFFECTS IN AEROSOL RETRIEVALS WITH DIFFERENT APPROACHES .....</b>	<b>153</b>
7.1 A Simple Analytic Algorithm for Aerosol Multiple Scattering Effects .....	154
7.1.1 Aerosol Retrieval Approaches and General Considerations at 532 nm.....	157
7.1.2 Aerosol Retrieval Approaches at 1064 nm.....	161
7.2 Simulation Results and Discussion.....	162
<b>8. CONCLUSIONS AND FUTURE WORK .....</b>	<b>176</b>
8.1 Conclusions.....	176
8.2 Future Work.....	179
<b>REFERENCES.....</b>	<b>181</b>

## LIST OF FIGURES

Fig. 1.1 Aerosol formation sources and relative percentages based on geographic locations. ....	18
Fig. 1.2 The schematic diagram of how the sulfur dioxide gas from a volcanic eruption converts to tiny persistent sulfuric acid ( $H_2SO_4$ ) aerosols. (Graphic by Robert Simmon, Goddard DAAC). ....	18
Fig. 1.3 Example lidar system that was employed for the LITE mission [9]. ....	21
Fig. 2.1 A schematic diagram of the scattering of electromagnetic radiation from a bound electron.....	49
Fig. 2.2 Angular configuration of the scattered electric-field components. ....	51
Fig. 2.3 A cartoon overview of the LITE mission ( <a href="http://www-lite.larc.nasa.gov">http://www-lite.larc.nasa.gov</a> ).....	58
Fig. 2.4.LITE Level 0, version 3 data blocks schematic diagram. ....	60
Fig. 2.5.The formation of CALIPSO satellite with Aura, PARASOL, CloudSat, and Aqua satellites (This image courtesy of Jesse Allen, NASA Earth Observatory).....	62
Fig. 2.6. Lidar block diagram of CALIPSO [71]......	64
Fig. 3.1. A schematic diagram for the relationship between range $r$ and altitude $z$ .....	67
Fig. 3.2 Retrieved 532 nm calibration constant for a portion of LITE orbit 24 based on a 200 shot average spanning about a 1000 km horizontal extent [51].....	72
Fig. 3.3 Retrieved 532 nm calibration constant for portions of LITE orbit 34: (a) based on a 200 shot average spanning about a 1000 km horizontal extent, (b) based on a 1000 shot horizontal average over about half the nighttime portion of orbit 34 and (c) based on a 1000 shot horizontal average for the entire nighttime portion of orbit 34 [51]......	73
Fig. 3.4 Block diagram representing the basic flow of the calibration processes for CALIPSO.....	75
Fig. 3.5. A schematic diagram for demonstrating the implementation of the 532 nm CALIPSO calibration for every 55 km along the night side of the orbit in the 30-34 km region. ....	76
Fig. 3.6. The calculated calibration constant, $C_{532}$ , for CALIPSO with the simulated CALIPSO data (from LITE orbit 34).....	79

## LIST OF FIGURES - Continued

Fig. 3.7. The calculated calibration constant, $C_{532}$ , for CALIPSO with the simulated CALIPSO data (from LITE orbit 103).....	79
Fig. 3.8. Retrieved 1064/532 calibration ratios from selected cirrus cloud returns for (a) orbit 23, (b) orbit 24, and (c) orbit 27 [51]. .....	84
Fig. 3.9. The operational algorithm flo chart for 1064 nm calibration. ....	86
Fig. 3.10. The 1064 nm calibration constant, $C_{1064}$ versus: a) maximum 532 nm cloud scattering ratio; b) altitude of peak 532 nm cloud scattering ratio; c) latitude of calibration cloud profiles for CALIPSO simulation of LITE orbit 23 [74]......	87
Fig. 4.1 Normalized (to unity) relative intensities for the three branches of the depolarized (pure rotational) scattering spectrum of the atmosphere [79]. ....	94
Fig. 4.2 Normalized Cabannes spectrum at 532 nm for the atmosphere at 275 K and 0.75 atm[79]......	94
Fig. 4.3. The modeled relationship between depolarization factor and the receiver filter bandwidth (Center wavelength: $0.5\mu\text{m}$ ). ....	98
Fig. 4.4. The calibration constants at 532 nm for LITE orbit 24 versus latitudes with different depolarization factors. ....	100
Fig. 4.5. The relative deviation of the calibration constants for LITE orbit 24 with different $\delta$ at 532 nm comparing with $C_{532}$ with $\delta = 0.0036$ ......	100
Fig. 4.6. The SNR results from simulation and LITE measurements for 100 shots horizontal average.....	108
Fig. 4.7 Simulation procedure for evaluating the relative uncertainty of $CT^2$ at $z^*$ .....	113
Fig. 4.8. The relationship of $R_{\min}$ versus latitudes with regard to different $S_a$ values for orbit 24. (a) $S_a=25$ ; (b) $S_a=40$ . ....	114
Fig. 4.9. The relationship of $R_{\min}$ versus latitudes with regard to different $S_a$ values for orbit 83, (a) $S_a=25$ ; (b) $S_a=40$ . ....	114
Fig. 4.10. The relationship of $R_{\min}$ versus latitudes with regard to different $S_a$ values for orbit 103, (a) $S_a=25$ ; (b) $S_a=40$ . ....	115
Fig. 4.11. The relationship of $R_{\min}$ versus latitudes with regard to different $S_a$ values for orbit 146, (a) $S_a=25$ ; (b) $S_a=40$ . ....	115
Fig. 5.1. The flight track of orbit 83 during LITE mission in 1994.....	121

## LIST OF FIGURES - Continued

Fig. 5.2. A color image of the Saharan dust structure at different locations. ....	121
Fig. 5.3. Retrieved uncertainties in $\beta_a(z)$ for the Saharan dust layer case due to (a) $\pm$ bias error of C and (b) $\pm$ bias error of $S_a$ . ....	122
Fig. 5.4. Retrieved relative uncertainties (%) in aerosol backscattering coefficients for Sahara dust layer case broken down by sources, which were defined in Eq. (5.3). 123	
Fig. 5.5. Retrieved aerosol extinction profiles at 532 and 1064 nm for orbit 103. ....	127
Fig. 5.6. Solar radiometer measured and LITE retrieved aerosol optical depths vs. latitudes. ....	128
Fig. 5.7. Solar radiometer measured and LITE retrieved aerosol optical depths vs. latitudes. ....	128
Fig. 5.8. Solar radiometer measured and LITE retrieved aerosol optical depths vs. latitudes. ....	129
Fig. 5.9. Solar radiometer measured and LITE retrieved aerosol optical depths vs. latitudes. ....	130
Fig. 5.10. Retrieved aerosol backscattering coefficients with $\tau_a=0.5$ , relative $S_a$ bias error as (a) 15% and (b) 30%. ....	131
Fig. 5.11. Retrieved aerosol extinction coefficients with $\tau_a=0.5$ , relative $S_a$ bias error as (a) 15% and (b) 30%. ....	132
Fig. 5.12. Aerosol retrieval results with $\tau_a=0.5$ , relative C bias error as 4.4%. ....	133
Fig. 5.13. Retrieved aerosol backscattering coefficients with $\tau_a=0.2$ , relative $S_a$ bias error as (a) 15% and (b) 30%. ....	135
Fig. 5.14. Retrieved aerosol extinction coefficients with $\tau_a=0.2$ , relative $S_a$ bias error as (a) 15% and (b) 30%. ....	135
Fig. 5.15. Aerosol retrieval results with $\tau_a=0.2$ , relative C bias error as 4.4%. ....	136
Fig. 6.1. Map of the AERONET sites used by Cattrall et al. in their study. Oceanic sites are represented by an 'X' [56]. ....	141
Fig. 6.2. Colored image of the Saharan dust layer from LITE orbit 83. ....	143
Fig. 6.3. Colored image of the smoke layer for biomass burning from LITE orbit 146. ....	143

## LIST OF FIGURES - Continued

Fig. 6.4. Colored image of the boundary layer for urban/industrial from LITE orbit 103. .....	144
Fig. 6.5. Colored image of the marine boundary layer (MBL) from LITE orbit 83.....	145
Fig. 6.6. Retrieved aerosol backscattering coefficient ratios of 532/1064 nm for Dust (spheroids), Biomass Burning and Urban/Industrial models.....	148
Fig. 6.7. Retrieved aerosol extinction coefficient ratios of 532/1064 nm for Dust (spheroids), Biomass Burning and Urban/Industrial models.....	148
Fig. 6.8. Retrieved aerosol backscattering coefficient ratios of 532/1064 nm for Dust (spheroids), Oceanic and Urban/Industrial models.....	149
Fig. 6.9. Retrieved aerosol extinction coefficient ratios of 532/1064 nm for Dust (spheroids), Oceanic and Urban/Industrial models.....	149
Fig. 6.10. Simulation results of performance function for Biomass Burning, Urban/Industrial, Dust (spheroids) and Oceanic models. ....	150
Fig. 7.1 A schematic diagram of the multiple scattering effect for a spaceborne lidar. .	154
Fig. 7.2. The modeled LITE $\eta$ values for elevated dust layer model with $\sigma_a=0.2/\text{km}$ and $0.6/\text{km}$ respectively at 532 nm [95]. ....	156
Fig. 7.3. The modeled CALIPSO $\eta$ values for elevated dust layer model with $\sigma_a=0.2/\text{km}$ and $0.6/\text{km}$ respectively at 532 nm [95].....	156
Fig. 7.4. A schematic flow chart of Self/Auxiliary-Transmittance approach at 532 nm.	160
Fig. 7.5. The averaged relative retrieval uncertainties versus $\eta$ for elevated aerosol layer model at 532 nm ( $\tau_a = 0.5$ ), (a) $\Delta S_a/S_a$ vs. $\eta$ (b) $\Delta\sigma_a/\sigma_a$ vs. $\eta$ (c) $\Delta\beta_a/\beta_a$ vs. $\eta$ . ....	163
Fig. 7.6. The averaged relative retrieval uncertainties versus $\tau_a$ for elevated aerosol layer model at 532 nm ( $\eta = 0.7$ ), (a) $\Delta S_a/S_a$ vs. $\tau_a$ (b) $\Delta\sigma_a/\sigma_a$ vs. $\tau_a$ (c) $\Delta\beta_a/\beta_a$ vs. $\tau_a$ . ....	164
Fig. 7.7. The averaged relative retrieval uncertainties versus $\eta$ at 1064 nm for (a) elevated aerosol layer model ( $\tau_a = 0.5$ ), (b) boundary layer model ( $\tau_a = 0.2$ ). ....	165
Fig. 7.8 The averaged relative retrieval uncertainties versus $\tau_a$ at 1064 nm for (a) elevated aerosol layer model ( $\eta=0.7$ ), (b) boundary layer model ( $\eta=0.7$ ).....	166

## LIST OF FIGURES - Continued

Fig. 7.9. Retrieved aerosol extinction and backscattering profiles from simulated single and multiple scattering signals ( $\eta=0.7$ and $\tau_a=0.5$ at 532 nm, elevated layer model). .....	167
Fig. 7.10. Retrieved aerosol extinction and backscattering profiles from simulated single and multiple scattering signals ( $\eta=0.7$ and $\tau_a=0.2$ at 532 nm, boundary layer model). .....	167
Fig. 7.11. Retrieved aerosol extinction and backscattering profiles from simulated single and multiple scattering signals ( $\eta=0.7$ and $\tau_a=0.5$ at 1064 nm, elevated layer model). .....	168
Fig. 7.12. Retrieved aerosol extinction and backscattering profiles from simulated single and multiple scattering signals ( $\eta=0.7$ and $\tau_a=0.2$ at 1064 nm, boundary layer model). .....	168
Fig. 7.13. The correctional relations for $S_a$ , $\sigma(r)$ and $\beta(r)$ with known $\eta$ for the elevated aerosol layer model at 532 nm ( $\tau_a=0.5$ ). .....	171
Fig. 7.14. The correctional relations for $S_a$ , $\sigma(r)$ and $\beta(r)$ with known $\eta$ for the aerosol boundary layer model at 1064 nm ( $\tau_a=0.2$ ). .....	172
Fig. 7.15. Retrieved aerosol extinction profiles from LITE and simulated single scattering signals. .....	174

## LIST OF TABLES

Table 2.1. LITE system parameters [10] .....	56
Table 2.2. Level 1 data parameters for each laser shot profile .....	59
Table 2.3. The instrumentation specifications of CALIPSO ( <a href="http://www-calipso.larc.nasa.gov">http://www-calipso.larc.nasa.gov</a> ).....	63
Table 3.1 Uncertainty estimates of the 532 nm calibration constant and related parameters. ....	71
Table 3.2. The spatial resolution of CALIPSO simulated data.....	75
Table 3.3 Calibration ratio $C_{1064}/C_{532}$ for LITE orbits 23, 24 and 27 .....	85
Table 3.4. Calculated 1064 nm calibration constant using CALIPSO simulated data. ....	88
Table 3.5 Uncertainty estimates of the 1064 nm calibration constant and related parameters. ....	90
Table 4.1. The relative uncertainties of $R_{\min}(z^*)$ , $X(z^*)$ , $\beta_R(z^*)$ and $CT^2(z^*)$ with $S_a = 25$ and 40.....	116
Table 6.1 Summary of lidar parameters retrieved from selected AERONET sites [56]..	141

## ABSTRACT

Two of the biggest uncertainties in understanding and predicting climate change are the effects of aerosols and clouds. NASA's satellite mission, CALIPSO (Cloud-Aerosol Lidar and Infrared Pathfinder Satellite Observations), will provide vertical, curtain-like images of the atmosphere on a global scale and assist scientists in better determining how aerosols and clouds affect the Earth's radiation budget. The data from a previous space shuttle mission, LITE (Lidar In-space Technology Experiment, launched in Sept., 1994), have been employed to develop algorithms (e.g., spaceborne lidar system calibration and aerosol retrievals) in support of CALIPSO.

In this work, a new calibration approach for 1064 nm lidar channel has been developed via comparisons of the 532 nm and 1064 nm backscatter signals from cirrus clouds. Some modeling analyses and simulations have also been implemented for CALIPSO's narrow bandwidth receiver filter to quantitatively distinguish Cabannes scattering from the full bandwidth Rayleigh scattering and correct the calibration of 532 nm channel. LITE data were also employed in some analyses with the aim of recovering the estimates of the backscatter ratio,  $R$ , of clean air regions. The uncertainties in aerosol retrieval due to different error sources, especially the bias and random errors of the extinction-to-backscatter ratio,  $S_a$ , have been investigated. A revised  $S_a$  table look-up approach is incorporated with two notable revisions for improved  $S_a$  selection, which, as a consequence enable more bounded aerosol retrievals. Approximate but quantitatively useful multiple-scattering corrections are reported using a modeled multiple scattering

factor,  $\eta$ , which approximates the reduced attenuation caused by multiple scattering. Assessment of multiple scattering effects for a reasonable range of  $\eta$  values is included for a combination of retrieval approaches.

## 1. INTRODUCTION

### 1.1 Aerosols in the Atmosphere

According to the US National Academy of Sciences, the Earth's surface temperature has risen by about 1 degree Fahrenheit in the past century, with accelerated warming during the past two decades (<http://yosemite.epa.gov/oar/globalwarming.nsf>). From reports of increasing temperatures, thinning mountain glaciers and rising sea level, scientists know that Earth's climate is changing (<http://earthobservatory.nasa.gov>). Even though it is undisputed that human activities have altered the chemical composition of the atmosphere through the buildup of "greenhouse" gases – primarily carbon dioxide, methane, and nitrous oxide, uncertainties exist about exactly how earth's climate responds to them (<http://yosemite.epa.gov/oar/globalwarming.nsf>). Two of the biggest uncertainties in understanding and predicting climate change are the effects of clouds and aerosols (<http://earthobservatory.nasa.gov>).

Scientists have developed mathematical representations of natural processes, climate models, to simulate many features of the climate and make predictions about climate. While they are invaluable tools, they are still not accurate enough to provide reliable forecasts of how the climate may change; and the several models often yield contradictory results. Clouds and aerosols are important variables in these models. How they help cool and warm the Earth, how they interact with each other and how human activities will change them and their effect on the climate in the future have motivated researchers to explore these questions for decades.

Aerosols are tiny particles suspended in the air. They can be either solid or liquid particles, which can be characterized by several physical properties, such as chemical composition and method of production, size distribution, and temporal and spatial variability. Aerosols range in size from about 0.01 microns to several tens of microns. For example, cigarette smoke particles are in the middle of this size range and typical cloud drops are 10 or more microns in diameter. Some aerosols occur naturally, originating from volcanoes, dust storms, forest and grassland fires, living vegetation, and sea spray. Another source of aerosol is human activities, such as the burning of fossil fuels and the alteration of natural surface cover. Fig. 1.1 shows the aerosol formation sources and their relative percentages based on geographic locations (<http://earthobservatory.nasa.gov>).

Normally, the majority of aerosols form a thin haze in the troposphere (troposphere - the lowest part of the atmosphere, which is below 10~15 km), where they are washed out of the air by rain within about a week. Aerosols are also found in a part of the atmosphere just above the troposphere (called the "stratosphere", a region owing its characteristics to its rather isothermal vertical temperature distribution and ozone content). A severe volcanic eruption, such as Mount Pinatubo in the Philippines in 1991, can put large amounts of aerosol into the stratosphere. Since it does not rain in the stratosphere, these aerosols can remain there for many months, producing beautiful sunsets around the globe, and possibly causing summer temperatures to be cooler than normal. Scientists estimate that Mount Pinatubo injected about 20 million tons of sulfur dioxide into the atmosphere, cooling average global temperatures over the following year

by about half a degree (<http://earthobservatory.nasa.gov>). Fig. 1.2 shows how the sulfur dioxide ( $\text{SO}_2$ ) gas from a volcanic eruption converts to tiny persistent sulfuric acid ( $\text{H}_2\text{SO}_4$ ) aerosols. A broader and more accurate description of various aerosol species and their physical properties may be found in standard references [1].

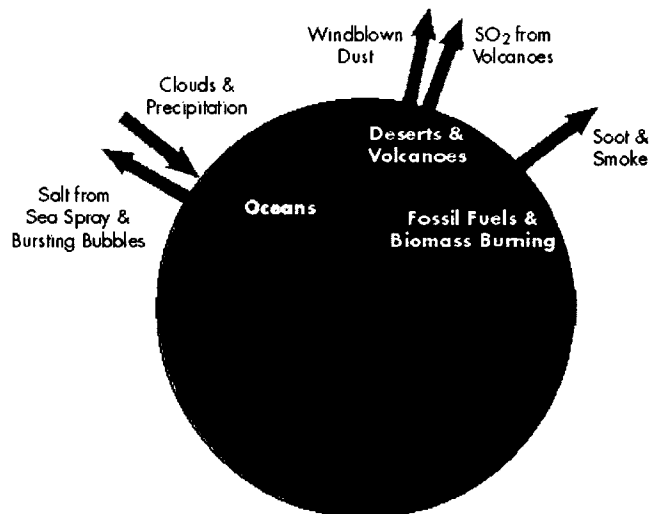


Fig. 1.1 Aerosol formation sources and relative percentages based on geographic locations.

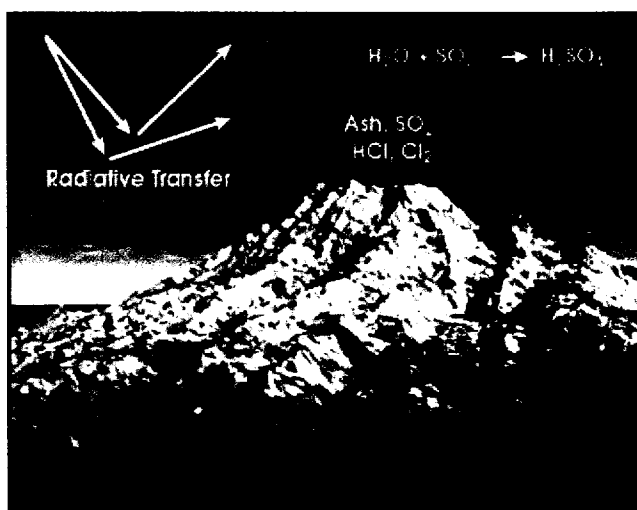


Fig. 1.2 The schematic diagram of how the sulfur dioxide gas from a volcanic eruption converts to tiny persistent sulfuric acid ( $\text{H}_2\text{SO}_4$ ) aerosols. (Graphic by Robert Simmon, Goddard DAAC).

## 1.2 LIDAR Techniques

The acronym lidar stands for LIght Detection And Ranging, which was applied first [2] to pulsed "white light" ceilometers in 1930s. With the discovery of pulsed lasers, lidar was almost immediately employed as an atmospheric probe. As an extension of meteorological radars into visual region of the electromagnetic spectrum, lidar sometimes is also called laser radar. About forty years ago, the appearance of the giant-pulse (Q-switched) solid state lasers in the commercial market made it possible to optically probe the atmosphere with previously unknown sensitivity and resolution. Compared to radar, lidar has a much shorter wavelength range, which provided the opportunity for sensing atmospheric constituents and properties to which radar was insensitive. Most importantly, lidar offered the capability for sensing scattering by both air molecules and aerosol particles. The great potential of lidar was recognized very quickly [3]. In 1963, G.Fiocco and co-workers [4, 5] first reported experimental application of lidar at MIT. In their application, a ruby lidar was employed in attempts to detect high altitude aerosol layers in the stratosphere and mesosphere. At about the same time, some experiments using a ruby lidar to probe the lower troposphere were performed at Stanford Research Institute by Ligda [6]. He and his co-workers reported [7, 8] that aerosol scattering features could frequently be related to changes in thermal stability and air motion in the atmosphere, as in the case of aerosol stratification near temperature inversions.

In the years that followed, there have been many significant advances in the theory and practice of lidar sensing. Increased interest in environmental monitoring and concern over possible changes in climate due to increased aerosol loading of the

atmosphere fueled much of the lidar research through the latter part of the 1960s and well into the 1970s. Reagan et al. [9] has given a very complete review and summary of the development and application of lidar sensing techniques. They also offered comments regarding the future outlook for aerosol and cloud sensing by both ground-based and spaceborne lidar.

The operating principle of lidar is analogous to pulsed microwave radar. The only difference is that lidar uses optical rather than microwave components to direct, intercept, and detect the emitted lidar radiation. A major component of a typical lidar system is a pulsed laser source such as a Q-switched ruby, neodymium doped glass (Nd: YAG) or dye laser, which transmits light pulses into the atmosphere. Typically, the duration of the pulses is about 20 nanoseconds (ns). The pulses have energies ranging from a few millijoules (mJ) to several joules depending on the type and size of the laser. Repetition frequencies range from ~0.1 Hz to several kilohertz, varying more or less inversely with pulse energy, so that average powers are generally less than 10 W [9].

Another important component of a lidar system is an optical telescope mounted adjacent to the laser, which is used to intercept backscattered echoes from scatterers in the path of the transmitted pulses. The telescopes collect the light and focus it onto a photodetector such as a photomultiplier which yields an electronic signal proportional to the received light flux (power). The electronic signals generated by the transient detector responses are sampled, digitized, and stored and/or displayed graphically versus time (A-scope presentation). The relationship between time,  $t$ , and the scattering range,  $r$ , can be expressed as  $r = ct/2$  where  $c$  is the velocity of light and  $t$  is the elapsed time since the

transmitted laser pulse left the transmitter. Fig. 1.3 shows an example lidar system, which was employed for the LITE shuttle mission [10]. Several aspects of the LITE mission and measurements will be discussed in Chapter 2.

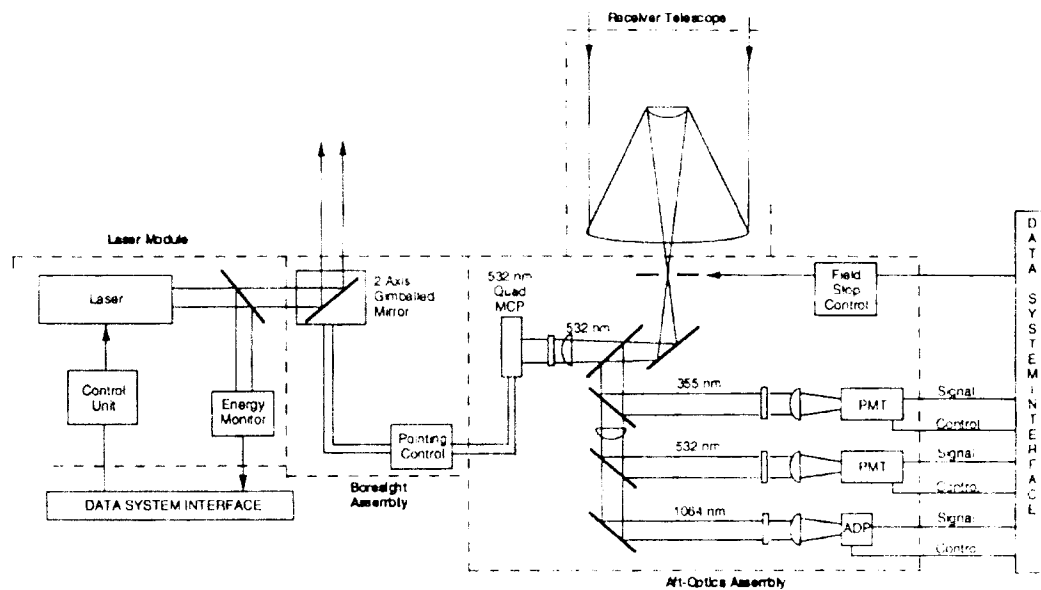


Fig. 1.3 Example lidar system that was employed for the LITE mission [9].

For an aerosol lidar, there are two points which should be considered for selecting the operating wavelength. Firstly, the atmospheric gaseous spectral absorption regions should be avoided. Secondly, a wavelength should be picked that is long enough so that the aerosol scattering signal is not too small comparing to the molecular (Rayleigh) scattering signal.

In most cases, aerosol lidar systems only employ one laser operating at one or two wavelengths. Frequency doublers and triplers provide ways for generating additional wavelengths. The main factor in determining the lidar operating wavelength is the availability of laser sources. The ruby laser was the first available giant pulse (Q-

switched) laser for early lidar systems. In recent years, the Nd: YAG laser has become the most widely used laser for aerosol lidar due to its improved efficiency and reliability.

Another important component in a lidar system is the lidar receiver, which serves chiefly as a "photon bucket" in the case of aerosol lidar. The requirement for coherence/spectral purity is relatively crude for this simple elastic scatter application. But the receiver in the High Spectral Resolution Lidar (HRSL) approach [11, 12] can be one exception. With the HRSL approach, the aerosol and molecular scattering contributions are separated on the basis of the much wider Doppler broadening of the molecular signal. Thus, a wide variety of optical collectors, which range from astronomical quality telescopes to simple plastic Fresnel lens and revamped searchlight reflector systems, have been used for lidar receivers.

In many cases, separate transmitting and receiving optics are used in a lidar system, thereby yielding a noncoaxial system with parallex. Thus, the overlap range, the distance over which the single scatter echoes are not received until the transmitted pulse crosses into the receiver field-of-view, must be taken into consideration. The overlap generally occurs within a few hundred meters to a kilometer for typical transmitter divergences and receiver fields-of-view (a few milliradians). To avoid near range signal saturation of the photodetector, the overlap range may be purposely extended for long-range probing applications, such as stratospheric sounding lidars. Recently, more and more lidars use a common primary element for both transmitter and receiver. But overlap still occurs for co-axial systems; e.g., MPL's (micro-pulse lidar).

Some other important components, such as narrow-band interference filters (~0.2 to 2 nm) and mechanical shutters, may also be included in the lidar receiver system to reduce background radiation and protect detector from being saturated. Without using extremely narrow bandwidth filtering in the receiver, the daytime lidar ranging distances are generally rather limited due to strong background radiation.

Typically, there are two detectors of choice for an aerosol lidar, photomultipliers and avalanche photodiodes. The former offers fast response and high gain coupled with fairly good quantum efficiency and relatively low noise levels, even at or near room temperature. This makes photomultipliers the preferable choice for most of the wavelengths used in aerosol lidar. However, photomultipliers have poor quantum efficiencies at longer wavelengths, which makes it very inefficient to operate at the Nd:YAG fundamental wavelength (1064 nm). The alternative is the avalanche photodiode which offers a viable detector choice at this wavelength for probing in the lower troposphere. The aerosol scattering in the lower troposphere is generally strong enough so that the inherent detector "avalanche" noise is not a problem. But the avalanche noise can become unacceptably large compared to the lidar signal in the upper troposphere and stratosphere due to both very small aerosol scattering and a larger ranging distance. Most Nd:YAG based lidars operate at the frequency doubled second harmonic (532 nm) or use the second harmonic to pump dye lasers that operate at wavelengths less than about 800 nm, thereby permitting the use of more efficient and less noisy detectors.

Finally, for the purpose of doing further signal processing with the received lidar signal, a series of operations must be performed on the raw photodetector output.

Sampling and digitizing are two typical signal processing techniques for handling the transient signal response to each transmitted lidar pulse. The higher the desired spatial resolution, the faster the required sampling rate. As mentioned before, maximum achievable resolution is set by the limit of half the transmitted pulse length, as with pulsed radar. But for the purpose of limiting the noise bandwidth, the bandwidth of the post-detection electronics is generally too low to achieve this maximum resolution limit. Typically, the sampling rate is on the order of one sample per 100 ns (15 m resolution). With this spatial resolution, two thousand samples are required to achieve a ranging distance of 30 km. The minimum number of bits required for each sample is 8 to 10 bits, and even higher resolution may be appropriate for high accuracy requirements. However, the large dynamic range typically exhibited by a lidar signal over a distance of 10 km or more requires a gain compression amplifier, such as a log amp or a gain-switching amp, between the detector and the transient digitizer, even if a higher bit-resolution digitizer is employed.

One typical approach to improve the signal-to-noise ratio is to average the digitized signals for each transmitted lidar pulse over many pulses. For this reason, a large number of digitized records must be saved in data storage, and an on-line computer is needed to perform averaging and other housekeeping tasks associated with the operation of a lidar system. In the following subsections, a literature review for the research topics in this dissertation will be introduced based on various aspects of the lidar techniques.

### 1.2.1 Lidar Calibration at 532/1064 nm

Following radar practice, the lidar response may be quantitatively interpreted in terms of the lidar range equation. The instantaneous received power,  $P(r)$ , due to backscattering from range,  $r$ , assuming only single scattering and a vertically pointing lidar, may be expressed in the form [9]

$$P(r) = P_o Y(r) \frac{ct_p}{2} \cdot \frac{A_r}{z^2} \beta(r) T^2(r) \quad (1.1)$$

or

$$P(r) = cE_o Y(r) A_r \beta(r) T^2(r) / 2r^2 \quad (1.2)$$

where

$P_o$  = transmitted peak power

$r$  = the range between lidar and the target

$Y(r)$  = geometry factor for overlap of transmitter/receiver beam paths

$ct_p$  = transmitted pulse length; pulse duration  $t_p$  times speed of light  $c$

$E_o$  = transmitted pulse energy; product of  $P_o t_p$

$A_r/r^2$  = solid angle (sr) subtended by receiver aperture  $A_r$  at range  $r$

$\beta(r)$  = unit volume backscattering coefficient ( $m^{-1}sr^{-1}$ ) of the atmosphere at range  $r$

$T^2(r)$  = round-trip transmittance and from range  $r$ .

$$\text{Also, } T^2(r) = e^{-2 \int_0^r \sigma(r') dr'} \quad (1.3)$$

where  $\sigma(r)$  is the unit volume extinction or attenuation coefficient ( $m^{-1}$ ) of the atmosphere at range  $r$ .

Scattering and extinction are due to the combined effects of Rayleigh (molecular) and aerosol scattering. With a simple superposition of the two independent scattering constituents, molecular scattering and aerosol scattering,  $\beta(r)$  may be resolved as

$$\beta(r) = \beta_R(r) + \beta_a(r) \quad (1.4)$$

where  $\beta_R(r)$  and  $\beta_a(r)$  are the Rayleigh (molecular) and aerosol backscattering coefficients, respectively. Similarly,  $\sigma(r)$  may be expressed as

$$\sigma(r) = \sigma_R(r) + \sigma_a(r) \quad (1.5)$$

The Rayleigh and aerosol extinction-to-backscatter ratio,  $S_R$  and  $S_a$  can be written as

$$S_R = \frac{\sigma_R(r)}{\beta_R(r)} \quad (1.6)$$

and 
$$S_a = \frac{\sigma_a(r)}{\beta_a(r)} \quad (1.7)$$

Photodetection and post-detection amplification of the received power yields the lidar response output signal  $V(r)$ , proportional to  $P(r)$ . For ranges beyond complete overlap of the transmitter receiver beam paths, the working form of the lidar equation becomes

$$V(r) = \frac{CE_o\beta(r)T^2(r)}{r^2} \quad (1.8)$$

where  $C$  is the lidar system calibration factor.

A lidar system must be calibrated very accurately to enable quantitative measurements of aerosol scattering properties in the atmosphere. However, lidar systems are inherently difficult to calibrate. Hall and Ageno [13] described the calibration of their

system, using a standard target, and this approach was also successfully employed by Reagan et al. [14]

Barret and Ben-Dov analyzed the lidar returns from clear skies [15] and introduced a molecular (Rayleigh) scattering background calibration procedure. But their calibration procedure was highly uncertain because they simply assumed that the return from approximately 100 m above the ground surface was dominated by molecular scattering over the particulate scatterers at that level, which generally is not the case. However, the calibration obtained by normalizing to a nearly molecular scattering signal at higher altitude (i.e., 30 to 34 km above the ground) is quite feasible.

For a spaceborne lidar system, changes of system gain/efficiency can be expected to occur during the course of a shuttle or satellite mission. It is essential to employ a calibration approach that can be implemented on-orbit, preferably repeatable at least a few times per orbit. For wavelengths less than about 550 nm, in situ calibration can be accomplished via normalization to high altitude, nearly molecular scattering regions [16]. However, for longer wavelengths beyond about 800 nm, particularly the popular Nd:YAG fundamental wavelength at 1064 nm, the Rayleigh normalization approach becomes questionable due to both an inherently weaker signal and a stronger, variable and somewhat unknown aerosol scattering contribution. For lidars operating at both longer and shorter wavelengths, a viable approach is to retrieve the longer wavelength calibrations ratioed to the shorter wavelength calibrations via comparisons of spectral backscatter from known/quantifiable scatterers. If lidar ground returns can be obtained from surfaces of known reflectance, this can also be used for calibrating longer

wavelength lidars. For example, a calibration study for 1064 nm via the surface return approach has been reported by Reagan, Liu and Cooley [17-19].

### 1.2.2 Cabannes versus Rayleigh Scattering

In the application of lidar in atmosphere remote sensing, the returned signal usually consists of Rayleigh scattering and vibrational Raman scattering from molecules as well as Mie scattering from aerosol and clouds. Depending on the filter bandwidth of the lidar receiver, the shifted pure rotational Raman scattering signal may or may not be included in the measured lidar return signal.

The concept of Rayleigh scattering was often misinterpreted as molecular scattering in many lidar applications, which has been pointed out in a series of articles by Young [20-23]. An accurate estimate of the amount of Rayleigh scattering in the terrestrial atmosphere is required in both lidar calibration and lidar aerosol retrieval applications. The parameters that characterize this type of scattering are well defined (e.g., by McCartney [24]) and the general relationship to calculate the total Rayleigh-scattering cross section per molecule has been widely reported [25, 26]. However, it has also been reported that the Rayleigh optical depth determined by various sources can vary by as much as 3-4% depending on the values of the index of refraction and the depolarization factor assumed for air[27]. In order to clarify the confusion that arose a few years ago when an incorrect value for the depolarization factor was used in computations of the Rayleigh optical depth [20], a brief historical review is listed chronologically.

In 1957, Penndorf [28] first published tabular values of the refractive index of standard air and the Rayleigh-scattering coefficients for the 0.2-20.0  $\mu\text{m}$  wavelength range. He used Edlen's [29] formula for the index of refraction and a constant value of 0.035 for the depolarization factor to calculate the Rayleigh-scattering cross section, the Rayleigh mass-scattering coefficient, and the Rayleigh volume-scattering coefficient as a function of wavelength. With the U.S. Standard Atmosphere (1962) data [30], Eltermann [31, 32] extended Penndorf's [28] research by tabulating values of the Rayleigh volume-scattering coefficient and the Rayleigh optical depth as a function of wavelength (0.27-4.0 $\mu\text{m}$ ) and altitude (0-50 km). Edlen's [29] formula for the refractive index of air was also used in Eltermann's calculation as well as the value of 0.035 for the depolarization factor.

In the years that followed, the work of many researchers involving Rayleigh scattering parameters can be traced back to Penndorf [28] or Eltermann [31, 32], (e.g., Margraff and Griggs [33] used a least-squares fit to Eltermann's [31] optical depth data in 1969). McCartney listed Penndorf's [28] Rayleigh scattering coefficient and refractive-index values in his book [24] in 1976. The series of LOWTRAN atmospheric transmittance-radiance models developed by Kneizys *et al.* [34-36] all use some form of least-squares fit to Penndorf's [28] Rayleigh volume-scattering coefficients in their calculations from 1980 to 1988.

Using Edlen's formula for the index of refraction and a constant value of 0.0139 for the depolarization factor, Hoyt [37] reported values of the Rayleigh optical depth as a function of wavelength (0.3-1.5  $\mu\text{m}$ ) for six standard atmospheres (U.S. Standard

Atmosphere supplement, 1966 [38]). Frolich and Shaw [39] used updated depolarization data, giving a value of 0.0095, and Edlen's [40] refractive-index formula for their tabulated values of the Rayleigh optical depth, which is a function of wavelength (0.26 - 1.5  $\mu\text{m}$ ) for five standard atmospheres [38] models. However, the depolarization factor used by Hoyt [37] and Frolich and Shaw [39] deviated from the true value because their measurements excluded the effects of the Raman-scattered lines and, therefore, did not completely represent the depolarization factor for Rayleigh scattering [20-23]. This resulted in optical parameter values that were a few percent lower. Based on the latest measurements, Young [21] recommended a value of 0.0279 for the depolarization factor, which applied for unpolarized incident light.

### 1.2.3 Backscatter Ratio for the Terrestrial Atmosphere

Accurate retrieval of aerosol properties requires the minimization of overall errors and uncertainties in the LITE measurements and the data analysis process. It is important, therefore, to study the sources of error and to establish accurate models for these errors. These uncertainties depend upon a number of factors, including the lidar system parameters, the background light, the aerosol types, the accuracy, resolution, and proximity of the nearest molecular density measurement, the validity of lidar calibration procedures, and the uncertainty in the upper atmospheric transmission profile at the lidar location.

The calibration obtained by normalizing to a nearly Rayleigh background signal depends on the backscatter ratio,  $R$ , defined as the ratio of the total backscattering

coefficient [aerosol backscattering coefficient,  $\beta_a(r)$ , plus molecular backscattering coefficient,  $\beta_m(r)$ ] to the molecular backscattering coefficient,  $\beta_m(r)$ . How well this backscatter ratio,  $R$ , can be estimated in clean air regions will play an important role in lidar measurement of aerosol and cloud. The LITE mission [10], which was the first lidar designed for atmospheric studies to fly in the Earth orbit, provided an important database for doing the analysis and simulations for the coming CALIPSO mission. It seems appropriate, therefore, that the Rayleigh-scattering parameters (i.e., the Rayleigh-scattering cross section, volume-scattering coefficient, and optical depth) should be updated by the use of the latest estimates of the depolarization factor.

#### 1.2.4 Error Analysis of Aerosol Retrieval

In lidar aerosol retrievals, there are four significant error/uncertainty sources: (1) lidar signal; (2) molecular density; (3) lidar calibration; and (4) assumption for the aerosol extinction-to-backscatter coefficient,  $S_a$ . Once the noise models for the error sources which affect the LITE measurements and calibration are established, the sensitivity of the aerosol retrievals to the various errors and uncertainties can be modeled and analyzed. Russell et al. [16] have extensively discussed and evaluated the major error sources affecting retrieval of the aerosol backscattering coefficient. For their treatment of the two types of scatterer atmosphere (i.e., both molecular and aerosol scattering important), they assumed the total relative error in the retrieved backscattering coefficient had contributions from the signal measurement error, the range error, the two-way transmission error, the molecular-density error, and the error in the assumed value of

$R_{\min}$ . However, the uncertainty in the aerosol extinction-to-backscatter ratio,  $S_a$ , which is usually known either poorly or not at all, was not included.

### 1.2.5 Two-Wavelength Lidar Aerosol Retrieval Algorithm

An evaluation scheme for a two-wavelength lidar aerosol retrieval was presented by Potter [41], who developed an iterative procedure for determination of the aerosol transmission along the lidar path from the information content for the two Nd: YAG wavelengths (1064- and 532-nm). This algorithm is for a one-component (i.e., aerosol scattering only) atmosphere with two assumptions: (1) the ratio of the extinction-to-backscatter is constant (2) the ratio of the extinction coefficients at the two wavelengths is independent of the position along the lidar line, namely, the ratio is a constant too. This aerosol transmission can be used to solve the boundary value problem of the lidar equation.

The iterative approach of Potter was expanded by Ackermann to two component (i.e., aerosol and air molecule scattering) atmospheres assuming the ratio between the extinction coefficients of both wavelengths is constant along the lidar path [42-44].

An analytical solution for  $T_{a,532}^2(r_1 \rightarrow r_2)$ , the aerosol layer round-trip transmission at 532 nm between the lidar-to-target distance  $r_1$  and  $r_2$  ( $r_1 < r_2$ ), is introduced by Ackermann [44]. With this solution, the corresponding aerosol extinction coefficients at 532 nm,  $\sigma_{a,532}(r)$ , and the ratio of aerosol extinction coefficients at 1064 nm and 532 nm,  $\gamma$ , can also be obtained with only the lidar signals at these two wavelengths.

In practice, however, because of the noise inherent to each measurement and possibly unknown variations of  $\gamma$  and the aerosol extinction-to-backscatter ratio,  $S_a$ , along the lidar line, more than three ranges were needed by Ackermann's approach to obtain a reliable estimate for  $T_{a,532}^2(r_1 \rightarrow r_2)$ . Thus, despite the analytical solution given by Ackermann, the two-wavelength lidar inversion must be considered as a statistical approach for the boundary value determination [44].

### 1.2.6 Multiple Scattering Effects in the Lidar Aerosol Retrieval

Scattering from transmitted lidar pulses by particles and molecules in the atmosphere provides the means to probe the optical properties and the spatial distribution of these scatterers. The optical properties of particles in the atmosphere can be determined by the analysis of the temporal variation of the scattered light flux measured by the lidar receive, generally with the first order assumption that only single scattering is important. However, it is also possible for light to be multiply scattered before it is measured at the receiver when the particle number density is large, or for certain lidar geometries. In such cases, the data collected by lidar can, when analyzed based on the single scattering theory, lead to wrong conclusions.

The Monte Carlo method has been used by many researchers to obtain an accurate estimate of the temporal variation of light pulses multiply scattered backward to a lidar receiver [45-50]. A number of studies [51-54] have shown that in addition to the particle scattering characteristics (angular scattering distribution, extinction coefficient, etc.), the degree of multiple scatter for turbid media is primarily determined by the field of view

(FOV) of the lidar receiver. Besides the receiver FOV factor, Spinhirne also reported that lidar multiple scattering is a function of the receiver-to-scattering medium range [54], a significant factor for spaceborne lidar. He pointed out that for a given receiver FOV, an increase in the receiver range can result in a significant increase in the multiply scattered signal.

For spaceborne lidar measurements, the geometrical configuration is very different from that for airborne or ground-based measurements. As a result of the much larger distance between the lidar and the observed layer, the volume inside the cone of the receiver field-of view (FOV) is also larger. Thus, for spaceborne lidar measurements, there is a higher possibility for the photons which are scattered in a sideward direction to again experience another scattering event inside the cone, and be scattered back to the detector, than for ground-based or airborne lidar measurements. Multiple scattering can then be expected to play an important role in. Using a representative aerosol model, Spinhirne [54] showed that for spaceborne lidar measurements even for clear atmospheric conditions (i.e., only weak aerosol loading and no clouds), multiple scattering is not negligible. The effect of multiple scattering can be notably reduced by employing a much smaller FOV lidar receiver than that typical of ground-based and airborne lidar systems.

While the Monte Carlo method has become more and more efficient with improvements in implementation techniques [50], solutions of the lidar problem by means of the Monte Carlo method are still time consuming and impractical for a variety of physical situations. Some analytical solutions [44, 48] have also been reported for analyzing lidar data obtained in clouds, fogs, or haze, but analytical solutions are often

quite complicated or still rely partially on the Monte Carlo method to generate the specified lidar signals [55].

To first order, lidar multiple scattering effects can be modeled with an effective aerosol extinction-to-backscatter ratio  $S_a^* = \eta S_a$ , where  $\eta$  is a multiple scattering factor less than 1 (i.e., reduces extinction to account for enhanced scattering in forward direction:  $\sigma_a^*(r) = \eta S_a \beta_a(r)$ ). The effects of multiple scattering can be estimated for different assumed values of  $\eta$  to assess the impact of multiple scattering on different aerosol retrieval approaches.

### 1.3 Summary of Contributions

Overall, the main contribution of the research reported here is the development of some simulation-based approaches for the lidar calibration, aerosol retrieval, aerosol retrieval error analysis and multiple scattering corrections to the aerosol retrievals.

In this dissertation, a cirrus spectral backscatter ratio calibration approach for 1064 nm is reported for application during the CALIPSO and GLAS (Geoscience Laser Altimeter System) missions. The molecular normalization calibration approach for 532 nm is also reviewed, including results obtained from case studies of lidar data collected during the LITE shuttle mission. Attention is focused on developing a simple, autonomous approach applicable to satellite lidar missions such as CALIPSO.

The lidar system for the CALIPSO mission will use a very narrow-bandwidth filter in the lidar receiver, which is very close to the bandwidth of Cabannes scattering. The impact upon the lidar calibration at 532 nm by using of the wrong depolarization

factor, (e.g., 0.0279), is discussed and assessed. The spectral structure of molecular scattering (strength and bandwidth) and its constituent spectra associated with Rayleigh and vibrational Raman scattering has been reviewed to characterize these constituent contributions versus bandwidth, including development of a modeled relationship between the receiver filter bandwidth and the depolarization factor. The Rayleigh/Cabannes scattering cross sections that should apply for CALIPSO were calculated by incorporating different depolarization factors appropriate for different spectral bandwidths. These results enable determination of the molecular scattering components that can be expected to pass through the CALIPSO narrow-bandwidth receiver filter.

Additionally, LITE data were analyzed to recover the estimates of  $R$  characteristics that take into account uncertainties in the assumed calibration constant determined at higher altitude (e.g. ~30 km above ground). The relative uncertainties of the calibration constant at 532 nm and the two-way transmission at the calibration reference height were modeled and assessed.

In order to estimate various uncertainties in the retrieved aerosol backscattering coefficient, simulations have been presented to assess and analyze the sensitivity of the retrievals of the aerosol backscattering coefficient caused by the use of an inaccurate assumed extinction-to-backscattering coefficient,  $S_a$ , calibration factor,  $C$ , normalized signal,  $X(r)$ , and Rayleigh backscattering profile,  $\beta_R(z)$ . The range of  $S_a$  values estimated for LITE orbits 24 and 103 were also investigated by using revised calibration

approaches and solar radiometer measured optical depths at 532 nm and 1064 nm [19, 51].

Aerosol retrievals at 532 nm for the current GLAS and upcoming CALIPSO satellite lidar missions employ/will employ a look-up table approach to select climatologically based  $S_a$  model values for these retrievals when alternate, less uncertain methods for either defining  $S_a$  or providing the needed auxiliary information are unavailable. A spaceborne lidar aerosol retrieval approach based on aerosol model constraints is presented, which incorporates two notable revisions for improved  $S_a$  selection [56]. One is a refined, more bounded set of  $S_a$  values, both for 532 nm and 1064 nm, representative of a definitive set of aerosol types/models determined from an extensive analysis of the AERONET data base [57]. The other is an accompanying set of key spectral ratio parameters (i.e., dual wavelength, 532 nm to 1064 nm, ratios of backscatter, extinction and  $S_a$ ) also derived from the AERONET data which offer additional ways to bound the lidar aerosol retrievals. Thus, aerosol retrievals can be obtained subject to the constraints that the lidar data yield retrievals with spectral ratio parameters consistent with a given aerosol model (or models), to confirm the model choice and better bound the retrievals.

Approximate, but quantitatively useful multiple-scattering corrections are presented in this dissertation by making use of a multiple-scattering factor  $\eta$  [50], which reduces the aerosol extinction-to-backscatter ratio,  $S_a$ , to an effective value  $S_a^* = \eta S_a$ . This accounts for the first order effect of multiple scattering on the lidar signal, namely, reduction in the apparent atmospheric attenuation due to added scattering in the forward

direction. Assessment of multiple scattering effects for a reasonable range of  $\eta$  values and a combination of retrieval methods is addressed, using simulated multiple and single scattering signals for 532 and 1064 nm.

## 1.4 Dissertation Organization

In what follows, Chapter 2 presents the basic lidar theory and some derivations of solutions to the lidar equation. Two spaceborne lidar missions, LITE and CALIPSO, are also briefly introduced in this chapter. These missions serve as the motivation and test-beds for the lidar technique developments, assessments and implementations presented in this dissertation. Chapter 3 introduces a viable calibration ratio approach to overcome the difficulty in implementing the Rayleigh normalization approach at longer wavelengths beyond 800 nm. In Chapter 4, some modeling analyses and simulations are implemented for CALIPSO to quantitatively distinguish Cabannes scattering from the full bandwidth Rayleigh scattering, and to correct the calibration of the 532 nm channel based on Rayleigh normalization. In addition, LITE data are employed to do some analysis, which aims at recovering estimates of the backscatter ratio,  $R$ , of clean air regions. Chapter 5 addresses the error analysis of aerosol retrievals due to different error sources, and Chapter 6 addresses a revised table look-up approach that incorporates two notable revisions for improved  $S_a$  selection, which, as a consequence, enable more bounded aerosol retrievals. In Chapter 7, an assessment of multiple scattering effects is presented including some first-order retrieval correction approaches, based on modeling lidar

multiple scattering via the reduced extinction multiple scattering factor,  $\eta$ . Finally, conclusions are drawn in Chapter 8.

## 2. LIDAR THEORY AND IMPLEMENTATION

### 2.1 Lidar Theory

The instantaneous received power,  $P(r)$ , due to backscattering from range,  $r$ , assuming only single scattering and a vertically pointing lidar, has been described in Chapter 1 by (1.1). Photodetection and post-detection amplification yields the lidar response output signal,  $V(r)$ , which is proportional to the received power,  $P(r)$ , and can be expressed by (1.8). Equations (1.1) and (1.8) are based on the single scattering approximation that is quite valid for most atmospheric conditions. But for scattering within clouds, fogs and severe hazes, and for certain lidar geometries, multiple scattering effects must be taken into consideration.

The transmission or attenuation factor  $T(r)$  in (1.1) follows the Beer-Lambert law and can be expressed as

$$T(r) = e^{-\tau(r)} \quad (2.1)$$

or

$$T(r) = e^{-\int_0^r \sigma(r') dr'} \quad (2.2)$$

where  $\tau(r)$  is the atmospheric optical depth through range  $r$  and  $\sigma(r')$  is the atmospheric unit volume extinction coefficient ( $\text{m}^{-1}$ ) at any intervening range  $r'$  between 0 and  $r$ . The extinction coefficient includes the loss effects of both scattering and absorption. The backscattered signal is produced by the interaction between the constituents in the atmosphere and the transmitted lidar pulse. The constituents in the atmosphere include

the gaseous air molecules and aerosol particles. Molecules scatter light rather weakly due to their small size, producing Rayleigh scattering that varies inversely with the fourth power of wavelength of the incident radiation. Compared with molecules, atmospheric aerosol particles [58] strongly scatter/diffract light due to their polydisperse characteristics and wide particle size range (~0.01 to several micrometers), which spans the lidar wavelength range. The aerosol particles strongly scatter/diffract light producing what is generally approximated as Mie scattering after the generalized spherical particle scattering theory developed by G.Mie [59, 60]. At a given lidar wavelength, the molecular scattering contribution, which varies directly with the atmospheric molecular number density, can be predicted rather accurately if temperature sounding data for the time and place in question are available. In contrast, it is virtually impossible to exactly predict the expected aerosol scattering contribution to a given lidar signal due to uncertainty in the aerosol properties (e.g., size distribution and indices of refraction of the aerosol particles), which are highly variable with place and time. From (2.1) and (2.2), one then obtains

$$T(r) = T_R(r)T_a(r) \quad (2.3)$$

where

$$T_R(r) = e^{-\tau_R(r)} = e^{-\int_0^r \sigma_R(r') dr'} \quad (2.4)$$

and

$$T_a(r) = e^{-\tau_a(r)} = e^{-\int_0^r \sigma_a(r') dr'} \quad (2.5)$$

Again, the 'R' and 'a' subscripts denote the Rayleigh and aerosol contributions, respectively. Thus, the expression (1.8) can be rewritten as

$$V(r) = \frac{CE_o[\beta_R(r) + \beta_a(r)]}{r^2} \cdot \exp\left[-2 \int_0^r \{\sigma_R(r') + \sigma_a(r')\} dr'\right] \quad (2.6)$$

The general lidar equation is often expressed in a normalized form

$$X(r) = C\beta(r)T^2(r) \quad (2.7)$$

where  $\beta(r)T^2(r)$  is referred to as attenuated backscatter (i.e., the backscatter at  $r$  modulated by the roundtrip transmittance to range  $r$ ),  $X(r) = V(r)r^2 / E_o$ , because  $r^2$  and  $E_o$  (at least on a relative basis) can usually be normalized out of the lidar equation with very high accuracy.

## 2.2 Lidar Equation Solution Approaches

In equation (2.6), the system calibration factor  $C$  can be assumed to be known/determined. The Rayleigh terms  $\beta_R(r)$  and  $\sigma_R(r)$  may be theoretically determined from the Rayleigh scattering law and knowledge of the atmospheric temperature and pressure profiles over the observation site (e.g.,[22],[28]). But there are still two unknowns,  $\beta_a(r)$  and  $\sigma_a(r)$ , remaining in the equation based on only one measurement,  $V(r)$ , at each range  $r$ . The only way to solve this problem is to include certain assumptions and/or constraints in the solution procedure. Assuming that the aerosol extinction-to-backscatter ratio,  $S_a = \sigma_a/\beta_a$ , can be known beforehand or some supplementary data are available so that  $S_a$  can be one of the outputs of the data analysis, the lidar equation will be solvable. There had been various successful solution methods,

which were based on this assumption, developed during the past decades [15, 61-67]. Only some of these approaches, related to the topics addressed in this dissertation, will be described in the following subsections.

### 2.2.1 Two-Type of Scatterers Solution

In 1972, Fernald et al. [67] presented a solution formulation including both molecular and aerosol scattering. One assumption of this solution is that the aerosol extinction-to-backscatter ratio,  $S_a = \sigma_a/\beta_a$ , is constant with range.

From (2.5), this yields,

$$T_a^2(r) = e^{-2 \int_0^r \sigma_a(r') dr'} = e^{-2 \int_0^r S_a \beta_a(r') dr'} \quad (2.8)$$

From which,

$$\frac{dT_a^2(r)}{dr} = T_a^2(r) \cdot (-2S_a) \beta_a(r) \quad (2.9)$$

and

$$\beta_a(r) = -\frac{1}{2S_a T_a^2(r)} \frac{dT_a^2(r)}{dr} \quad (2.10)$$

Substituting (2.10) into (2.7), yields

$$X(r) = C \left[ \beta_R(r) - \frac{1}{2S_a T_a^2(r)} \frac{dT_a^2(r)}{dr} \right] T_a^2(r) T_R^2(r) \quad (2.11)$$

Hence, (2.11) can be generalized to a linear differential equation,

$$\frac{dT_a^2(r)}{dr} - 2S_a \beta_R(r) T_a^2(r) = -\frac{2S_a X(r)}{C T_R^2(r)} \quad (2.12)$$

Equation (2.12) can be solved for  $T_a^2(r)$  as

$$T_a^2(r) = e^{-\int_0^r [-2S_a\beta_R(r')]dr'} \left\{ \int_0^r e^{\int_0^{r'} -2S_a\beta_R(r'')dr''} \left[ -\frac{2S_a X(r')}{CT_R^2(r')} \right] dr' + 1 \right\} \quad (2.13)$$

where  $S_R=8\pi/3$  and  $\int_0^r \beta_R(r)dr = \int_0^r \sigma_R(r)/S_R dr = \frac{3}{8\pi} \int_0^r \sigma_R(r)dr$

Equation (2.13) can be written as

$$T_a^2(r) = T_R(r)^{-3S_a/4\pi} \left[ 1 - \frac{2S_a}{C} \int_0^r X(r')T_R(r')^{(3S_a/4\pi-2)} dr' \right] \quad (2.14)$$

Substituting (2.14) into (2.7), yields

$$\beta_a(r) = \frac{X(r)}{CT_a^2(r)T_R^2(r)} - \beta_R(r) \quad (2.15)$$

Combining (2.14) and (2.15) produces

$$\beta_a(r) = \frac{X(r)T_R(r)^{\frac{3S_a}{4\pi}-2}}{C \left[ 1 - \frac{2S_a}{C} \int_0^r X(r')T_R(r')^{(3S_a/4\pi-2)} dr' \right]} - \beta_R(r) \quad (2.16)$$

and

$$T_R(r)^{\frac{3S_a}{4\pi}-2} = \exp \left[ -2(S_a - S_R) \int_0^r \beta_R(r')dr' \right] \quad (2.17)$$

Finally, (2.16) can be written as

$$\beta_a(r) = \frac{X(r) \exp \left[ -2(S_a - S_R) \int_0^r \beta_R(r')dr' \right]}{C - 2S_a \int_0^r X(r') \exp \left[ -2(S_a - S_R) \int_0^{r'} \beta_R(r'')dr'' \right] dr'} - \beta_R(r) \quad (2.18)$$

For a spaceborne downlooking (nadir) lidar system operating at 532 nm, calibration for the 532 nm channel may be performed at a reference range,  $r_c$ , which is selected via normalization to a high altitude, nearly molecular scattering regions. The

relationship between range  $r$  and the corresponding altitude above the ground  $z$  is  $r = z_L - z$ , where  $z_L$  is the altitude of the spaceborne lidar system, (e.g., for CALIPSO, it is about 705 km). The reference calibration range is also the starting point of the aerosol retrieval for a downlooking lidar system.

The new quantities

$$\Phi(r') = -2S_a\beta(r') \quad (2.19)$$

and

$$\Psi(r') = e^{-\int_0^{r'} 2S_a\beta_R(r'')dr''} \left[ -\frac{2S_aX(r')}{CT_R^2(r')} \right] \quad (2.20)$$

are now introduced to simplify the notation of (2.13). This enables the two-way aerosol transmittance at  $r_c$  ( $0 < r_c < r$ ) to be expressed by

$$T_a^2(r_c) = e^{-\int_0^{r_c} \Phi(r')dr'} \left\{ \int_0^{r_c} \Psi(r')dr' + 1 \right\} \quad (2.21)$$

and

$$T_a^2(r) = e^{-\int_{r_c}^r \Phi(r')dr'} \left[ T_a^2(r_c) + e^{-\int_0^{r_c} \Phi(r')dr'} \int_{r_c}^r \Psi(r')dr' \right] \quad (2.22)$$

$$e^{-\int_{r_c}^r \Phi(r')dr'} = T_R^{-\frac{3S_a}{4\pi}}(r) T_R^{\frac{3S_a}{4\pi}}(r_c) \quad (2.23)$$

$$e^{-\int_0^{r_c} \Phi(r')dr'} = T_R^{-\frac{3S_a}{4\pi}}(r_c) \quad (2.24)$$

Equation (2.22) then becomes

$$T_a^2(r) = T_R^{-\frac{3S_a}{4\pi}}(r) T_R^{\frac{3S_a}{4\pi}}(r_c) \left[ T_a^2(r_c) + T_R^{-\frac{3S_a}{4\pi}}(r_c) \int_{r_c}^r T_R^{\frac{3S_a}{4\pi}-2}(r') \cdot \frac{-2S_aX(r')}{C} dr' \right] \quad (2.25)$$

where

$$T_R^{\frac{3S_a-2}{4\pi}}(r') = T_R^{\frac{3S_a-2}{4\pi}}(r_c) \exp\left[\int_{r_c}^{r'} -2(S_a - S_R) \beta_R(r') dr'\right] \quad (2.26)$$

Substituting (2.25) and (2.26) into (2.15) yields

$$\beta_a(r) = \frac{X(r) \exp\left[-2(S_a - S_R) \int_{r_c}^r \beta_R(r') dr'\right]}{CT^2(r_c) - 2S_a \int_{r_c}^r X(r') \exp\left[-2(S_a - S_R) \int_{r_c}^{r'} \beta_R(r'') dr''\right] dr'} - \beta_R(r) \quad (2.27)$$

Equations (2.18) and (2.27) are the general equations for solving the two-type scatterer problems. Profiles of  $\beta_a(r)$  and  $\sigma_a(r)$  can be retrieved given an a priori estimate of  $S_a$  or an estimate of  $T_a^2(r)$  at some reference range,  $r_c$ .

## 2.2.2 One-Type Scatterer Solution

When the extinction coefficient,  $\sigma(r)$ , at a reference range,  $r_{ref}$ , is used as an input, a stable solution to the single scattering lidar equation may be obtained as presented by Klett [66]. In Klett's solution, the aerosol scattering was assumed to be dominant and

$$\beta_a(r) = B\sigma_a^k(r) \quad (2.28)$$

where B and k are constants. Typically, k is set to unity, which is identical to assuming the aerosol extinction to backscatter ratio,  $S_a$ , is a constant. Klett's solution is a backward solution, which allows the retrieval of  $\sigma(r)$  through range  $r < r_{ref}$ , given by

$$\sigma(r) = \frac{\left[X(r)/X(r_{ref})\right]^{1/k}}{\sigma(r_{ref})^{-1} + \frac{2}{k} \int_r^{r_{ref}} \left[X(r')/X(r_{ref})\right]^{1/k} dr'} \quad (2.29)$$

where  $r_{ref}$  is the farthest range. One advantage of this backward regression solution is that fairly accurate retrievals of  $\sigma(r)$  can be obtained for rather crude estimates of  $\sigma(r_{ref})$  so

long as  $T(r_{\text{ref}})$  is small (i.e., for turbid conditions). However,  $\sigma(r_{\text{ref}})$  must be estimated fairly accurately to obtain good estimates of  $\sigma(r)$  for values of  $T(r_{\text{ref}})$  close to unity. It is important to recognize that the stability and boundary value sensitivity of various solutions to the lidar equation can vary greatly depending upon atmospheric turbidity and the spatial location of the boundary value [9, 65, 66, 68, 69]. The transmittance boundary condition is more likely what one will have from auxiliary measurements, and the direct use of an assumed  $S_a$  is also another likely solution approach. Due to above-mentioned reasons, the one-type scatterer solution in this dissertation is based on the approaches given by Fernald et al. [67].

When aerosol scattering is dominant, the normalized backscattering signal can be expressed as

$$X(r) = C\beta_a(r)T_a^2(r) \quad (2.30)$$

From (2.9), this yields

$$\frac{dT_a^2(r)}{dr} = T_a^2(r) \cdot (-2S_a)\beta_a(r) \quad (2.31)$$

Combining (2.30) and (2.31), yields

$$dT_a^2(r) = \frac{X(r)}{C} \cdot (-2S_a)dr \quad (2.32)$$

Integrating both sides of (2.32) from  $r_1$  to  $r_2$ , one obtains

$$T_a^2(r_2) - T_a^2(r_1) = - \int_{r_1}^{r_2} \frac{2S_a}{C} X(r)dr \quad (2.33)$$

and

$$T_a^2(r_1 \rightarrow r_2) - 1 = -\frac{1}{T_a^2(r_1)} \int_{r_1}^{r_2} \frac{2S_a}{C} X(r) dr \quad (2.34)$$

where  $T_a^2(r_1 \rightarrow r_2) = T_a^2(r_2)/T_a^2(r_1)$ . Finally, we can also obtain the relation

$$\frac{CT_a^2(r_1)}{S_a} = \frac{2 \int_{r_1}^{r_2} X(r) dr}{1 - T_a^2(r_1 \rightarrow r_2)} \quad (2.35)$$

If the integration range of (2.32) is from  $r_1$  to  $r$ , then

$$T_a^2(r) - T_a^2(r_1) = -\int_{r_1}^r \frac{2S_a}{C} X(r) dr \quad (2.36)$$

Substituting (2.36) back into (2.30), yields

$$\beta_a(r) = \frac{X(r)}{C \left[ T_a^2(r_1) - \int_{r_1}^r \frac{2S_a}{C} X(r) dr \right]} \quad (2.37)$$

Based on (2.37) and  $\sigma_a(r) = S_a \beta_a(r)$ , one obtains

$$\sigma_a(r) = \frac{X(r)}{\frac{CT_a^2(r_1)}{S_a} - 2 \int_{r_1}^r X(r) dr} \quad (2.38)$$

Substituting (2.35) into (2.38), yields

$$\sigma_a(r) = \frac{X(r)}{\frac{2 \int_{r_1}^{r_2} X(r) dr}{1 - T_a^2(r_1 \rightarrow r_2)} - 2 \int_{r_1}^r X(r) dr} \quad (2.39)$$

Equations (2.38) and (2.39) are the general equations for the one-type scatterer solution.

In addition, from (2.38) and (2.39),  $S_a$  can be expressed as

$$S_a = \frac{CT_a^2(r_1) [1 - T_a^2(r_1 \rightarrow r_2)]}{2 \int_{r_1}^{r_2} X(r) dr} \quad (2.40)$$

### 2.3 Rayleigh Scattering Analysis for Linearly Polarized Light

As shown in Fig. 2.1, when a plane, linearly polarized monochromatic wave propagates in the  $z$ -direction with its plane of polarization at an angle  $\phi$  to the  $y$ -axis, a dipole moment in the molecules (or atoms) in its path will be induced by the electric-field component of this wave. This dipole moment will then radiate into  $4\pi$  steradians and this reemission of electromagnetic radiation can be interpreted as a form of elastic scattering of the incident wave [70]. Before and after this elastic scattering, the wavelength is the same. One simplified model is to consider a single molecular (or atom) with only one valence electron (i.e. only one electron that is bound weakly enough to be influenced by the applied field) located at the origin of the coordinate system shown in Fig. 2.1.

Assuming that this molecule or atom can be treated as a classical harmonic oscillator, the electron's equation of motion in terms of its displacement from its equilibrium position (at the origin)  $\chi$  takes the form

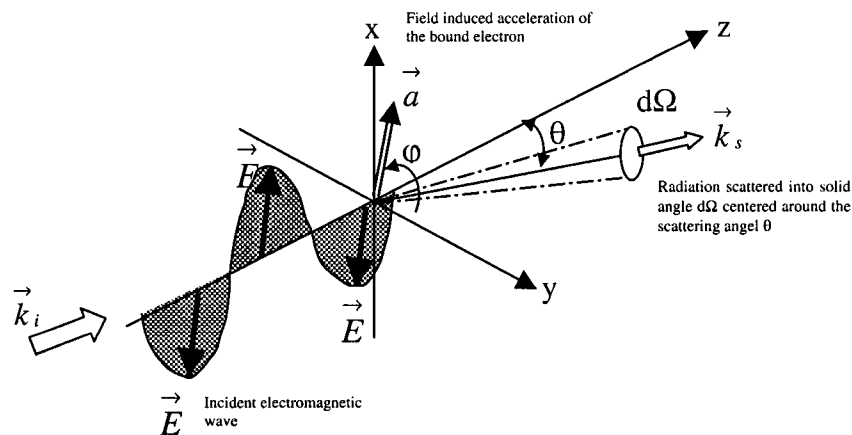


Fig. 2.1 A schematic diagram of the scattering of electromagnetic radiation from a bound electron.

$$\ddot{\vec{\chi}} + \alpha \dot{\vec{\chi}} + \omega_0^2 \vec{\chi} = -\frac{e}{m_e} \vec{E} \quad (2.41)$$

where  $\omega_0$  represents the resonant angular frequency of the electron and  $\alpha$  the damping constant. The electric field  $\vec{E}$  for the incident wave can be expressed in terms of its angular frequency  $\omega$  and a unit polarization vector  $\vec{\xi}$ :

$$\vec{E} = \vec{\xi} E_0 e^{-j\omega t} \quad (2.42)$$

A harmonic steady-state solution for (2.41) is of the form

$$\vec{\chi} = \vec{\xi} \chi_0 e^{-j\omega t} \quad (2.43)$$

and the induced acceleration of the bound electron is

$$\vec{a} = \ddot{\vec{\chi}} = -\left[ \frac{\omega^2}{\omega_0^2 - \omega^2 - j\omega\alpha} \right] \frac{e}{m_e} \vec{E} \quad (2.44)$$

At position  $R(r, \theta)$ , the radiated component of the electric field produced by this accelerating electron can be divided into two components:

$$\vec{E}_1^s = -\frac{e}{4\pi\epsilon_0 c^2 r} \vec{a}_1 \quad (2.45)$$

and

$$\vec{E}_2^s = -\frac{e}{4\pi\epsilon_0 c^2 r} \vec{a}_2 \quad (2.46)$$

where  $\vec{a}_1$  and  $\vec{a}_2$  are the perpendicular components of acceleration in the plane perpendicular to the direction of scattering  $\vec{k}_s$ .  $\theta$  is the angle between the incident and

scattering directions in the scattering (yz) plane and  $\varphi$  is referred to as the polarization angle.  $\hat{k}_i$  and  $\hat{k}_s$  are unit vectors in the incident and scattered directions, respectively.

As shown in Fig. 2.2, the amplitudes of the perpendicular components,  $\vec{a}_1$  and  $\vec{a}_2$ , can be expressed as

$$a_1 = a \sin \varphi \quad \text{and} \quad a_2 = a \cos \varphi \cos \theta \quad (2.47)$$

and from (2.45) and (2.46), the scattered field at position  $R(r, \theta)$  is

$$\vec{E}_s = \vec{E}_1^s + \vec{E}_2^s = -\frac{ea}{4\pi\epsilon_0 c^2 r} [\hat{a}_2 \cos \theta \cos \varphi + \hat{a}_1 \sin \varphi] \quad (2.48)$$

where  $\epsilon_0$  is the vacuum permittivity,  $-e$  is the electron's charge and  $\hat{a}_2$  and  $\hat{a}_1$  represent unit vectors in the  $\vec{a}_2$  and  $\vec{a}_1$  directions.

The power radiated into the solid angle  $d\Omega$  can be expressed in the form

$$dP(\theta, \varphi) = \frac{1}{2} \epsilon_0 c |E_s|^2 r^2 d\Omega \quad (2.49)$$

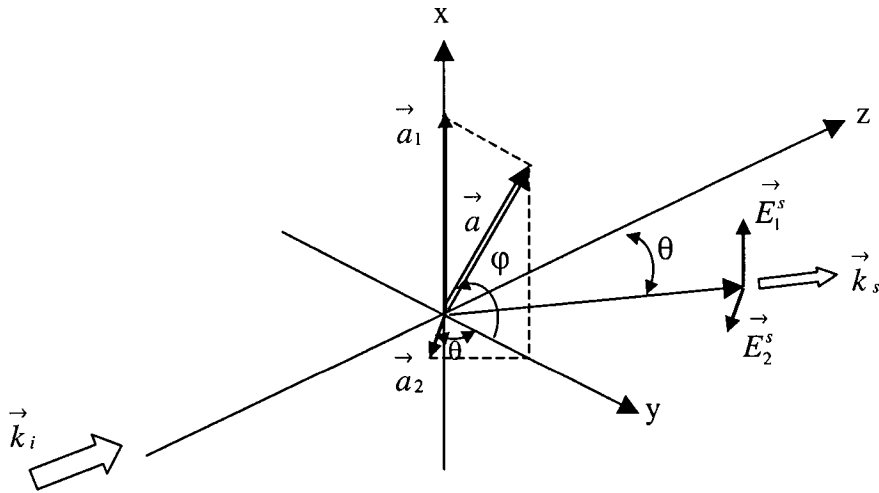


Fig. 2.2 Angular configuration of the scattered electric-field components.

Substituting (2.48) into (2.49), the scattered power radiated per unit solid angle can be expressed as

$$\frac{dP(\theta, \varphi)}{d\Omega} = \frac{e^2 a^2}{2^5 \pi^2 \epsilon_0 c^3} [\cos^2 \varphi \cos^2 \theta + \sin^2 \varphi] \quad (2.50)$$

where  $|\vec{E}_s|^2 = |\vec{E}_1^s|^2 + |\vec{E}_2^s|^2$  and the orthogonality between  $\hat{a}_1$  and  $\hat{a}_2$  has been employed.

Substituting (2.42) in (2.44) and (2.44) into (2.50), (2.50) can be rewritten as

$$\frac{dP(\theta, \varphi)}{d\Omega} = \frac{1}{2} \epsilon_0 c |E_0|^2 r_e^2 \left[ \frac{\omega^2}{\omega_0^2 - \omega^2 - j\omega\alpha} \right] [\cos^2 \varphi \cos^2 \theta + \sin^2 \varphi] \quad (2.51)$$

where  $r_e = \frac{e^2}{4\pi\epsilon_0 m_e c^2}$  is the electron classical radius

By introducing the differential scattering cross section of an individual molecule or atom,  $d\sigma/d\Omega$ , the scattered power radiated per unit solid angle can be expressed as

$$\frac{dP(\theta, \varphi)}{d\Omega} = I_0 \frac{d\sigma(\theta, \varphi)}{d\Omega} \quad (2.52)$$

where

$$\frac{d\sigma(\theta, \varphi)}{d\Omega} = r_e^2 \left[ \frac{\omega^2}{\omega_0^2 - \omega^2 - i\omega\alpha} \right]^2 [\cos^2 \varphi \cos^2 \theta + \sin^2 \varphi] \quad (2.53)$$

and  $I_0 = \frac{1}{2} \epsilon_0 c |E_0|^2$  represents the incident irradiance.

It is reasonable to assume that  $\omega_0 + \omega \approx 2\omega$  at optical frequencies and consequently,

$$\frac{d\sigma(\theta, \varphi)}{d\Omega} \approx \frac{1}{4} r_e^2 \left[ \frac{\omega^2}{(\omega_0 - \omega)^2 + (\alpha/2)^2} \right] [\cos^2 \varphi \cos^2 \theta + \sin^2 \varphi] \quad (2.54)$$

From (2.54) a total Rayleigh scattering cross section per isolated molecule (or atom) can be derived as

$$\sigma_R(\omega) = \frac{1}{4} r_e^2 \left[ \frac{\omega^2}{(\omega_0 - \omega)^2 + (\alpha/2)^2} \right] \int_0^\pi \int_0^{2\pi} [\cos^2 \varphi \cos^2 \theta + \sin^2 \varphi] \sin \theta d\theta d\varphi \quad (2.55)$$

It is easy to evaluate the double integral in (2.55) which finally yields

$$\sigma_R(\omega) = \frac{2\pi r_e^2}{3} \left[ \frac{\omega^2}{(\omega_0 - \omega)^2 + (\alpha/2)^2} \right] \quad (2.56)$$

The frequency dependence can be eliminated in terms of the square of the complex refractive index of the medium based on previous research results on Rayleigh scattering [70].

The complex refractive index of the medium is in the form

$$n^2 = 1 + \frac{Ne^2}{\epsilon_0 m_e} \left[ \frac{1}{\omega_0^2 - \omega^2 - j\omega\alpha} \right] \quad (2.57)$$

where  $N$  is the number density of the scatterers, assumed to have an oscillator strength of unity. From (2.57) and (2.53), the Rayleigh differential scattering cross section is given by

$$\frac{d\sigma(\theta, \varphi)}{d\Omega} = \frac{\pi^2 (n^2 - 1)^2}{N^2 \lambda^4} [\cos^2 \varphi \cos^2 \theta + \sin^2 \varphi] \quad (2.58)$$

where  $\lambda = 2\pi c/\omega$  is the wavelength of both the incident and scattered radiation, based on the elastic scattering assumption during which the photons neither gain nor lose energy.

The total Rayleigh scattering cross section per molecule,  $\sigma_R(\lambda)$ , can be obtained from (2.58) by integrating over all angles:

$$\sigma_R(\lambda) = \frac{\pi^2(n^2-1)^2}{N^2\lambda^4} \oint_{\Omega} [\cos^2 \varphi \cos^2 \theta + \sin^2 \varphi] d\Omega \quad (2.59)$$

and this yields

$$\sigma_R(\lambda) = \frac{8\pi}{3} \left[ \frac{\pi^2(n^2-1)^2}{N^2\lambda^4} \right] \quad (2.60)$$

## 2.4 Lidar Technique Implementation

### 2.4.1 LITE Mission

The Lidar In-space Technology Experiment (LITE) was initiated in 1985 by NASA Langley Research Center, which had developed a number of ground-based and airborne lidar systems since the early 1970s. The goals of the LITE mission were to validate key lidar technologies for spaceborne applications, to explore the applications of space lidar, and to gain operational experience which would benefit the development of future systems on free-flying satellite platforms. LITE was flown on the Space Shuttle Discovery as part of the STS-64 mission between September 9 and September 20, 1994. The LITE instrument was designed to measure tropospheric and stratospheric aerosols, clouds, the height of the planetary boundary layer (PBL), stratospheric temperature and density, and, for selected cases, studies of land and ocean reflectance [10]. LITE was a three-wavelength backscatter lidar operating simultaneously at the fundamental wavelength of the Nd: YAG laser, 1064 nm and its second and third harmonics, 532 nm and 355 nm, respectively. The 532 nm and 355 nm channel detectors were photomultiplier tubes (PMT), while the 1064 nm channel detector was a silicon

avalanche photodiode (APD). Because both the backscatter signals and the background radiances collected by a downward-looking lidar receiver in Earth orbit can vary over a wide dynamic range, LITE was designed to handle a variety of uplink commands to configure the optical bandwidths, fields of view, and receiver gains according to particular primary scientific objective at a particular time during the mission. For each of the three channels, there was a programmable electronic attenuator to control the total gain setting of the lidar receiver. When the system operated in the atmospheric mode, the attenuator was set to low attenuation to increase the dynamic range of the signal, while in surface mode the attenuator is set to high attenuation to avoid saturation on the surface returns. The gains of the PMTs for 532 nm and 355 nm channels were also programmable to provide additional gain control for these channels. The LITE system parameters are listed in Tables 2.1 and more details about LITE mission were reported by Winker et al. [10] or on NASA's website (<http://www-lite.larc.nasa.gov>).

LITE was launched into a circular orbit with an initial altitude of 260 km. The altitude was decreased to 240 km for the last few days of the mission to optimize landing opportunities. A 57 degree inclination was chosen to maximize global coverage. With a ground-track orbital velocity of  $\sim 8$  km/s, the 10 Hz laser pulse repetition rate and beam divergence produced a series of laser footprints on the ground of about 280 m diameter spaced by about 740 m, center to center. With regard to the vertical sampling spacing, the bandpass of the receiver electronics has to be taken into consideration. The detected lidar backscattering signal from each channel was first passed through a low pass filter (LPF) before it was sampled and digitized. The 7-pole Bessel low pass filter used in the signal

processing electronics for all three channels had little effect on the atmospheric signal because the vertical change of the distributed scatterers in the air (aerosol and molecules) is slow and continuous. However, the 7-pole Bessel LPF changed the shape of the surface return pulses, which ideally have the same duration and shape as the transmitted pulses.

Table 2.1. LITE system parameters [10]

<b>Laser Transmitter Module</b>			
<i>Output Wavelength (nm)</i>	<b>1064</b>	<b>532</b>	<b>355</b>
<i>Laser A Output Energy (mJ)</i>	470	530	170
<i>Laser A Beam Divergence (mrad)</i>	1.8	1.1	0.9
<i>Laser B Output Energy (mJ)</i>	440	560	160
<i>Laser B Beam Divergence (mrad)</i>	1.8	1.2	1.1
<i>Pulse Repetition Rate (1/s)</i>	10		
<i>Pulse Width (ns)</i>	27		
<b>Aft Optics</b>	<b>1064</b>	<b>532</b>	<b>355</b>
<i>Quantum Efficiency (%)</i>	33	14	21
<i>Color Filter Bandwidth (nm)</i>	675	265	60
<i>Interference Filter Bandwidth (nm)</i>	0.8	0.35	1
<i>Interference Filter Transmission (%)</i>	46	45	33
<i>Optical Throughput (Night) (%)</i>	64	45	42
<i>Optical Throughput (Day) (%)</i>	29	20	14
<i>Field of View (all wavelengths)</i>	<i>Selectable: 1.1 mrad, 3.5 mrad</i>		
<b>Telescope</b>			
<i>Primary Mirror Diameter</i>	37.25 in		
<i>Secondary Mirror Diameter</i>	12.25 in		
<i>Focal Length</i>	189.0 in		
<i>Focal Ratio</i>	f/5.1		
<i>Obscuration Ratio</i>	0.11		
<b>Signal Processing Electronics (all channels)</b>			
<i>Amplifier Bandwidth</i>	2.1 Mhz		
<i>Filter Characteristic</i>	7 pole Bessel Lowpass		
<i>Digitizer Resolution</i>	12bits		
<i>Digitizing Rate</i>	10 Mhz		
<i>Data Sample Period</i>	550 $\mu$ s		
<b>Instrument Data Rate</b>			
<i>high rate channel</i>	2 Mbps		
<i>low rate channel</i>	20.8 Kbps		
<b>Average Power Consumption</b>			
<i>standby</i>	560 W		
<i>lasing(inc. EMP)</i>	3.1 kW		
<b>Mass</b>			
<i>instrument</i>	990 kg		
<i>orthogrid</i>	270 kg		

Typically if we denote the bandwidth of LPF as  $B_f$ , and the pulse rise time as  $t_r$ , then  $t_r$  can be expressed as

$$t_r = \frac{Const}{B_f} \approx \frac{0.35}{B_f} \quad (2.61)$$

The LITE 7-pole Bessel LPF was designed with a bandwidth of  $\sim 2.1$  MHz and with the Const about 0.42. The rise time based on (2.61) can be calculated as

$$t_r = \frac{Const}{B_f} \approx \frac{0.42}{2.1 \times 10^6 \text{ Hz}} = 200 \text{ ns} \quad (2.62)$$

As given in Table 2.1, the LITE laser pulse duration was typically  $\tau_p = 27$  ns, which means that the minimum vertical range resolution,  $\Delta z_{\min}$ , will be determined by  $t_r$  rather than  $\tau_p$ , or,  $\Delta z_{\min} = ct_r/2 = 30\text{m}$ .

Based on Nyquist's sampling theorem, the sampling frequency should be at least twice the highest frequency component in order to reconstruct the original signal without aliasing. For this reason, the vertical sampling range for LITE data was set at

$$\Delta r = \frac{ct_r}{4} \approx 15 \text{ m} \quad (2.63)$$

The LITE mission collected over 40 GBytes of data and presented a detailed global view of the vertical structure of cloud and aerosol from the Earth's surface through the middle stratosphere. Fig. 2.3 is a cartoon overview from the LITE mission, which depicts instrument operation, science targets, and correlative measurement activities (<http://www-lite.larc.nasa.gov>).

The simulation programs in this dissertation used LITE Level 1 data. Comparing with previous versions of LITE data files, e.g. LITE level 0 version 3, the LITE Level 1

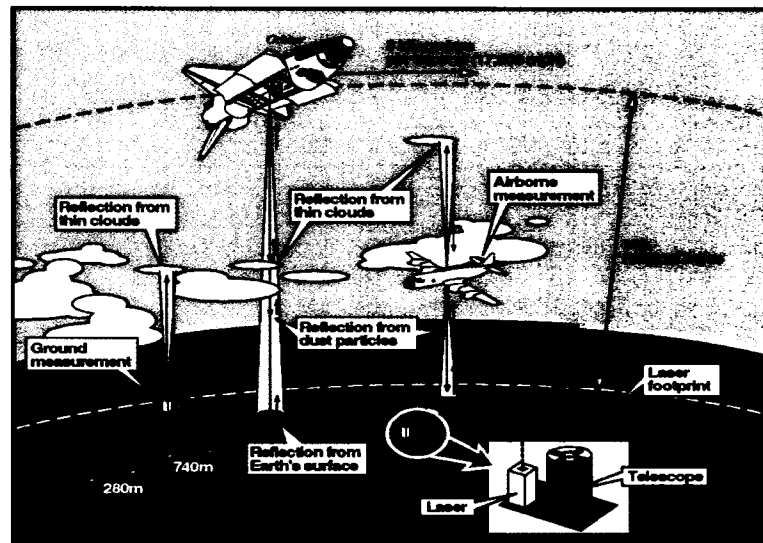


Fig. 2.3 A cartoon overview of the LITE mission (<http://www-lite.larc.nasa.gov>).

data product was formed by processing and reformatting the LITE high-rate telemetry data. The LITE Level 1 processing steps include:

- Correcting the profiles for instrument artifacts.
- Subtracting the DC offset from each lidar profile.
- Interpolating lidar profiles to a geolocated, common altitude grid, which extends from - 4.985 to 40.0 km with a 15 m vertical resolution.
- Determining the LITE system calibration constants for the 355 nm and 532 nm wavelength profiles.

In addition, some other parameters are merged into the LITE Level 1 lidar profiles. These added parameters are listed as below:

- Identification Parameters,
- Time Parameters,
- Location Parameters,

- Operation Mode Parameters,
- Validity Flags,
- Measurement Location Descriptions,
- Temperature and Pressure Profiles Derived from NMC Data,
- Instrument Status Information.

For the LITE Level 0 data format, the data file is composed of a series of blocks containing time synchronized instrument status data blocks (ISDB) and laser shot information. During the operation of LITE, the laser was fired on a 10.0 Hz clock cycle, and an ISDB was generated on a 1.0 Hz clock cycle. Therefore, 10 laser shots coincide with one ISDB. One example of LITE Level 0 data block organization and size is shown in Fig. 2.4

In contrast, the LITE level 1 data file is organized as one data record per lidar pulse. Each data record contains header and lidar profiles for each wavelength. The data format for LITE level 1 data is shown in Table 2.2.

Table 2.2. Level 1 data parameters for each laser shot profile

<b>LITE Level 1 Data Record Organization and Size</b>	
Header	1500 bytes
335 nm lidar profile	12000 bytes
532 nm lidar profile	12000 bytes
1064 nm lidar profile	12000 bytes
<b>Total Size</b>	<b>37500 bytes</b>

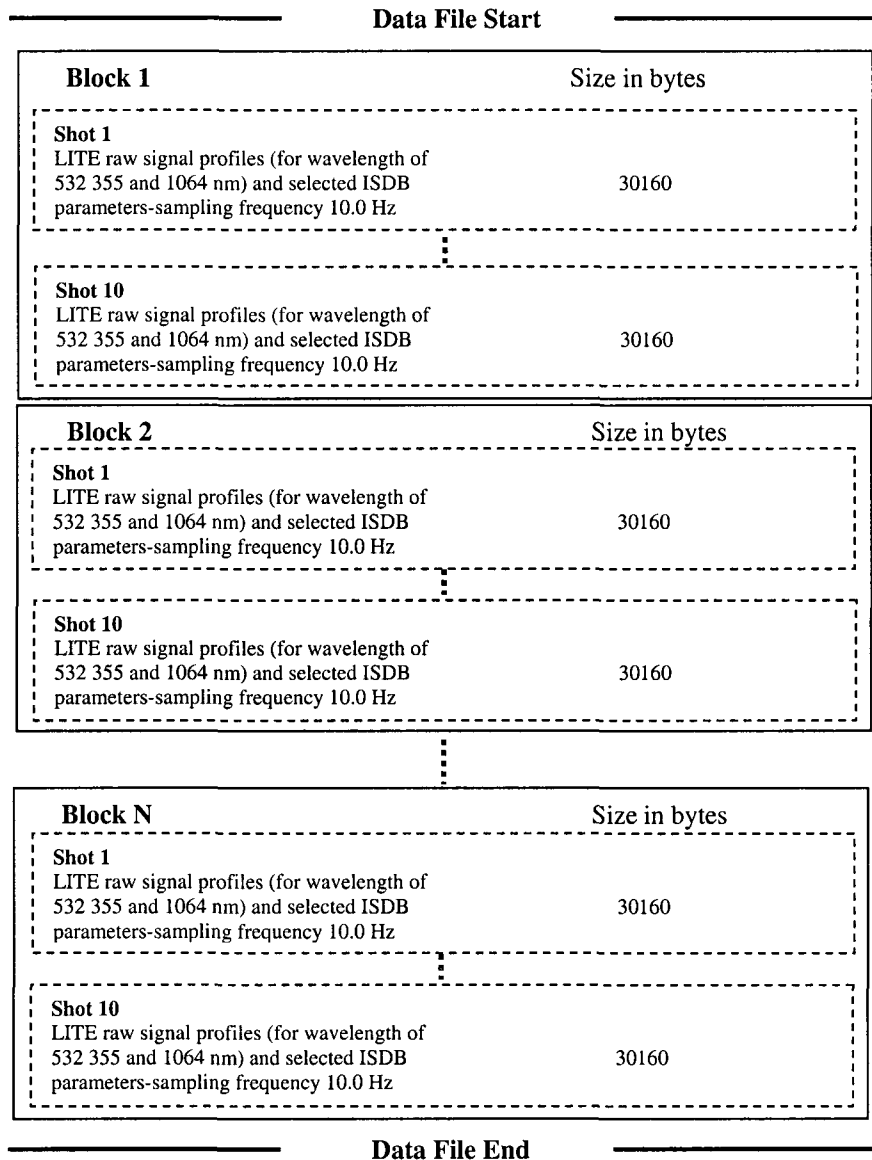


Fig. 2.4.LITE Level 0, version 3 data blocks schematic diagram.

There are a total of 120 parameters for each LITE Level 1 data record. The header information is provided by 117 parameters among which 45 general parameters contain information common for the three wavelength laser profiles, and the remaining 72 parameters contain wavelength specific information (24 for each wavelength). There are three parameters contained in the lidar profiles for the 355 nm, 532 nm and 1064 nm

wavelengths. With the current version of the LITE Level 1 data format, some preprocessing procedures, which were associated with previous versions of LITE data (e.g., LITE Level 0 data), have been removed. The format and the specific content of the LITE Level 1 data record can be found from NASA's official website: <http://www-lite.larc.nasa.gov>. Because the data record is too large to be appropriately included in this dissertation, details about this data record will not be discussed here.

#### 2.4.2 CALIPSO Mission

The Cloud-Aerosol Lidar and Infrared Pathfinder Satellite Observations (CALIPSO) satellite mission is a follow-on to the LITE shuttle mission. It is one of NASA's Earth System Science Pathfinder (ESSP) programs under development by NASA's Langley Research Center with collaboration by the French space agency Centre National d'Etudes Spatiales (CNES), Ball Aerospace and Technologies Corporation, Hampton University and the Institute Pierre Simon Laplace in France. The CALIPSO satellite is scheduled for launch in early 2005 and designed to operate for three years.

Present passive global observations of clouds and aerosols from space mainly monitor how clouds and aerosols vary with latitude and longitude, but provide at best limited information on how they vary with altitude. By using lidar, CALIPSO will provide vertical, curtain-like images of the atmosphere on a global scale (<http://www-calipso.larc.nasa.gov>). With the help of CALIPSO, scientists can determine precisely the altitudes of clouds and aerosol layers and the extent of layer overlap, identify the ice/water composition of some clouds, and estimate the abundance and identify some

types of aerosols. This will assist scientists in better determining how aerosols and clouds affect the Earth's radiation budget.

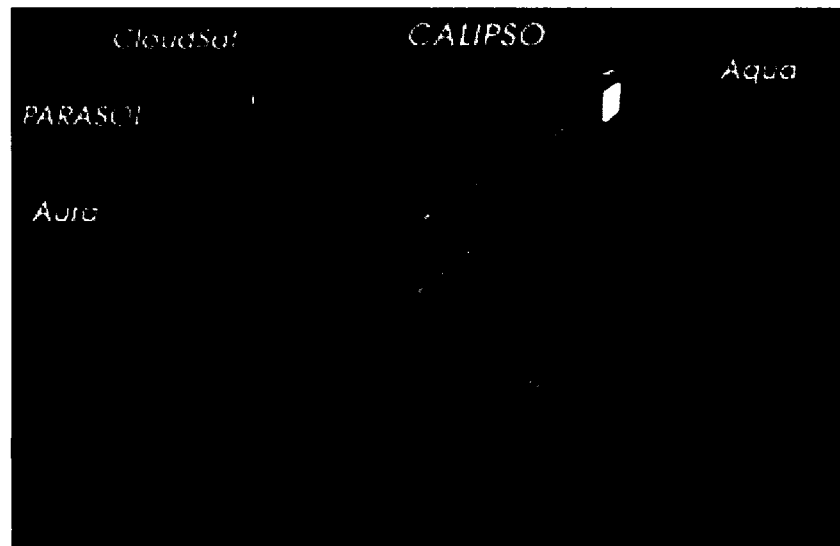


Fig. 2.5. The formation of CALIPSO satellite with Aura, PARASOL, CloudSat, and Aqua satellites (This image courtesy of Jesse Allen, NASA Earth Observatory).

CALIPSO will join the formation of four other satellites that will make a wide variety of nearly coincident measurements (see Fig. 2.5). Each satellite in the formation offers unique information on clouds and aerosols. Combining their data will provide greater insight than could be gained from a single satellite (<http://www-calipso.larc.nasa.gov>). The Earth Observing System (EOS) Aqua satellite, which is focused on understanding the Earth's water or hydrological cycle, will collect data on the geographical distribution of clouds and aerosols, atmospheric temperature, moisture content and the radiation balance at the top of the atmosphere. CloudSat, a sister ESSP satellite experiment, will use a radar to provide vertical profiles of thick clouds that lidar cannot penetrate. The PARASOL (Polarization and Anisotropy of Reflectances for

Atmospheric Science coupled with Observations from a Lidar) satellite, being developed by CNES, will provide unique information on aerosols and clouds using a multi-channel, wide field-of-view, polarization-sensitive camera. Finally, The EOS Aura satellite will monitor atmospheric chemistry and dynamics and will provide information on the geographic distribution of absorbing aerosols. Fig. 2.5 shows the formation of CALIPSO with the other four satellites. A lidar block diagram of CALIPSO is shown in Fig. 2.6 and some instrument specifications of CALIPSO are shown in Table 2.3.

Table 2.3. The instrumentation specifications of CALIPSO (<http://www-calipso.larc.nasa.gov>)

<b>Instrumentation</b>	
<b>CALIOP</b>	<b>Lidar Specifications</b>
<i>Laser</i>	<i>Nd:YAG, diode-pumped, Q-switched, frequency-doubled with ~110 mJ at 532 nm and 1064 nm</i>
<i>Polarization</i>	<i>532 nm has parallel and perpendicular channels</i>
<i>Wavelength</i>	<i>532 nm and 1064 nm</i>
<i>Repetition rate</i>	<i>20 Hz</i>
<i>Telescope aperture</i>	<i>1.0 m</i>
<i>Horizontal resolution</i>	<i>1/3 m~5km</i>
<i>Vertical resolution</i>	<i>30-300m, depending on altitude and wavelength</i>
<i>Field of view (FOV) for all wavelengths</i>	<i>130 <math>\mu</math>rad</i>
<i>Data rate</i>	<i>316 kbps</i>
<b>Imaging Infrared Radiometer (IIR)</b>	<b>IIR Characteristics</b>
<i>Wavelength range</i>	<i>8.7, 10.5, and 12.0 micron</i>
<i>Spectral resolution</i>	<i>0.8 micron</i>
<i>Instrument field of view/Swath</i>	<i>1km/64 km</i>
<i>Data rate</i>	<i>44 kbps</i>
<b>Wide Field Camera (WFC)</b>	<b>WFC Characteristics</b>
<i>Wavelength range</i>	<i>620 to 670 nm</i>
<i>Instrument field of view/Swath</i>	<i>125 m/60 km</i>
<i>Data rate</i>	<i>26 kbps</i>

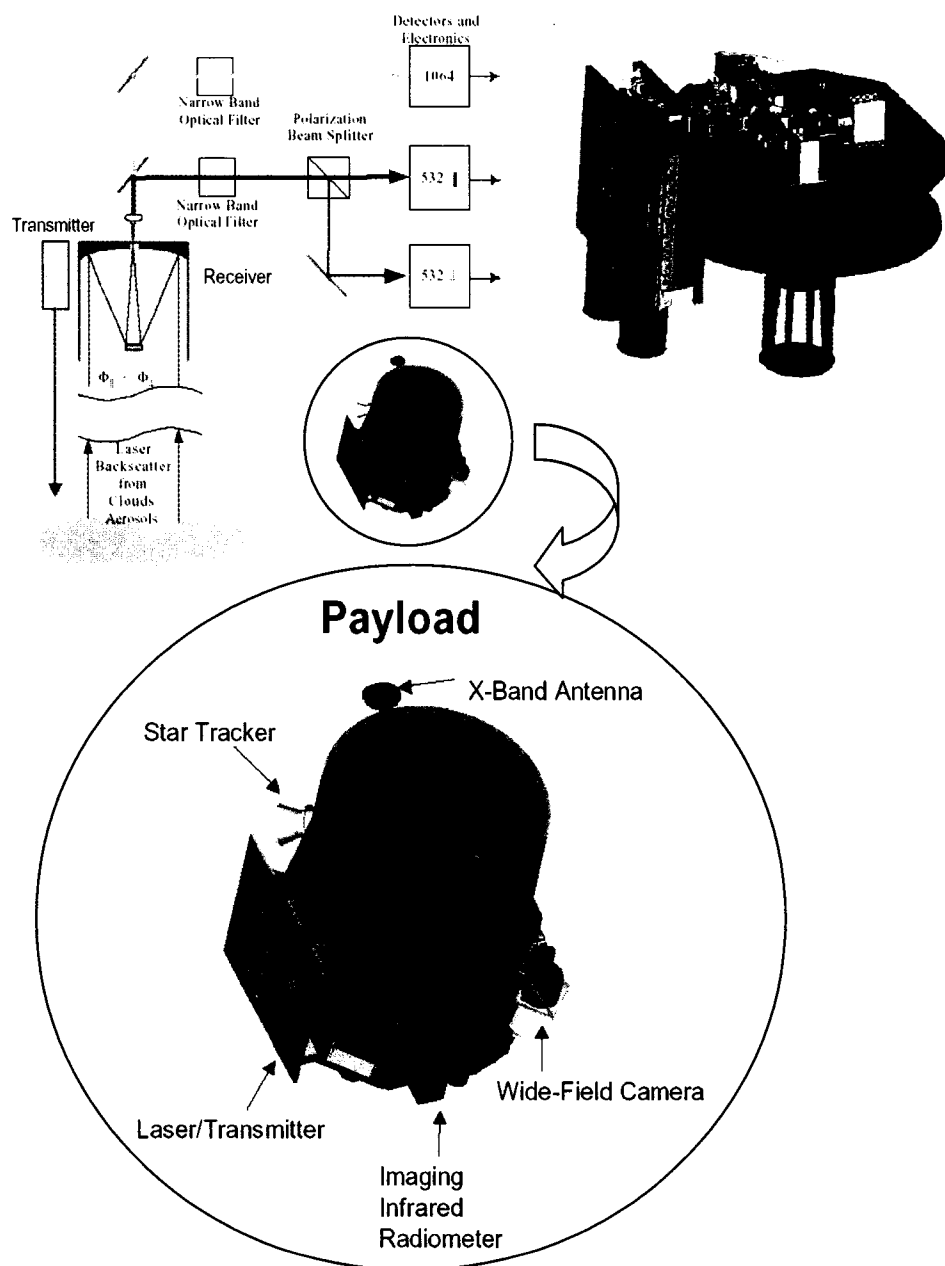


Fig. 2.6. Lidar block diagram of CALIPSO [71].

### 3. SPACEBORNE LIDAR CALIBRATION FROM CIRRUS AND MOLECULAR BACKSCATTER RETURNS

The calibration factor of a lidar system (e.g., LITE) includes effective receiver aperture, detector quantum efficiency, and the losses in the transmitting and receiving optics. The lidar system must be well calibrated in order to achieve quantitative retrievals of aerosol and cloud properties. Following the procedures employed for LITE, in situ calibration of the 532 nm lidar channel can be accomplished via normalization to a high altitude, nearly molecular scattering region. However, the molecular backscatter is too weak to permit such calibration for the longer 1064 nm channel. An alternative approach investigated by Reagan et al. [19] during the LITE shuttle mission employed surface backscatter returns from selected land surfaces as standard targets to calibrate the LITE 1064 nm channel. This approach yielded calibration uncertainties in the 10% range, but only for limited, well characterized surfaces. With the objective of finding a more feasible calibration method, which can be implemented on-orbit, preferably repeatable at least a few times per orbit during CALIPSO satellite mission, a new 1064 nm calibration method was developed. Specifically, that the calibration of the 1064 nm channel relative to the 532 nm channel calibration be accomplished via comparisons of the 532 nm and 1064 nm backscatter signals from cirrus clouds. Due to the low signal for noncloud returns, it is difficult to remove the noncloud signal from the total signal. For the approach presented here, only strong cloud signal returns are selected. Consequently, the

contamination by noncloud returns is minimized. This avoids uncertainty in subtracting a variable background level that must be done for weak cloud returns.

Examples demonstrating the 532 nm molecular normalization calibration approach are presented based on representative LITE data from orbits 24 and 34. Error assessments are included which support achievable calibration uncertainties within 5% by this approach. Cirrus cloud returns from LITE orbits 23, 24 and 27 have been analyzed to assess the feasibility of the cirrus cloud calibration approach [51]. Results are given which indicate that calibration of the CALIPSO 1064 nm channel in terms of, or as a ratio to, the 532 nm calibration factor by using cirrus cloud returns appears quite feasible.

### 3.1 532 nm Calibration

#### 3.1.1 Physical Model and Mathematical Description

Calibration of a nadir/near-nadir viewing spaceborne lidar via normalization to high altitude, nearly molecular scattering regions is, in principle, very straightforward. From the normalized lidar equation (2.7), the lidar calibration factor or constant at 532 nm,  $C_{532}$ , may be extracted from the lidar signal obtained at a reference calibration range,  $r_c$ , by

$$C_{532} = \frac{X(r_c)}{R(r_c)\beta_R(r_c)T^2(r_c)} \quad (3.1)$$

where

$\beta_R(r_c)$  = Rayleigh backscatter (for the lidar wavelength) at range  $r_c$  for 532 nm

$R(r_c) = \beta(r_c) / \beta_R(r_c)$ ; total to Rayleigh backscattering mixing ratio at range  $r_c$

In many papers (e.g., [9, 16]), altitude,  $z$ , is used in the lidar equations. For a downward-looking lidar, the range,  $r$ , which is the distance between the lidar and the target, is more frequently used. The relationship between  $r$  and  $z$  has been described in section 2.2.1, and Fig. 3.1 is given to help clarify this confusion.

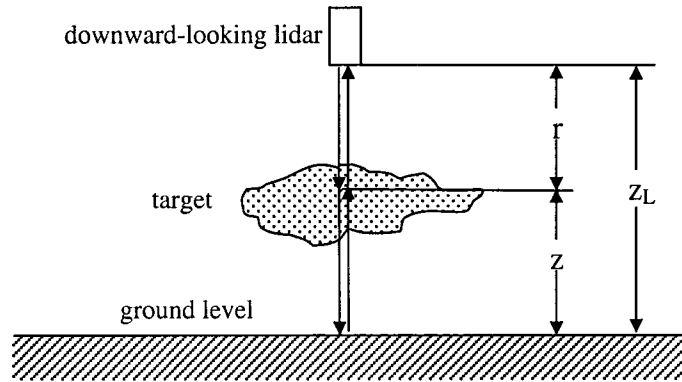


Fig. 3.1. A schematic diagram for the relationship between range  $r$  and altitude  $z$ .

For  $r_c$  selected to be around 30 km above ground where the ozone optical depth,  $\tau_{O_3}(r_c)$ , is very small,  $R(r_c) \approx 1$  and  $T^2(r_c) \approx 0.99$  are very good approximations for 532 nm, enabling accurate retrievals of  $C_{532}$  providing the signal uncertainty is sufficiently small and  $\beta_R(r_c)$  can be accurately computed (driven by how accurately the air density can be determined).

The total Rayleigh-scattering cross section per molecule,  $\sigma_R(\lambda)$ , was given by (2.59). Considering the anisotropic properties of some scattering molecules, the Rayleigh scattering cross section per molecule is modified to take the more general form [22]

$$\sigma_R(\lambda) = \frac{8\pi}{3} \left[ \frac{\pi^2 (n^2 - 1)^2}{N^2 \lambda^4} \right] \left( \frac{6 + 3\delta}{6 - 7\delta} \right) \quad (3.2)$$

where  $\delta$  is the depolarization factor, which will be discussed in more detail in Chapter 4.

The total Rayleigh volume backscattering coefficient  $\beta_{R,\lambda}(z)$  is given by the product of the total Rayleigh cross section per molecule,  $\sigma_R(\lambda)$ , as defined in Eq. (3.2), the molecular number density  $N(z)$ , for a given pressure and temperature at altitude  $z$ , and the Rayleigh extinction-to-backscatter ratio,  $S_R$  (e.g., [9, 67]):

$$\beta_{R,\lambda}(z) = S_R^{-1} N(z) \sigma_R(\lambda) \quad (3.3)$$

where  $S_R = 8\pi/3$ .

In terms of pressure,  $p(z)$ , and the absolute temperature,  $t(z)$  at height  $z$ , the number density of molecules,  $N(z)$ , is given by

$$N(z) = \frac{N_A p(z)}{R^* t(z)} \quad (3.4)$$

where  $N_A$  is Advogadro's number, which is  $6.02486 \times 10^{23} \text{ mole}^{-1}$ , and  $R^*$  is the universal gas constant, which is  $8.3144 \times 10^7 \text{ erg mole}^{-1} \text{ k}^{-1}$ . If  $p(z)$  is expressed in mb,  $t(z)$  in k,  $N(z)$  in  $\text{cm}^{-3}$ , then

$$N(z) = 0.72463 \times 10^{19} \frac{p(z)}{t(z)} \quad (3.5)$$

The pressure and temperature of the atmosphere from the LITE database are given over a much coarser vertical spacing than that of the LITE data; values of  $p(z)$  and  $t(z)$  at intermediate levels are determined by extrapolating and interpolating to the LITE locations.

The Rayleigh per molecule cross section can be accurately determined within a few tenths of a percent [25], leaving  $N(z)$  as the primary source of uncertainty in

determining  $\beta_{R,\lambda}(z)$ . Using ancillary meteorological data along the satellite track, it is estimated that  $\beta_R(r_c)$  can be determined within about  $\pm 3\%$  uncertainty. For  $z$  near 30 km, this corresponds to knowing temperature within  $\sim \pm 5\text{K}$  and pressure within  $\sim \pm 2.5\text{mb}$ , which is about the level of uncertainty associated with just assuming a latitudinal, seasonal standard atmospheric model [16, 26]. Using pressure and temperature fields derived from weather network measurements and assimilation models, coupled with averaging the  $C_{532}$  retrievals over significant horizontal extents ( $\sim$ several hundred kilometers), it is anticipated that the  $N(z)$  uncertainty can be further reduced. However, for the estimates presented here, it is assumed that  $\beta_R(r_c)$  is not known better than  $\pm 3\%$ .

In the 532 nm calibration algorithm, LITE data is processed with a 4 km vertical averaging window over the range from  $z = 30$  to 34 km and 200 shot ( $\sim 150$  km) horizontal block averaging. In order to increase the SNR, various total horizontal extents of  $\sim 1000$  km up to half an orbit can be employed. The detailed expressions for calculating  $C$  for varying horizontal segments are given by the following equations:

$$C_{532}(y_k) = \frac{1}{j_{34} - j_{30} + 1} \sum_{j=j_{30}}^{j_{34}} \frac{\frac{1}{200} \sum_{i=200k}^{200(k+1)-1} X_{532}(y_i, z_j)}{\beta_{m,532}(y_k, z_j) R(y_k, z_j) T^2(y_k, z_j)} \quad (3.6)$$

$$\bar{C}_{532}(y_k) = \frac{1}{M} \sum_{k=0}^{M-1} C_{532}(y_k) \quad (3.7)$$

where

$i$  = index for the  $i^{\text{th}}$  full-resolution profile (horizontal resolution =  $\sim 0.74\text{km}$ )

$j$  = index for the  $j^{\text{th}}$  vertical sample in a high resolution profile (vertical resolution = 300 m)

$j_{30}$  = vertical index corresponding to 30 km

$j_{34}$  = vertical index corresponding to 34 km

$k$  = index for the  $k^{\text{th}}$  calibration factor (computed horizontally every ~150 km)

$y$  = horizontal distance along the ground track

$z$  = vertical distance

$M$  = the number of unsmoothed calibration factors corresponding to a range of ~1000 km up to half an orbit ( $M \geq 7$ )

$C_{532}$  = unsmoothed calibration factor computed approximately every 150 km along track

$\bar{C}_{532}$  = smoothed calibration factor computed every ~1000 km along track

### 3.1.2 LITE Retrieval Results for the 532 nm Calibration Factor

Extracting absolute estimates of  $C_{532}$ , as can be seen from (3.1), requires that  $r_c$ ,  $E_0$ ,  $R_{532}(r_c)$ ,  $\beta_{R,532}(r_c)$  and  $T_{532}^2(r_c)$  all be known/specified. It is assumed that this can be done with essentially no significant error (i.e., less than ~0.5% error) for  $r_c$  and  $E_0$  (a relative energy normalization is all that is actually required), and with manageably small error for  $\beta_{R,532}(r_c)$ , using temperature and pressure meteorological data incorporated in the LITE or CALIPSO databases. As discussed earlier, using molecular number densities calculated from pressure and temperature fields derived from assimilated network measurements should yield estimates of  $\beta_{R,532}(r_c)$  easily within  $\pm 3\%$ . Also, for  $r_c$  selected in the mid to upper stratosphere,  $T_{532}^2(r_c)$  will generally be within about one percent of unity, but must still be specified to extract  $C_{532}$ . Applying standard error propagation analysis to the  $C_{532}$  retrieval equation, (3.1), yields

$$\left[ \frac{\delta C_{532}}{C_{532}} \right]^2 = \left[ \frac{\delta X_{532}(r_c)}{X_{532}(r_c)} \right]^2 + \left[ \frac{\delta R_{532}(r_c)}{R_{532}(r_c)} \right]^2 + \left[ \frac{\delta \beta_{R,532}(r_c)}{\beta_{R,532}(r_c)} \right]^2 + \left[ \frac{\delta T_{532}^2(r_c)}{T_{532}^2(r_c)} \right]^2 \quad (3.8)$$

The details of the error analysis that are related to the error propagation will be discussed more in Chapter 4. Assuming uncertainties that should reasonably apply in the stratosphere for  $r_c$  in the range of 30 to 34 km above ground, as listed in Table 3.1, yields an uncertainty in  $C_{532}$  of about 4.4%, as also given in the table.

Table 3.1 Uncertainty estimates of the 532 nm calibration constant and related parameters.

$\frac{\delta C_{532}}{C_{532}}$	$\frac{\delta X_{532}}{X_{532}}$	$\frac{\delta R_{532}(r_c)}{R_{532}(r_c)}$	$\frac{\delta \beta_{m,532}(r_c)}{\beta_{m,532}(r_c)}$	$\frac{\delta T_{532}^2(r_c)}{T_{532}^2(r_c)}$
0.044	0.03	0.01	0.03	0.005

A retrieval of  $C_{532}$  for a segment of orbit 24, which is shown in Fig. 3.2, yields a ~2% relative uncertainty of  $C_{532}$ . In Fig. 3.3, retrievals of  $C_{532}$  from orbit 34 LITE data are presented for 4km vertical averaging over the altitude range  $z = 30$  to 34 km and 200 shot (~150 km) minimum horizontal block averaging, for various total horizontal extents of ~1000 km up to half an orbit. In Fig. 3.3(a),  $C_{532}$  is calculated based on a 200 shot average spanning about a 1000 km total horizontal extent (during the nighttime portion), Fig.3.3 (b) is based on a 1000 shot average, spanning about half the nighttime portion of the orbit, and in Fig. 3.3 (c) the 1000 shot average extends over entire nighttime portion of the orbit. Each data point in the figures includes  $\pm$ one standard deviation error bars for the number of shots averaged for the point (either 200 or 1000 shots). These values are averaged for the number of points in each figure, yielding the average and standard derivation values cited in the figures. The standard deviation of the 200 shot average

points is mainly determined by the uncertainty in the normalized signal  $X$  and is in the range of 3%.

From Fig. 3.3 it can be seen that  $C_{532}$  for orbit 34 is around  $2.41 \times 10^{15}$  and the relative uncertainty of  $C_{532}$  is less than 2%. Here it is important to note that these figures depict the effects of signal uncertainty and relative spatial variability in  $\beta_{R,532}(r_c)$ ,  $R_{532}(r_c)$  and  $T_{532}^2(r_c)$ , but not the absolute errors in these latter three factors. What the figures demonstrate is that averaging over horizontal extents of  $\sim 1000$  to  $10,000$  km should still yield averages with uncertainties within about 2% insofar as these horizontal inhomogeneity effects are concerned. The results shown for orbit 34 are typical of other orbits [72] and the results shown in Fig. 3.2 yield a  $C_{532}$  within about 2% of the orbit 34 results. Some change in  $C_{532}$  between several orbits was observed during the LITE mission [72], presumably reflecting instrument changes and drift. Hence, a repeatable, on-orbit calibration approach is needed to overcome these effects.

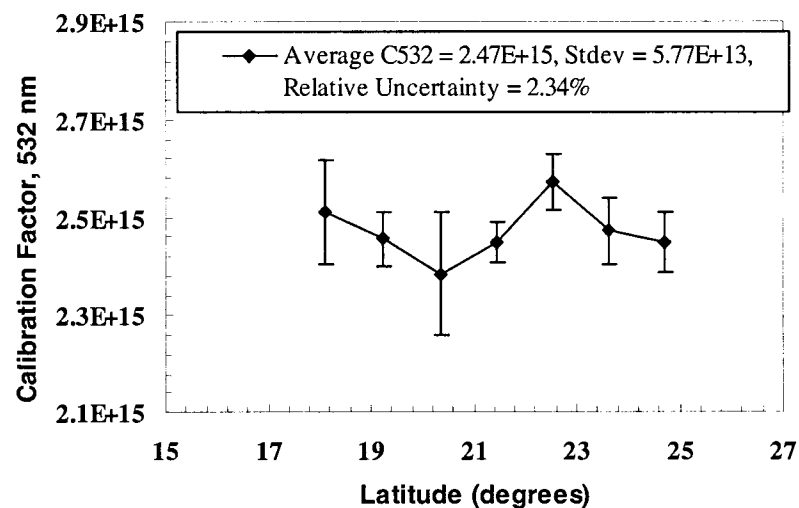


Fig. 3.2 Retrieved 532 nm calibration constant for a portion of LITE orbit 24 based on a 200 shot average spanning about a 1000 km horizontal extent [51].

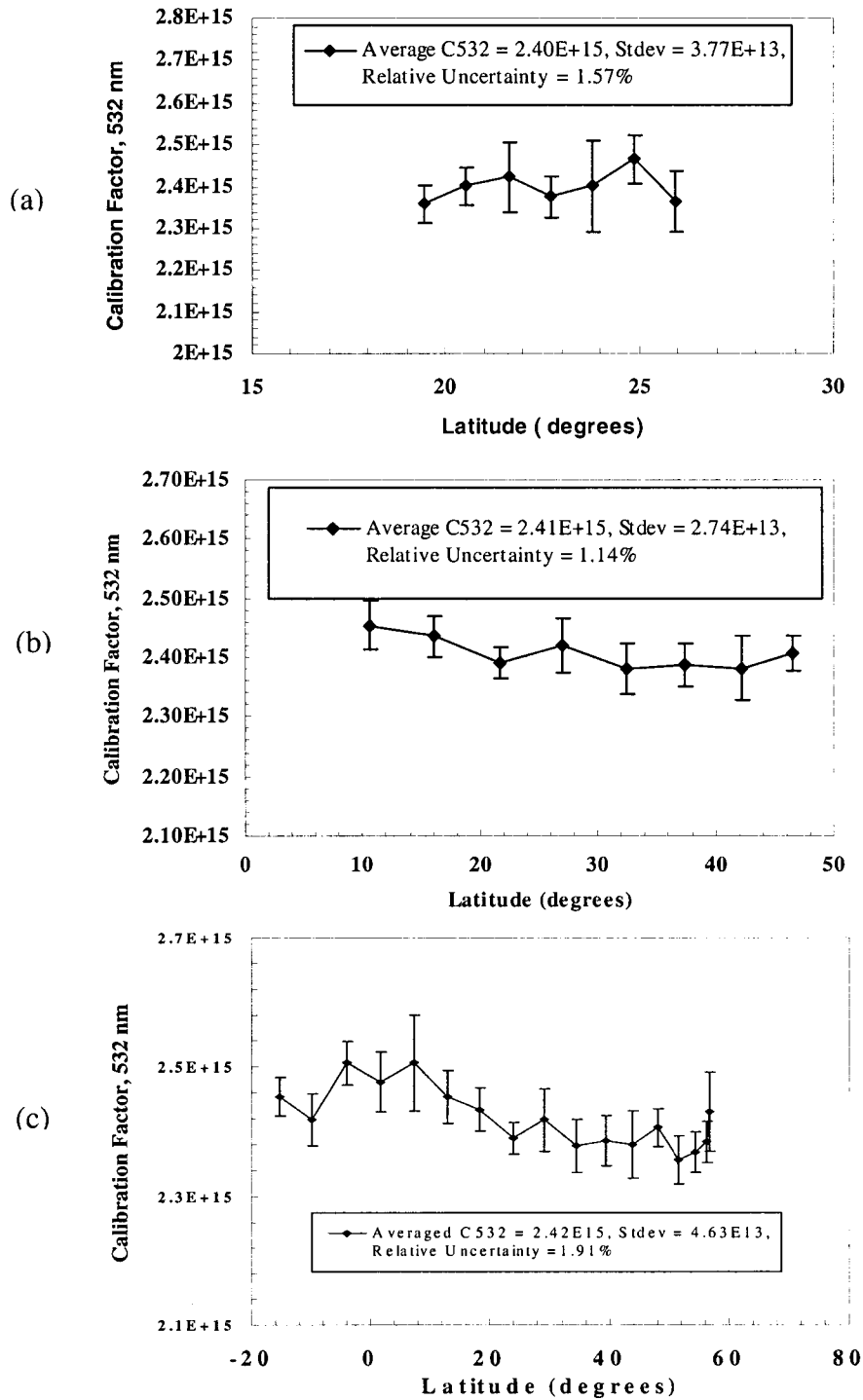


Fig. 3.3 Retrieved 532 nm calibration constant for portions of LITE orbit 34: (a) based on a 200 shot average spanning about a 1000 km horizontal extent, (b) based on a 1000 shot horizontal average over about half the nighttime portion of orbit 34 and (c) based on a 1000 shot horizontal average for the entire nighttime portion of orbit 34 [51].

### 3.1.3 CALIPSO Simulation Results for the 532 nm Calibration

The schematic diagram of the CALIPSO lidar system in Fig. 2.6 has shown that the CALIPSO 532 nm channel includes both parallel and perpendicular polarized components. A block diagram representing the basic flow of the calibration process is shown in Fig. 3.4. For CALIPSO, the polarization (532 nm) of backscatter from the molecular atmosphere is almost completely parallel to the transmitted laser in the mid-stratosphere. The simulated CALIPSO calibration results presented in this chapter are only for 532 nm parallel channel.

The 532 nm calibration algorithm used for CALIPSO is the same as what was described for LITE in previous sections. But due to the changes in horizontal and vertical resolutions, the horizontal and vertical averaging range will be different. Table 3.2 lists the spatial resolutions of CALIPSO simulated data. In addition, when calculating the total Rayleigh-scattering cross section per molecule,  $\sigma_R(\lambda)$ , the depolarization factor used was 0.0036 [73], which is for Cabannes scattering and will be discussed further in Chapter 4. The depolarization factor used for LITE calibration is 0.0279 [22].

Basically, there are three main steps in the 532 nm CALIPSO calibration:

*Step 1:* The normalized parallel channel profile data,  $X_{//,532}$ , are averaged horizontally over 11 full-resolution profiles. At the calibration altitude, a full-resolution profile corresponds to a 5-km along track resolution (due to averaging done on board the satellite for data compression purposes); thus, the 11-profile average corresponds to a 55-km

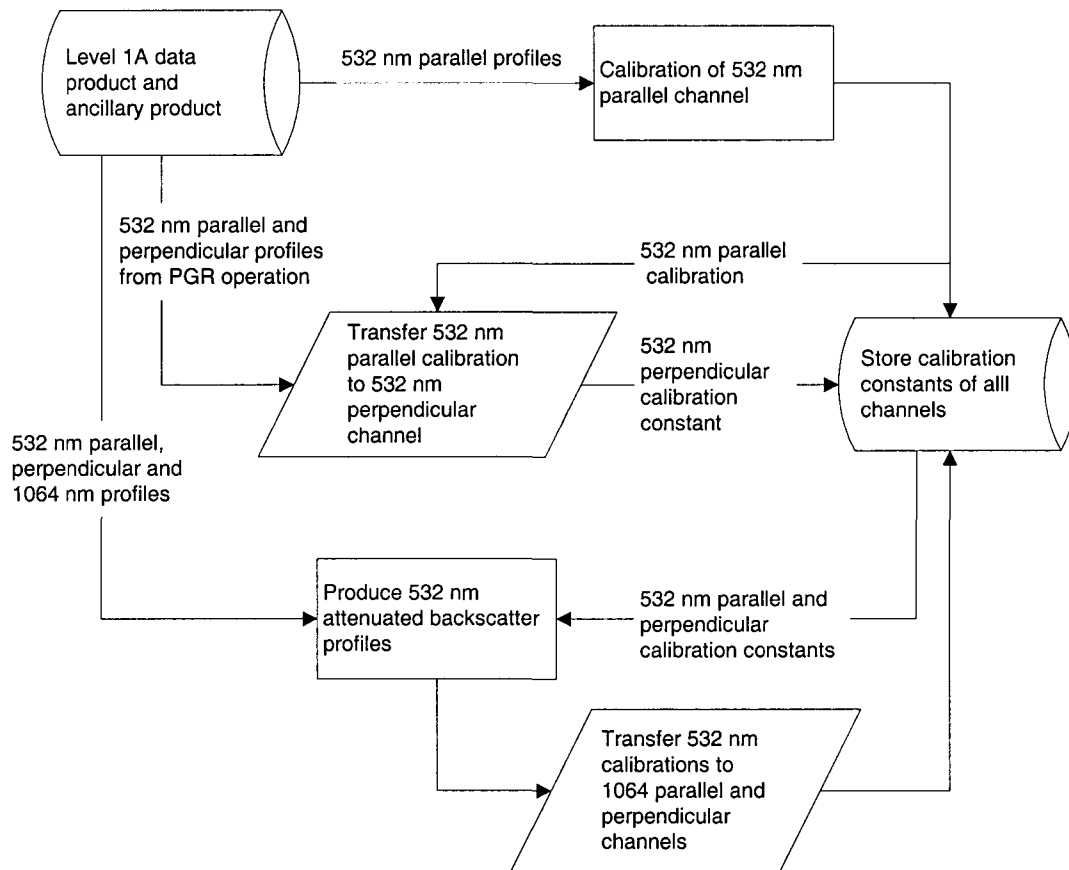


Fig. 3.4 Block diagram representing the basic flow of the calibration processes for CALIPSO.

Table 3.2. The spatial resolution of CALIPSO simulated data

Altitude Region	Resolution	
	Horizontal	Vertical
30.1 to 40.0 km (532 nm only)	5km @ 532 nm (15 laser shots)	0.30 km @ 532 nm
20.2 to 30.1 km	1.667 km (5 laser shots)	0.18 km
8.2 to 20.2 km	1 km (3 laser shots)	0.06 km
-0.5 to 8.2 km	0.333 km (1 laser shot)	0.03 km @ 532 nm 0.06 km @ 1064 nm
-2.0 to -0.5 km	0.333 km (1 laser shot)	0.30 km

along track average (see Fig. 3.5). Intermediate values of the calibration factor are then computed for each vertical sample in this horizontally averaged composite profile.

*Step 2:* The computed calibration factors at each altitude are averaged vertically over the entire calibration range (4km or whatever is selected), which results in a single estimate of the calibration factor for each 55 km orbit segment along the night side of the orbit.

*Step 3:* In order to further smooth the sequence of values, these calibration factors are further averaged via a 13-point running average filter, resulting in an effective 715 km average between two adjacent independent samples.

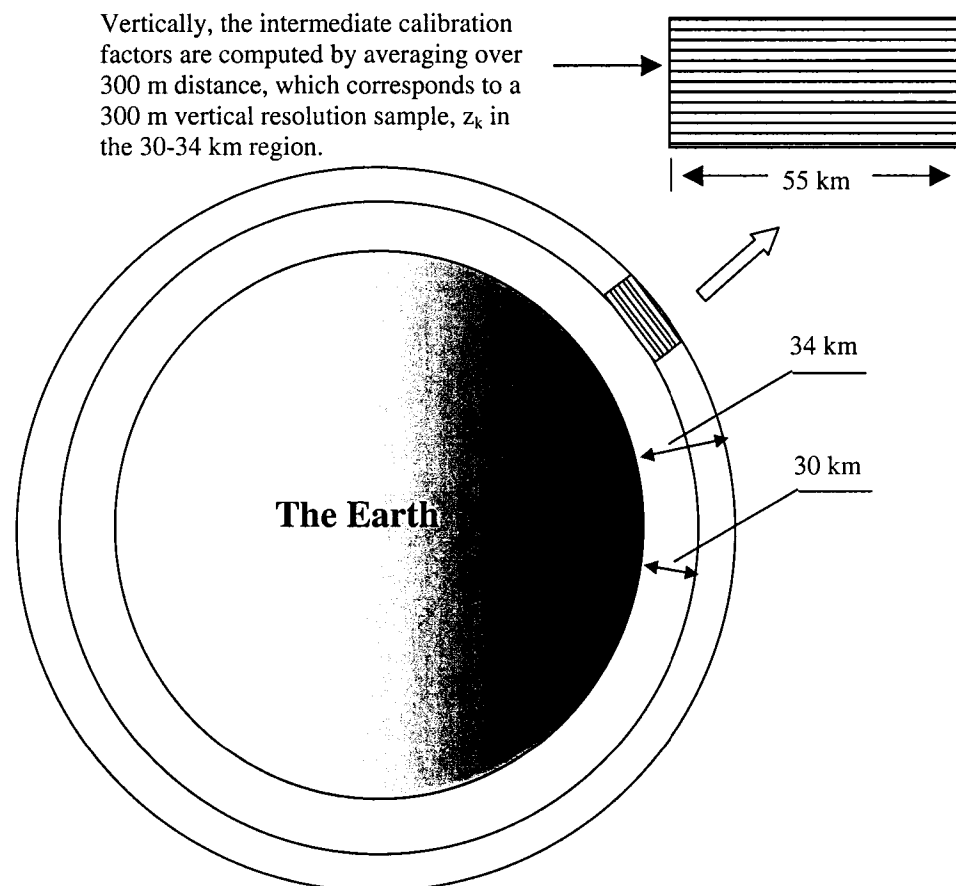


Fig. 3.5. A schematic diagram for demonstrating the implementation of the 532 nm CALIPSO calibration for every 55 km along the night side of the orbit in the 30-34 km region.

The final Calibration Data Product (CDP) will include both the smoothed and unsmoothed calibration factors, which will be used to interpolate/extrapolate calibration factors throughout the orbit. The calibration algorithms for the 532 nm parallel channel can be expressed by

$$C_{//,532}(y_k) = \frac{1}{j_{34} - j_{30} + 1} \sum_{j=j_{30}}^{j_{34}} \frac{\frac{1}{11} \sum_{i=11k-5}^{11k+5} X_{//,532}(y_i, z_j)}{\hat{\beta}_{m, //, 532}(y_k, z_j) \hat{R}_{//}(y_k, z_j) \hat{T}^2(y_k, z_j)} \quad (3.9)$$

$$\bar{C}_{//,532}(y_k) = \frac{1}{13} \sum_{k=6}^{k+6} C_{//,532}(y_k) \quad (3.10)$$

where

i = index for the i<sup>th</sup> full-resolution profile (horizontal resolution = 5km)

j = index for the j<sup>th</sup> vertical sample in a high resolution profile (vertical resolution = 300 m)

j<sub>30</sub> = vertical index corresponding to 30 km

j<sub>34</sub> = vertical index corresponding to 34 km

k = index for the k<sup>th</sup> calibration factor (computed every 55 km)

y = horizontal distance along the ground track

z = vertical distance

$C_{//,532}$  = unsmoothed calibration factor computed every 55 km along track

$\bar{C}_{//,532}$  = smoothed calibration factor computed every 715 km along track

The term,  $\frac{1}{11} \sum_{i=11k-5}^{11k+5} X_{//,532}(y_i, z_j)$ , in equation (3.9), is the horizontal average over

11 5-km profiles, for Step 1, which gives the k<sup>th</sup> average calibration factor corresponding

to a 55-km cell and altitude  $z_j$ . Equation (3.9) gives the average intermediate calibration constants averaged vertically from 30 to 34 km. In equation (3.10), a running average filter is used to compute the running average over the 13 55-km cells, each of which spans over 715 km. Fig. 3.5 pictorially displays the averaging process.

It should also be noted that  $\hat{\beta}_{m, //, 532}(y_k, z_j)$ ,  $\hat{R}_{//}(y_k, z_j)$  and  $\hat{T}^2(y_k, z_j)$  are estimates of the corresponding parameters computed for the  $k^{\text{th}}$  55-km along-track cell and  $j^{\text{th}}$  altitude bin. As described in earlier sections, these parameters are obtained from external data sources, which include the output from global meteorological analyses and measurements from other instruments. The external data include profiles of pressure, temperature, aerosol extinction and/or backscatter, and ozone concentration. The external data are interpolated along the ground track such that the sampling is identical in space and time to the CALIPSO full resolution profiles. Horizontal averages of the estimated quantities are produced on the 55-km grid established for the CALIPSO calibration data product.

CALIPSO simulations based on specified lidar system parameters (Table 2.3) predict that the shot-noise limited uncertainty in  $X(r)$  for a height of 30 km above ground and 4 km vertical averaging should be within about  $\pm 3\%$  for horizontal averaging of not more than  $\sim 1000$  km. As shown in Fig. 3.2 and Fig. 3.3, results from LITE demonstrate that horizontal averaging over 1000 km and more without significant horizontal inhomogeneity biases, should be quite feasible. Hence, the molecular normalization approach should enable on-orbit calibrations of  $C_{532}$  for CALIPSO with uncertainties within  $\pm 5\%$ . The calibration constant,  $C_{//, 532}$  for CALIPSO, was calculated with the

simulated CALIPSO data, which was obtained by running the LITE data (orbits 34 and 103) through the CALIPSO simulator [74]. The calculated  $C_{//,532}$  for simulated CALIPSO orbits 34 and 103 are shown in Figs 3.6 and 3.7; the relative uncertainties of  $C_{//,532}$  are 2% (orbit 34) and 1.24% (orbit 103) with a horizontal average of  $\sim 1000\text{km}$ .

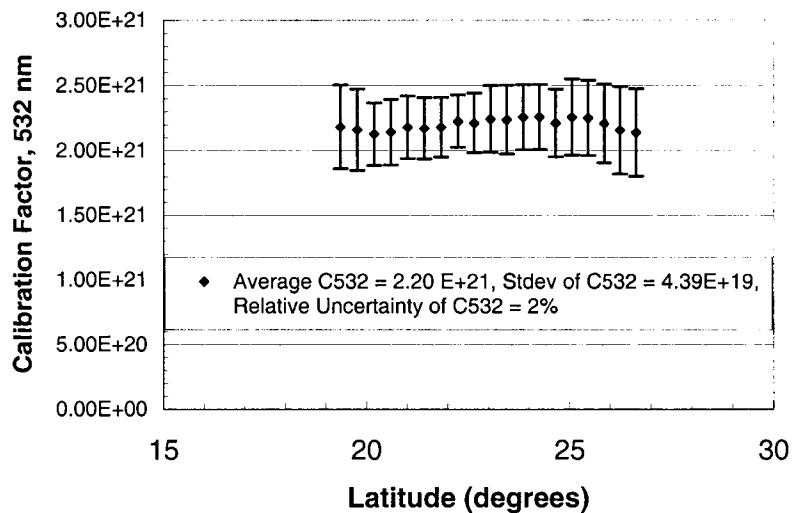


Fig. 3.6. The calculated calibration constant,  $C_{532}$ , for CALIPSO with the simulated CALIPSO data (from LITE orbit 34).

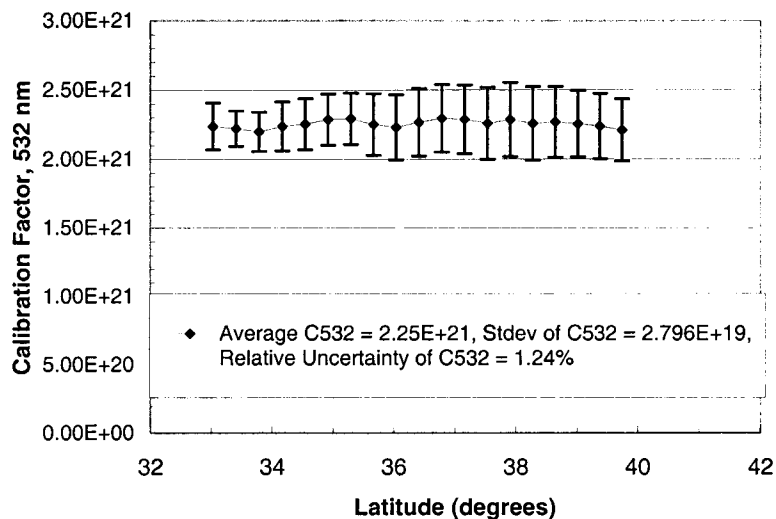


Fig. 3.7. The calculated calibration constant,  $C_{532}$ , for CALIPSO with the simulated CALIPSO data (from LITE orbit 103).

## 3.2 1064 nm Calibration

### 3.2.1 Operational 1064 nm Calibration Algorithms

Given  $C_{532}$  determined by the molecular calibration approach, cirrus clouds offer good candidate targets by which the calibration ratio  $C_{1064}/C_{532}$  can be estimated from the ratio of the normalized returns for the two wavelengths. This is feasible because, to first order, the backscatter and extinction from cirrus should be nearly the same for both wavelengths. Also, as cirrus cloud occurs at high altitudes, corrections for 1064/532 spectral transmittance differences between the satellite and the cloud top are relatively small and predictable.

The normalized cloud return,  $X_c(r)$ , defined as the total normalized return minus the non-cloud background normalized return, is given approximately by

$$X_c(r) = C_{1064} T_{ct}^2 \beta_c(r) T_c^2(r) \quad (3.11)$$

where

$C_{1064}$  = lidar calibration factor

$T_{ct}^2$  = round-trip transmittance to cloud top at range  $r_{ct}$ .

$\beta_c(r)$  = cloud backscatter for  $r > r_{ct}$

$T_c^2(r)$  = cloud round-trip transmittance from  $r_{ct}$  to  $r > r_{ct}$

As cirrus particles are typically sufficiently large relative to the 532 and 1064 nm wavelengths for the geometrical optics limit to reasonably apply, there should be no wavelength dependence in the extinction and backscatter for these two wavelengths [75],

[76], save any small refractive index difference effects. In addition, cirrus spectral optical depths measured by sunphotometers are observed to be quite spectrally flat over ~500 to ~1000 nm range [77]. In fact, screening for spectral flatness in optical depth is a technique often employed to detect the presence of very thin cirrus contamination in derived aerosol optical depths. Lidar data, though sparse, supports  $\beta_{c,532} = \beta_{c,1064}$  within measurement/calibration uncertainties (albeit these uncertainties are typically somewhat large, ~10 to 20%). Preliminary analysis of lidar observations made during the SAFARI-2000 campaign with the NASA/GSFC Cloud Physics Lidar, deployed on a NASA ER-2, reveals that  $\beta_{c,1064}/\beta_{c,532}$  is quite constant, not highly variable, and close to unity [78]. Finally, for spaceborne lidar to cloud geometry and even a very small receiver FOV (~100 microradians), multiple scattering effects should be effectively the same for both wavelengths (assuming beam divergences and receiver FOV's are similar for both wavelengths). All of this supports assuming  $\beta_c T_c^2$  to be spectrally flat.

Assuming  $\beta_c T_c^2$  is the same for 532 nm and 1064 nm, the ratio of  $X_c$  for the two wavelengths at any  $r$  within the cloud will be

$$\frac{X_{c1064}}{X_{c532}} = \frac{C_{1064}}{C_{532}} \times \frac{T_{cr1064}^2}{T_{cr532}^2} \quad (3.12)$$

yielding

$$\frac{C_{1064}}{C_{532}} = \frac{X_{c1064}}{X_{c532}} \times \frac{T_{cr532}^2}{T_{cr1064}^2} \quad (3.13)$$

In order to minimize the noncloud return, a threshold is selected to screen out the weak backscatter signals. By setting a high threshold, the non-cloud background can be

ignored, allowing  $X_c$  be approximated by  $X$ , the total signal including the non-cloud background. Then the calibration ratio may be approximated by

$$\frac{C_{1064}}{C_{532}} \approx \frac{X_{1064}}{X_{532}} \times \frac{T_{cr,532}^2}{T_{cr,1064}^2} \quad (3.14)$$

The last term is approximately 0.9 at about 12 km above ground and can be estimated more accurately from profile models of aerosol extinction and ozone concentration and an atmospheric density profile [26].

A threshold signal,  $X_t$ , for determining strong cloud returns may be determined by computing the 532 nm normalized signal that is equivalent to a scattering ratio of  $R_t$ . Expressing  $X_t(r)$  in terms of altitude above ground,  $z$ , which is normally how molecular and aerosol scattering coefficients and cloud positions are height referenced,  $X_t(z)$  may be expressed by

$$X_t(z) = C_{532} \times R_t \times \beta_{m,532}(z) \times T_{532}^2(z_L - z) \quad (3.15)$$

where  $R_t = \frac{\beta_a(z) + \beta_m(z)}{\beta_m(z)}$ , and  $z_L$  is the lidar height above ground (see Fig. 3.1)

Setting  $R_t$  to a large value, on the order of 50, insures  $X_c \approx X$ . Once again, for the heights of cirrus clouds, the transmission term can be modeled fairly accurately and is close to unity. This threshold is applied only to the 532 nm signals for determining cloud segments of sufficient signal intensity to be used for retrieving the calibration ratio [51].

### 3.2.2 LITE Retrieval Results for the $C_{1064}/C_{532}$ Calibration Ratio

The  $C_{1064}/C_{532}$  calibration ratio retrieval approach outlined in section 3.2.1 was applied using LITE data for the nighttime portions of orbits 23, 24 and 27. The search for cloud returns was restricted to the altitude region from 8 to 17 km above ground. This helps eliminate noncirrus cloud returns and facilitates the modeling of transmission terms in the retrieval equations. The screening threshold level,  $R_t$  was set to 50, insuring strong cloud returns, permitting minimal horizontal averaging on only 10 shots (~7 km horizontal extent) to still yield a signal uncertainty typically within about  $\pm 2\%$ . Also, only the highest altitude cloud with a thickness (as determined by the threshold signal) of at least 180 meters was used for each 10-shot average. Fig. 3.8 shows the relationship between the retrieved calibration ratios,  $C_{1064}/C_{532}$ , and the latitudes spanned by an orbit, corresponding to orbits 23, 24 and 27, respectively. For orbit 23, 61 cloud profiles (each set being a 10 shot average) met the signal selection requirements specified for the retrievals. For orbits 24 and 27, 29 and 111 cloud profile sets, respectively, were used for retrievals. There appears to be slightly greater scatter in the points for higher latitudes (perhaps due to greater variability in cloud microphysical properties), but this does not appear to be statistically significant. The numerical results (means and standard deviations) for the  $C_{1064}/C_{532}$  calibration ratio retrievals are listed in Table 3.3.

From this table, it can be seen that the calibration ratio for the three nearly adjacent LITE orbits, 23, 24 and 27, is very consistent with small standard deviations within  $\pm 3\%$ . In addition, the calibration ratio of these orbits agrees with the calibration ratio obtained from LITE ground reflections over Edwards dry lake bed (during orbit 24)

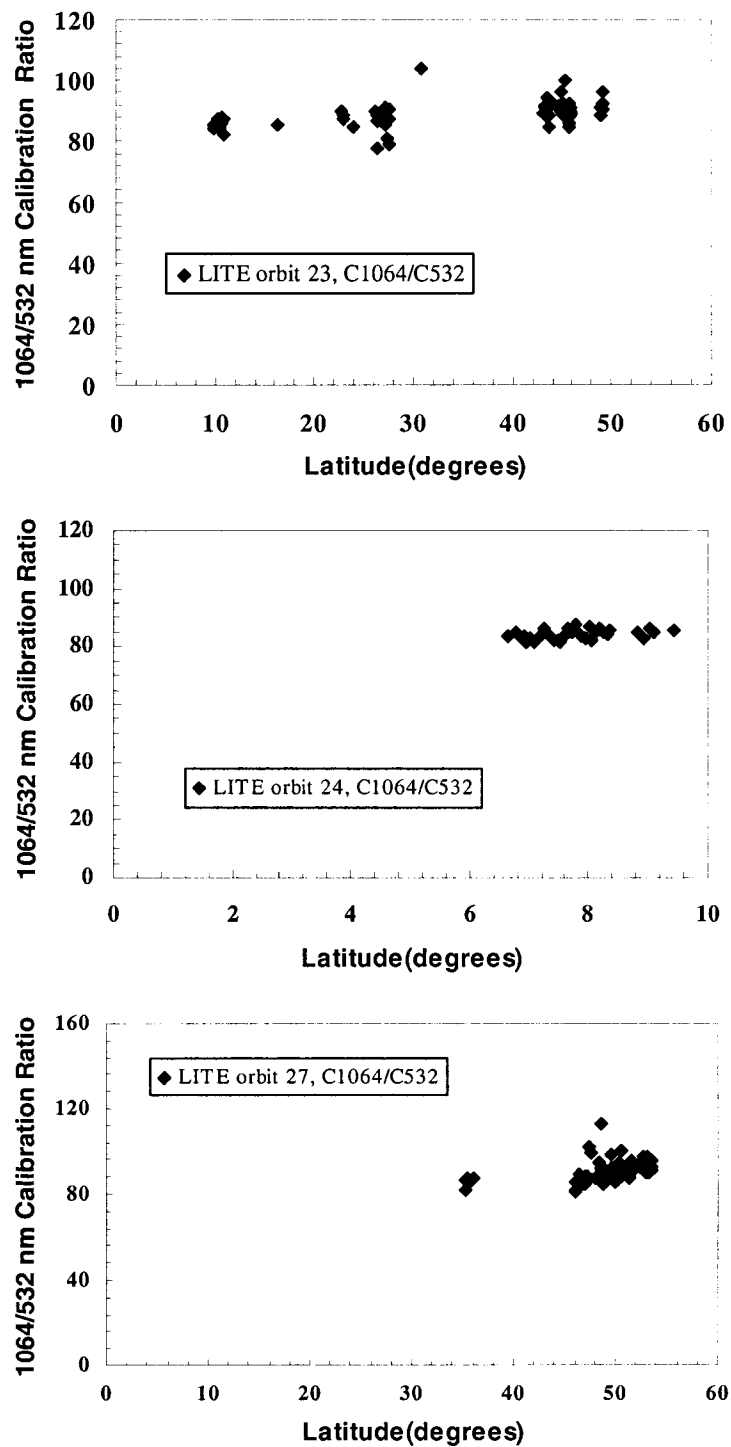


Fig. 3.8. Retrieved 1064/532 calibration ratios from selected cirrus cloud returns for (a) orbit 23, (b) orbit 24, and (c) orbit 27 [51].

within uncertainties for the ground reflection calibration retrieval [19]. The calibration ratio,  $C_{1064}/C_{532}$ , obtained at Edwards AFB, CA was about  $79 \pm 8$ .

Table 3.3 Calibration ratio  $C_{1064}/C_{532}$  for LITE orbits 23, 24 and 27

Orbit	Calibration Ratio $C_{1064}/C_{532}$	Number of Cloud Profiles
23	$88.1 \pm 2.3$	61
24	$85.3 \pm 1.5$	29
27	$88.5 \pm 2.6$	111

### 3.2.3 1064 nm Channel Calibration for CALIPSO

The 1064 nm calibration algorithm, developed by using the LITE database, has been applied to the simulated CALIPSO signals. Fig. 3.9 shows the flow chart of the 1064 nm CALIPSO calibration. Some orbits of LITE data were selected to run through the CALIPSO simulator to obtain the simulated CALIPSO 1064 nm signals with the correct averaging resolution and expected noise characteristics [74]. The data from LITE orbits 23, 24 and 27, obtained with low gain settings, had a sufficient number of unsaturated calibration quality cloud returns to test the 1064 nm calibration algorithm. The resulting calibration constants,  $C_{1064}$ , obtained based on CALIPSO simulated data from LITE orbit 23, are shown in Fig. 3.10 with respect to maximum 532 nm scattering ratio, altitude of 532 nm peak scattering ratio and latitude, respectively [74]. Fig. 3.10a is a plot of the 1064 nm calibration constant versus the peak 532 nm scattering ratio for each calibration cloud profile. It can be seen that the calibration constant is relatively

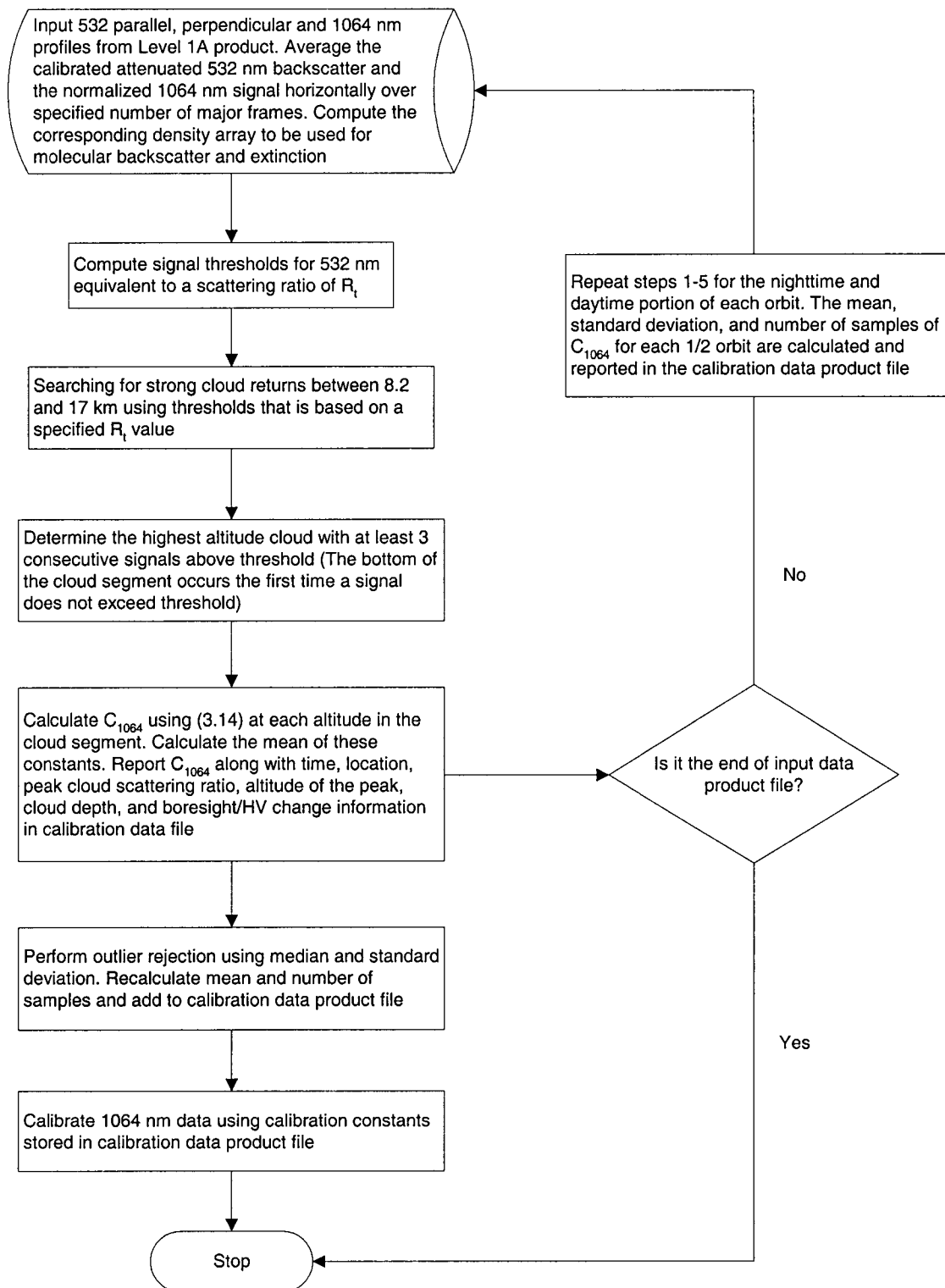


Fig. 3.9. The operational algorithm flow chart for 1064 nm calibration.

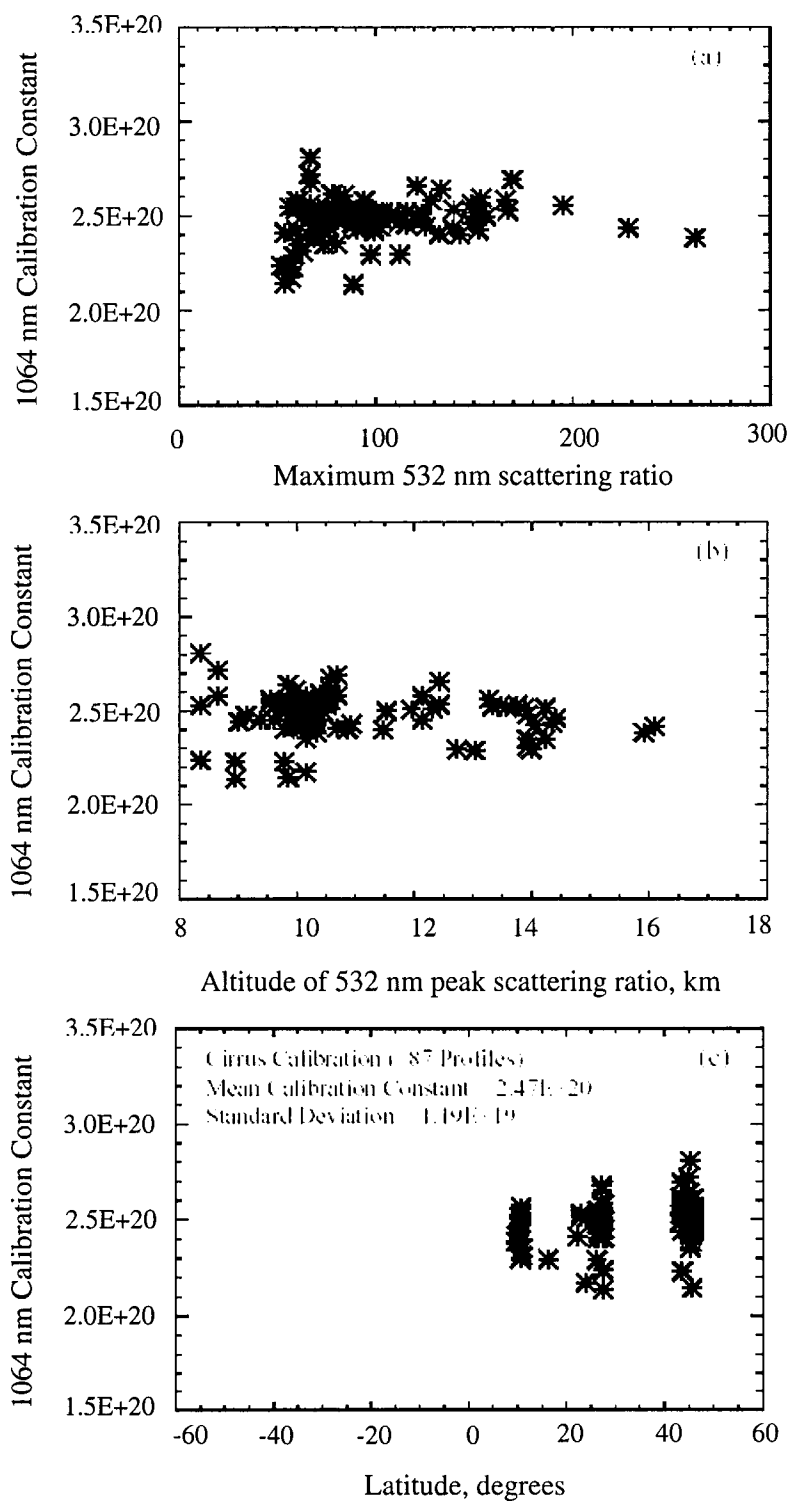


Fig. 3.10. The 1064 nm calibration constant,  $C_{1064}$  versus: a) maximum 532 nm cloud scattering ratio; b) altitude of peak 532 nm cloud scattering ratio; c) latitude of calibration cloud profiles for CALIPSO simulation of LITE orbit 23 [74].

stable with cloud scattering intensity, although there is more variability with weaker clouds. Fig. 3.10b shows that the calibration constant is relatively independent of cloud altitude. The latitudes where the calibration clouds were obtained are shown in Fig. 3.10c, and the calculated 1064 nm calibration constants for orbits 23, 24 and 27 are given in Table 3.4. The same increase in scatter with latitude noted with Fig. 3.8 can be seen in Fig. 3.10c. The calculated 1064 nm calibration constants in Table 3.4 show that the mean calibration constant estimated for each orbit is within about 4% of the simulator calibration value of  $2.49\text{E}+20$  with outlier rejection (rejection of all calibration points outside one standard deviation of the median). The relative uncertainties of the calculated 1064 nm calibration constants are on the order of 5% without outlier rejection. These results are consistent with the expected uncertainties discussed above. The results also show that the outlier rejection should further improve results.

Table 3.4. Calculated 1064 nm calibration constant using CALIPSO simulated data.

<b>LITE orbit #</b>	<b>No Outlier Rejection</b>	<b>Outlier Rejection</b>
Orbit 23	$2.47\text{E}20 \pm 1.19\text{E}19$ (87 profiles)	$2.49\text{E}20$ (66 profiles)
Orbit 24	$2.36\text{E}20 \pm 1.24\text{E}19$ (38 profiles)	$2.39\text{E}20$ (34 profiles)
Orbit 27	$2.48\text{E}20 \pm 9.97\text{E}18$ (160 profiles)	$2.50\text{E}20$ (115 profiles)

### 3.2.4 Error Analysis of the 1064 nm Calibration Approach

Assuming the current parameters for CALIPSO, the expected signal to noise ratio (SNR) for single shot returns at about 11 km above ground from cirrus clouds with backscatter 50 times greater than the 532 nm molecular backscatter, for a 180 m vertical range bin, is  $\text{SNR} \approx 5$  for both 532 and 1064 nm. Averaging over 5km (15 shots)

horizontally should yield an SNR of about 20, or a signal uncertainty (1/SNR) of about 5%, which reduces the signal uncertainty to a small enough level to apply fairly stringent statistical discriminants to reject “contaminated” or “atypical” horizontal cirrus cloud segments. Averaging over additional horizontal segments and/or vertical range bins should further reduce signal uncertainties as demonstrated by the LITE examples.

Including the possibility of some difference between  $\beta T^2$  for 532 nm and 1064 nm within the cloud ( $r > r_{ct}$ ), the ratio of the calibration constants may be expressed as

$$\frac{C_{1064}}{C_{532}} = \frac{X_{1064}}{X_{532}} \times \frac{T_{ct,532}^2}{T_{ct,1064}^2} \times \chi' \quad (3.16)$$

where

$$\chi' = \frac{\beta_{532}}{\beta_{1064}} \times \frac{T_{r>r_{ct},532}^2}{T_{r>r_{ct},1064}^2} \quad (3.17)$$

and

$\beta_\lambda$  = total cloud and noncloud backscatter

$T_{r>r_{ct},\lambda}^2$  = total two-way transmittance from  $r$  to  $r > r_{ct}$ .

Applying standard error propagation analysis to (3.16), the relative uncertainty in  $C_{1064}$  can be expressed as

$$\left[ \frac{\delta C_{1064}}{C_{1064}} \right]^2 = \left[ \frac{\delta X_{1064}}{X_{1064}} \right]^2 + \left[ \frac{\delta X_{532}}{X_{532}} \right]^2 + \left[ \frac{\delta T_{ct,532}^2}{T_{ct,532}^2} \right]^2 + \left[ \frac{\delta T_{ct,1064}^2}{T_{ct,1064}^2} \right]^2 + \left[ \frac{\delta C_{532}}{C_{532}} \right]^2 + \left[ \frac{\delta \chi'}{\chi'} \right]^2 \quad (3.18)$$

Conservative estimates for the error terms in (3.18) are given above in Table 3.5, along with the resulting error in  $C_{1064}$ . Hence, it appears quite feasible to determine  $C_{1064}$  within

$\pm 10\%$  using the cirrus cloud ratio approach. Given the ratio results from the LITE data analysis, it is anticipated that the  $C_{1064}$  calibration uncertainty that can be achieved for CALIPSO may more likely be less than  $\pm 10\%$ .

Table 3.5 Uncertainty estimates of the 1064 nm calibration constant and related parameters.

$\frac{\delta C_{1064}}{C_{1064}}$	$\frac{\delta X_{1064}}{X_{1064}}$	$\frac{\delta T_{ct,532}^2}{T_{ct,532}^2}$	$\frac{\delta X_{532}}{X_{532}}$	$\frac{\delta T_{ct,1064}^2}{T_{ct,1064}^2}$	$\frac{\delta C_{532}}{C_{532}}$	$\frac{\delta \chi'}{\chi'}$
0.097	0.05	0.02	0.05	0.002	0.05	0.04

#### 4. CABANNES VERSUS RAYLEIGH SCATTERING AND TERRESTRIAL BACKSCATTER RATIO REVISITED IN LITE IN SUPPORT OF CALIPSO

In the application of lidar for atmosphere remote sensing, the returned signal usually consists of Rayleigh scattering and vibrational Raman scattering from molecules as well as Mie scattering from aerosol and clouds. Depending on the filter bandwidth of the lidar receiver, the shifted pure rotational Raman scattering signal may or may not be included in the measured lidar return signal. In order to determine the molecular scattering components that the CALIPSO narrow-band lidar receiver should pass, the spectral structure of molecular scattering (strength and bandwidth) and its constituent spectra associated with Rayleigh and vibrational Raman scattering have been assessed to characterize these constituent contributions versus bandwidth. In addition, a model has been developed to simulate the relationship between the molecular depolarization factor and the receiver filter bandwidth. For polarized incident light, the depolarization factor for Cabannes and Rayleigh scattering are 0.0036 and 0.0141, respectively [22, 73]. The CALIPSO receiver filter bandwidth is 0.3 nm. Even though this bandwidth is much wider than the estimated Cabannes bandwidth, 0.002 nm, the simulation results show that the depolarization factor for only Cabannes scattering can be applied for the CALIPSO receiver bandwidth with negligible resulting error.

For lidar calibration via Rayleigh normalization, it is often convenient to obtain the calibration constant in terms of the backscatter ratio  $R$  defined as the ratio of the total

backscatter to molecular backscatter, as indicated earlier in (3.1). But this normalization process is also a source of uncertainty in derived data products. The commonly used value,  $R_{\min} = 1$ , can sometimes lead to significant error [16], particularly when applied to lower altitude, supposedly clean air regions. In this Chapter, data from LITE orbits, 24, 83, 103 and 146 have been analyzed to recover estimates of R characteristic of clean air regions. Errors in recovering R due to uncertainties in the calibration constant obtained at a higher altitude reference height, and the two-way transmission from the calibration reference height, are simulated and assessed based on standard error-propagation procedures.

#### 4.1 Spectrum of Light Scattering by Major Species in the Atmosphere

Molecular scattering consists of Rayleigh scattering and vibrational Raman scattering. The Rayleigh scattering portion consists of rotational Raman lines and the central Cabannes line. The Cabannes line is composed of the Brillouin doublet and the central Gross or Landau-Placzek line [20]. When excited off resonance, an atom that is in the ground state (spherically symmetric) scatters light elastically. The cross section of the atom can be calculated quantum mechanically. For those atoms that do not rotate or vibrate, there can be no sidebands in the scattering spectrum. For a molecule in its electronic ground state that rotates and vibrates, these motions lead to inelastic scattering and yield a characteristic scattering spectrum. For diatomic molecules, such as nitrogen and oxygen, there are two independent parts in the polarizability, the isotropic part and the anisotropic part, whose squares are proportional to cross sections of polarized (coherent) and depolarized (incoherent) scattering, respectively. Polarized scattering is

not affected by molecular rotation, but the rotational motion of the molecule will affect molecular anisotropic scattering. In this case, the scattering due to molecular anisotropy can be separated into three branches in the frequency spectrum, the unshifted branch, Q, and the shifted branches, O and S. The blueshifted and redshifted sidebands, O and S, correspond to anti-Stokes and Stokes pure rotational Raman scattering. For the central Cabannes line, it consists of the polarized scattering and the unshifted (or Q branch) depolarized scattering. The rotational Raman scattering refers to the O- and S-branch sidebands of the depolarized scattering only.

As pointed out by C.Y.She [79], the width of the Cabannes line and the Rayleigh spectrum at 0.5  $\mu\text{m}$  are  $0.083\text{ cm}^{-1}$  and  $200\text{ cm}^{-1}$ , which correspond to wavelength bandwidths of 0.002 nm and 5.66 nm, respectively. The normalized (to unity) relative intensities for the three branches of the depolarized (pure rotational) scattering spectrum are shown in Fig. 4.1 for the atmosphere, which consists of 79% nitrogen and 21% oxygen. In most case, only the relative strength of each scattering line resulting from rotational and vibrational motions has been discussed. However, each scattering line by itself is actually a frequency spectrum, which can be well approximated by a broadband (temperature- and pressure-broadened) spectral line shape. A normalized Cabannes spectrum at 532 nm for the atmosphere at 275 K and 0.75 atm is shown in Fig. 4.2. Kinetic theory can be employed to calculate the temperature and the pressure dependence of the Cabannes spectrum, such as in Tenti et al. [80].

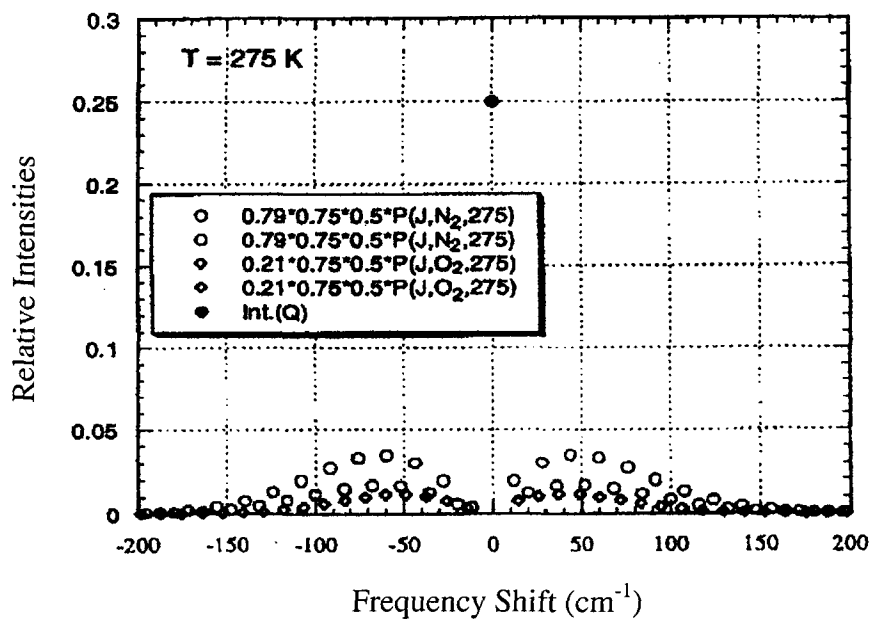


Fig. 4.1 Normalized (to unity) relative intensities for the three branches of the depolarized (pure rotational) scattering spectrum of the atmosphere [79].

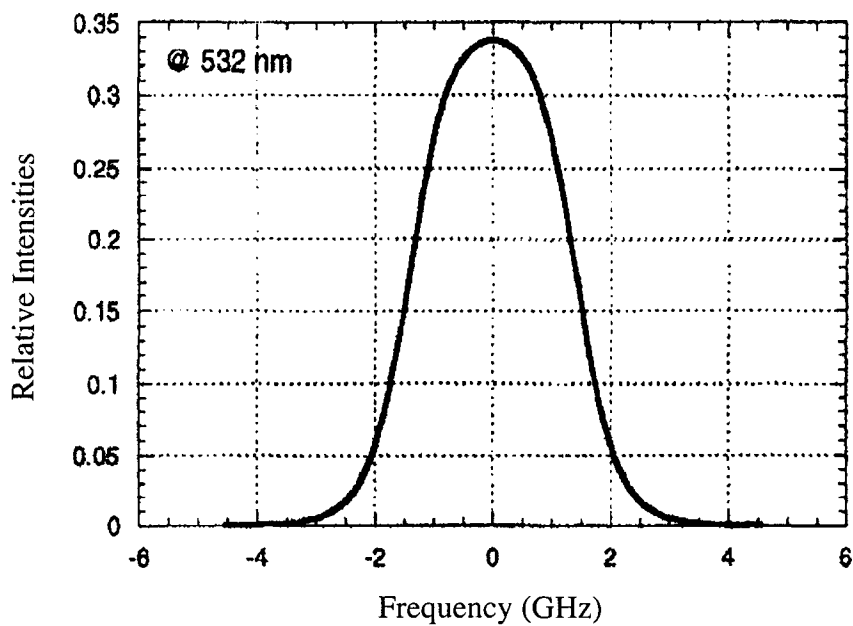


Fig. 4.2 Normalized Cabannes spectrum at 532 nm for the atmosphere at 275 K and 0.75 atm [79].

## 4.2 Modeling and Analysis of the Depolarization Factor

Rayleigh scattering is valid for an ensemble of isotropic spherical particles. Due to the anisotropic characteristics of molecules which comprise air (principally  $N_2$  and  $O_2$ ), the polarizability of a molecule will depend on its orientation relative to the direction of the incident light. For diatomic molecules, the polarizability reduces to parallel and perpendicular components.

In practice, it may be supposed that anisotropy prevents the dipole moment from aligning itself exactly with the electric vector of the primary incident light wave. However, molecular anisotropy can be accounted for by considering molecular scattering to be a combination of true Rayleigh and isotropic scattering [81] through the use of a depolarization factor. The depolarization factor is slightly wavelength-dependent and is different for different molecules [25]. Since there are several ways of defining the depolarization factor [82], some care is required in reading the literature. For Rayleigh scattering, the total scattering irradiance,  $I_s$ , at a distance  $r$  from a molecule can be divided into components that are polarized parallel ( $I_s^{\parallel}$ ) and perpendicular ( $I_s^{\perp}$ ) to the scattering plane (defined by the unit propagation vectors  $\vec{k}_i$  and  $\vec{k}_s$ , see Fig. 2.2). The most common definition for the depolarization factor is given by

$$\delta = \frac{I_s^{\perp}}{I_s^{\parallel}} \quad (4.1)$$

where in this instance the perpendicular and parallel signs refer to the plane of polarization of the incident linearly polarized light beam [70].

For molecular scattering,  $\delta$  is related to the anisotropy in the polarizability of the molecules. It is introduced into scattering theory by the expression  $\frac{6+3\delta}{6-7\delta}$ , applied as a multiplier to any of the standard coefficients. Considering the anisotropic properties of the scattering molecules, the Rayleigh scattering cross section per molecule is modified to take the more general form given by (3.2) [22]. In the case of isotropic scatterers such as monatomic gases like argon,  $\delta=0$ .

Referring to Fig. 4.1, a mathematic model was developed to characterize the relationship between the spectral bandwidth (i.e., receiver filter bandwidth) and the depolarization factor. Based on the shape of the spectrum, the relationship between the depolarization factor and the filter bandwidth can be modeled as a cubic polynomial. This is based on the fact that the depolarized scattering will increase rapidly at first and then reach the maximum increasing rate when the boundaries of the receiver filter bandwidth cross the points where the strength of the rotational Raman scattering is at the maximum. After the peaks of the rotational Raman lines have been passed, the rate of increase of the depolarization observed will decrease and eventually become zero when the boundaries of the receiver filter bandwidth reach the full extent of the Rayleigh scattering spectrum.

The modeled relationship between the depolarization factor and the receiver filter bandwidth is given by

$$\delta = \zeta_0 + \zeta_1 B_f + \zeta_2 B_f^2 + \zeta_3 B_f^3 \quad (4.2)$$

where  $\delta$  is the depolarization factor and  $B_f$  represents the receiver filter bandwidth (the full filter bandwidth, centered on the unshifted incident wavelength). The rate of increase in  $\delta$  with  $B_f$  is then given by

$$\frac{d\delta}{dB_f} = \zeta_1 + 2\zeta_2 B_f + 3\zeta_3 B_f^2 \quad (4.3)$$

As seen from Fig. 4.1, the increasing rate,  $\frac{d\delta}{dB_f}$ , reaches its maximum when  $B_f \approx 100$   $\text{cm}^{-1}$ , which results in

$$\frac{d^2\delta}{dB_f^2} = 2\zeta_2 + 6\zeta_3 B_f = 0 \quad (4.4)$$

which yields,

$$\zeta_2 = -300\zeta_3 \quad (4.5)$$

When  $B_f \approx 400$   $\text{cm}^{-1}$ ,  $\frac{d\delta}{dB_f} = \zeta_1 + 2\zeta_2 B_f + 3\zeta_3 B_f^2 = 0$ ; hence,

$$\zeta_1 = -2.4 \times 10^5 \zeta_3 \quad (4.6)$$

Using the depolarization factors from [22] and the corresponding bandwidths (in units of  $\text{cm}^{-1}$ ) for Cabannes and Rayleigh scattering along with equation (4.2), the following equation set is obtained:

$$0.0141 = \zeta_0 + 400\zeta_1 + 400^2 \zeta_2 + 400^3 \zeta_3 \quad (4.7)$$

$$0.0036 = \zeta_0 + 0.083 \zeta_1 + 0.083^2 \zeta_2 + 0.083^3 \zeta_3 \quad (4.8)$$

Substituting the values of  $\zeta_1$  and  $\zeta_2$  from (4.5) and (4.6) into (4.7) and (4.8), the values of  $\zeta_3$  and  $\zeta_0$  can be obtained by solving the equation set. With all the values of  $\zeta_0$ ,  $\zeta_1$ ,  $\zeta_2$  and  $\zeta_3$  thus determined, (4.2) may be expressed as

$$\delta = 0.0036 + 3.15E-5B_f + 3.939E-8B_f^2 - 1.313E-10B_f^3 \quad (4.9)$$

Based on (4.9), the depolarization factors have been computed for the receiver filter bandwidths of LITE and CALIPSO, respectively. The results are shown in Fig. 4.3. The modeled depolarization factor for CALIPSO and LITE (daytime) is 0.00394. The receiver filter bandwidth for LITE nighttime measurement is  $\sim 9363 \text{ cm}^{-1}$  (265 nm), which is much wider than the  $400 \text{ cm}^{-1}$  (11.32 nm) of the Rayleigh scattering spectrum.

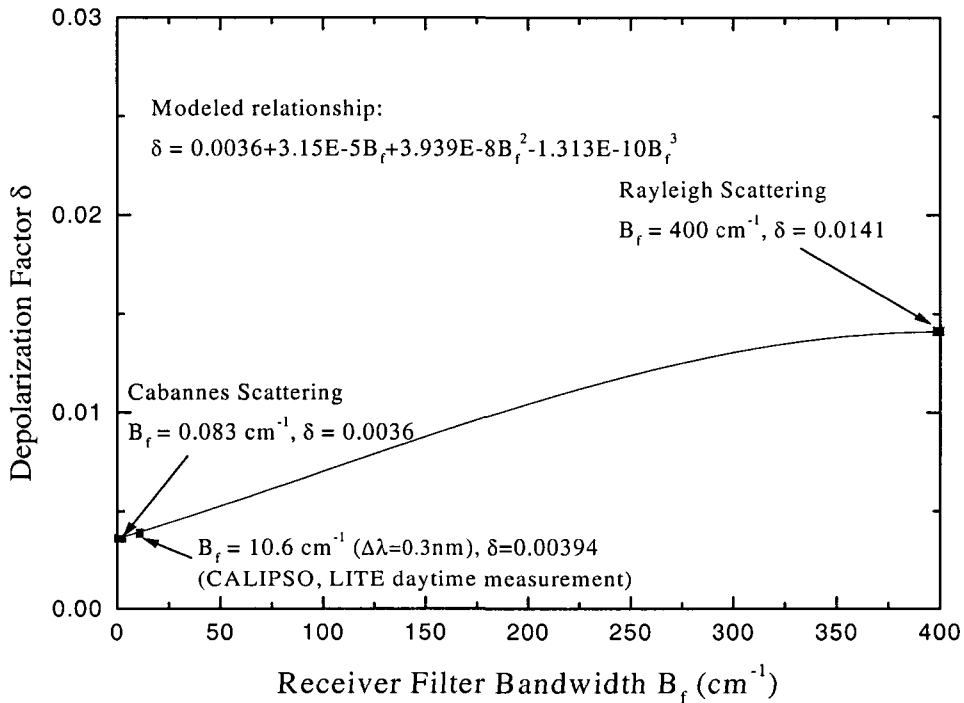


Fig. 4.3. The modeled relationship between depolarization factor and the receiver filter bandwidth (Center wavelength:  $0.5 \mu\text{m}$ ).

The commonly used depolarization factor for full Rayleigh scattering is 0.0279 for unpolarized incident light and a value of 0.0141 [22] for polarized incident light where the incident light refers to the light before molecular scattering occurs. The depolarization factor used for CALIPSO is 0.0036. Fig. 4.3 shows that the use of the modeled depolarization factor for CALIPSO, 0.00394, makes little difference versus using the well-known depolarization factor, 0.0036, which is for only Cabannes scattering. Even though the relative difference between the modeled depolarization factor for CALIPSO, 0.00394, and the commonly used depolarization factor for Cabannes scattering, 0.0036, is about 9.4%, it's the anisotropy correction factor,  $F_K$ , that more correctly reflects the error resulting from the uncertainty of depolarization factor in calibration. The expression for  $F_K$  is given as  $F_K = (6+3\delta)/(6-7\delta)$ , where  $\delta$  is the depolarization factor. The calibration constants at 532 nm for LITE orbit 24 (similar to Fig. 3.2, but for a greater latitudinal range) were determined assuming different depolarization factors, and the results are shown in Fig. 4.4. The relative deviations for using different depolarization factors (0.00394, 0.0141 and 0.0279) rather than  $\delta=0.0036$  were also investigated, and the results are shown in Fig. 4.5. The impact of using the commonly accepted depolarization factors, 0.0279 and 0.0141, for the 532 nm calibration in CALIPSO, causes errors about 4% and 2%, respectively. These estimates of the impact upon 532 nm CALIPSO calibration due to the use of inappropriate depolarization factors (0.0279, 0.0141) agree very well with the results reported by She [79].

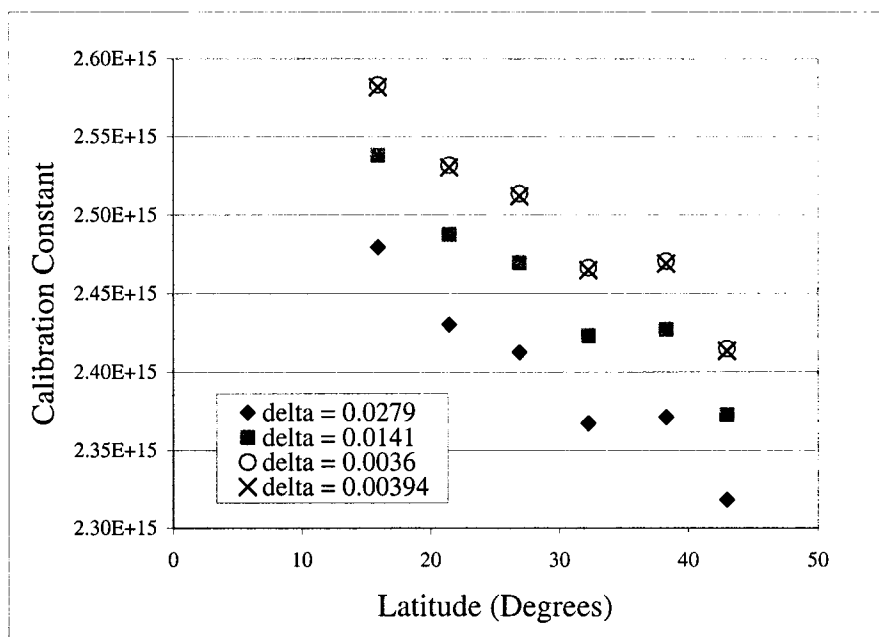


Fig. 4.4. The calibration constants at 532 nm for LITE orbit 24 versus latitudes with different depolarization factors.

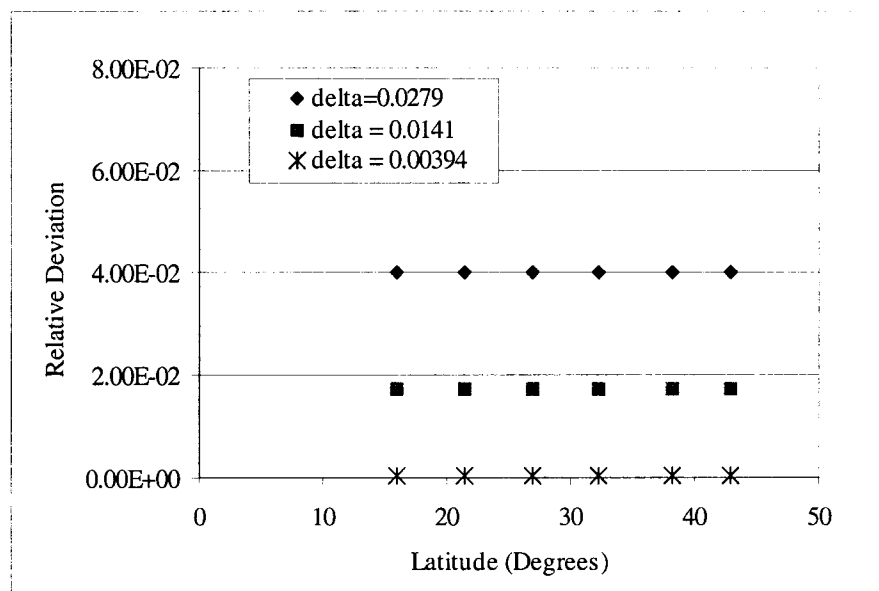


Fig. 4.5. The relative deviation of the calibration constants for LITE orbit 24 with different  $\delta$  at 532 nm comparing with  $C_{532}$  with  $\delta = 0.0036$ .

### 4.3 Error Analysis of the Terrestrial Backscatter Ratio in Support of CALIPSO

In previous sections, the calibration uncertainties at 532 nm due to the use of an incorrect value of the depolarization factor were assessed based on a developed mathematical model and LITE data. In this section, the 532 nm calibration work will be further extended by evaluating the errors of  $R_{\min}$ .

For a downward-looking lidar, if the starting point of the aerosol retrieval can be moved closer to the top of the aerosol layer, the errors in the aerosol retrieval are expected to be lowered significantly with the improved lidar signal to noise ratio (SNR). Another reason is the greater the distance from the starting point, the poorer the retrieval relation becomes. From this point of view, one alternative is to determine the best value and location for  $R_{\min}$  at a significantly lower altitude than  $\sim 30$  km and to calibrate the lidar via Rayleigh scattering normalization at that lower altitude where  $R_{\min}$ , if not exactly one, is at least somewhat bounded close to one.

The problem of determining the best value for  $R_{\min}$  was attacked by Russell and Livingston [16], hereafter referred to as RL. The values of  $R_{\min}$  are highly dependent on latitude, height range, atmospheric condition (volcanic or nonvolcanic) and assumed refractive index. For example, the latitude dependence of  $R_{\min}$  for nonvolcanic conditions (i.e., it has been some time, a few years, since the last major volcanic eruption that injected significant amount of gas and particles into the upper troposphere and stratosphere) had been discussed in more detail by RL [16]. Compared to the data set

used by RL in their study of  $R_{\min}$ , the terrestrial data collected during the LITE mission (a time when there were relatively few volcanic aerosols in the stratosphere) is more up to date and of greater global extent. Therefore, a further investigation of the upper atmosphere, clean air terrestrial backscatter ratio is now more feasible and can provide more useful information in support of the coming CALIPSO mission.

The normalization of the ratio  $R(z)$  is operationally performed by searching for the minimum value of  $R(z)$  in the altitude range where the lidar signal, two-way transmission and Rayleigh backscattering coefficients are sufficiently well known. Here,  $z$  is the altitude and it relates to the range  $r$  with  $z = z_L - r$  where  $z_L$  has been defined before (again, see Fig. 3.1). The height where  $R(z)$  reaches its minimum is called the normalization height, or calibration reference height, which is designated as  $z^*$  in this chapter.

As indicated earlier in (3.1), it is often convenient to obtain the calibration constant in terms of the backscatter ratio  $R_{\min}(z^*)$ . The process of finding  $R_{\min}(z^*)$  via the normalization of the ratio  $R(z)$  is also a source of uncertainty for the calibration at lower altitude due to the error/uncertainty transferring of the product,  $CT^2(r)$  from a higher altitude,  $z_c$ , to lower altitude,  $z^*$ . From (3.1), the product  $CT^2(z^*)$  can be written as

$$CT^2(z^*) = \frac{X(z^*)}{\beta_R(z^*)R_{\min}(z^*)} \quad (4.10)$$

In the following sections, the error analysis of  $R_{\min}(z^*)$  will be discussed in more detail.

### 4.3.1 Error Analysis

Recall in Chapter 3, Section 3.1.2, the standard error propagation analysis was applied to the  $C_{532}$  retrieval equation. This section gives a more detailed derivation of the standard error propagation. For a function  $f$ , derived from several measured variables  $x$ ,  $y$ , ..., the uncertainty in  $f$  can be approximated as [83, 84]

$$(\delta f)^2 = (\delta x)^2 \left( \frac{\partial f}{\partial x} \right)^2 + (\delta y)^2 \left( \frac{\partial f}{\partial y} \right)^2 + 2\sigma_{xy}^2 (\delta x)(\delta y) \left( \frac{\partial f}{\partial x} \right) \left( \frac{\partial f}{\partial y} \right) + \dots, \quad (4.11)$$

where  $\delta x$  is the uncertainty in the measured variable  $x$ , and  $\sigma_{xy}^2$  is the covariance between the measured variables  $x$  and  $y$ . This covariance can be expressed mathematically as

$$\sigma_{xy}^2 = \lim_{n \rightarrow \infty} \frac{1}{n} \sum [(x_i - \bar{x})(y_i - \bar{y})], \quad (4.12)$$

where  $\bar{x}$ ,  $\bar{y}$  are the mean measured values for  $x$  and  $y$ , and  $x_i$  and  $y_i$  are the values obtained in a particular measurement  $i$ . The covariance  $\sigma_{xy}^2$  vanishes when measurement errors  $(x_i - \bar{x})$  are uncorrelated with errors  $(y_i - \bar{y})$ , but is nonzero if these errors are correlated.

In applying (4.11) to (4.10), the first consideration is which, if any, covariance term is nonzero. Due to the different methods of determination (or assumption), there is no basis for correlation among  $X$ ,  $\beta_R$  and  $R_{\min}$ ; hence, the corresponding covariances are all zero. However,  $\beta_R(\lambda, z)$  values at different heights  $z_1$ ,  $z_2$  will be correlated if  $|z_1 - z_2|$  is less than the height resolution of the density measurement (or model) used to derive  $\beta_R(\lambda, z)$ . This is because the profile  $\beta_R(\lambda, z)$  for the height resolution used in the lidar analysis is usually obtained by interpolating between measurements (or a model) having

coarser resolution. In (4.10), all variables involved are at the same altitude,  $z^*$ . Thus, the covariance term in (4.11) can be ignored when applying (4.10), which yields

$$\{\delta[CT^2(z^*)]\}^2 = [\delta X(z^*)]^2 \left( \frac{\partial[CT^2(z^*)]}{\partial X(z^*)} \right)^2 + [\delta\beta_R(z^*)]^2 \left( \frac{\partial[CT^2(z^*)]}{\partial\beta_R(z^*)} \right)^2 + [\delta R_{\min}(z^*)]^2 \left( \frac{\partial[CT^2(z^*)]}{\partial R_{\min}(z^*)} \right)^2 \quad (4.13)$$

where errors in determining height have been assumed to be negligible.

Based on (4.10), substituting the appropriate partial derivatives yields

$$\{\delta[CT(z^*)^2]\}^2 = [\delta X(z^*)]^2 \left( \frac{CT(z^*)^2}{X(z^*)} \right)^2 + [\delta R_{\min}(z^*)]^2 \left( \frac{CT(z^*)^2}{R_{\min}(z^*)} \right)^2 + [\delta\beta_R(z^*)]^2 \left( \frac{CT(z^*)^2}{\beta_R(z^*)} \right)^2 \quad (4.14)$$

After rearranging, the relative uncertainty in  $CT^2(z^*)$  becomes

$$\frac{\delta[CT^2(z^*)]}{CT^2(z^*)} = \left[ \left( \frac{\delta X(z^*)}{X(z^*)} \right)^2 + \left( \frac{\delta R_{\min}}{R_{\min}} \right)^2 + \left( \frac{\delta\beta_R(z^*)}{\beta_R(z^*)} \right)^2 \right]^{\frac{1}{2}} \quad (4.15)$$

As seen in the one-type or two-type scatterer retrieval relations given earlier, the product of the calibration constant and the two-way transmission at a reference height  $z_c$ ,  $CT^2(z_c)$ , is more important than the calibration constant itself.

The total relative error in  $CT^2(z^*)$  contains contributions from signal measurement error, Rayleigh backscattering coefficient error and error in the estimates of  $R_{\min}$ . To provide some additional background for the statistical relations and considerations involved in this error analysis, the following sub-section presents explicit expressions for these terms.

### 4.3.2 Signal Measurement Error

For a series of  $M$  measurements of a variable  $v$ , the mean value of  $v$  from this series of measurement is

$$\bar{v} = \frac{1}{M} \sum_{i=1}^M v_i \quad (4.16)$$

where  $v_i$  represents the  $i^{\text{th}}$  measurement. The sample variance of the measurement is

$$\sigma_v^2 = \frac{1}{M} \sum_{i=1}^M v_i^2 - \bar{v}^2 \quad (4.17)$$

The uncertainty in a measurement  $v$  is represented by the standard deviation,  $\sigma_v$ , given by

$$\sigma_v = [\sigma_v^2]^{1/2} \quad (4.18)$$

From the quantum standpoint, the radiant energy received by a lidar system actually can be viewed as a bunch of photons. These photons generate a pulse of electrons within the detector. If a series of measurements were undertaken under essentially identical circumstances the inherent quantum nature of the radiation would mean that the number of photon-generated electrons (photoelectrons) would fluctuate in such a way that the probability of generating  $m_e$  electrons (or electron-hole pairs for a semiconductor detector) was

$$P(m_e, \bar{m}_e) = \frac{\bar{m}_e^{m_e}}{m_e!} e^{-\bar{m}_e} \quad (4.19)$$

where  $\bar{m}_e$  represents the mean number of the generated electrons in this series of measurements. Eq. (4.19) is a Poisson distribution and it is easily shown that for such a

statistical distribution, the uncertainty  $\sigma_{m_e}$  in the mean signal in a series of  $M$  measurements is given approximately by [84]

$$\sigma_{m_e} = \sqrt{\frac{\overline{m_e}}{M}} \quad (4.20)$$

The received lidar signal for one transmitted laser pulse of energy  $E$  at wavelength  $\lambda$ , expressed in received unmultiplied photoelectrons,  $n_s(r)$ , from backscattering with a range bin  $\Delta r$ , centered at a distance  $r$  may be easily derived from (1.1) or (1.2) and can be expressed by

$$n_s(r) = \left( \frac{\lambda \eta_\lambda}{hc} \right) \frac{EA_R \Delta r \beta(r) F_o(\lambda)}{r^2} \exp \left[ -2 \int_0^r \sigma(r') dr' \right] \quad (4.21)$$

where  $\eta_\lambda$  is the detector quantum efficiency,  $h$  is Planck's constant,  $c$  is the speed of light,  $F_o(\lambda)$  is the system optical efficiency and the exponential term describes the atmospheric round-trip transmittance. The range  $r$  can be replaced by altitude  $z$  and equation (4.21) can be rewritten as

$$n_s(z) = \frac{\Delta z EA_r F_o(\lambda)}{(z_L - z)^2} \left( \frac{\lambda \eta_\lambda}{hc} \right) \beta(z) T^2(z) \quad (4.22)$$

where  $T^2(z) = \exp \left[ -2 \int_z^{z_L} \sigma(z) dz \right]$ . The signal to noise ratio, SNR, for  $M$  pulses can be obtained from Eq. (4.20) by

$$SNR(z) = \frac{n_s(z)}{\sigma_{n_s}(z)} = \frac{n_s(z)}{\sqrt{\frac{n_s(z)}{M}}} = \sqrt{M} \sqrt{n_s(z)} \quad (4.23)$$

which is the limiting noise due to signal, and, thus, maximum SNR that can be achieved for measurements made during a dark night and for a detector which has a very low dark current. Otherwise, including the background and dark noise contents,  $n_{BD}$ , the SNR is given by

$$SNR(z) = \frac{n_s(z)}{\sqrt{\frac{n_s(z) + n_{BD}(z)}{M}}} \approx \sqrt{M} \sqrt{n_s(z)} \text{ if } n_s(z) \gg n_{BD}(z). \quad (4.24)$$

The relative uncertainty of the signal is equal to the inverse of SNR, or,

$$\frac{\delta X(\lambda, z)}{X(\lambda, z)} = \frac{1}{SNR(\lambda, z)} \quad (4.25)$$

At the altitude of ~30 km above ground, the relative uncertainty in the normalized signal with 200 shot average is in the range of 3%. Based on (4.21) and (4.23), the signal to noise ratio (SNR) for a 100 shot horizontal average is simulated by using the LITE system parameters as listed in Table 2.1. In the simulation, the total backscattering coefficient,  $\beta(r)$ , and the two-way transmission coefficient,  $T^2(r)$ , are replaced by  $\beta_{R,532}(r)$  and  $T_{R,532}^2(r)$ . A typical measured nighttime SNR for the 532 nm LITE channel, for orbit 83, for a 100 shot horizontal average, is also calculated based on (4.24) for comparison with the simulated SNR. The SNR results from simulation and LITE measurements are shown in Fig.4.6. The slightly greater SNR of the measurements versus the simulated SNR for lower altitudes is not unexpected and assumed to be due to the presence of some aerosols which contribute to a signal greater than that due only to Rayleigh scattering.

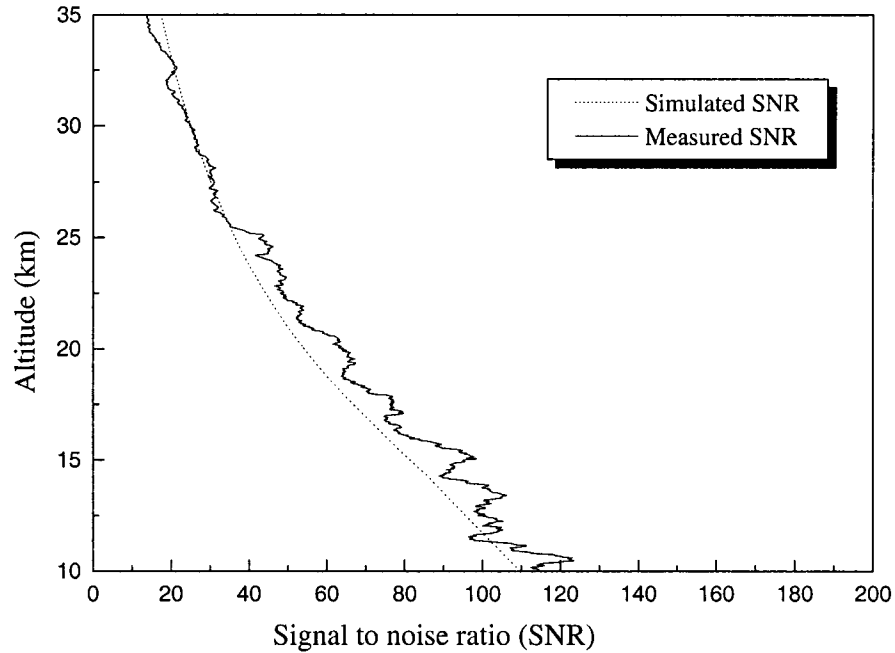


Fig. 4.6. The SNR results from simulation and LITE measurements for 100 shots horizontal average.

#### 4.3.3 Rayleigh Backscattering Coefficient Error

The Rayleigh backscattering coefficients can be calculated by (3.3) and the related error sources have been analyzed in Chapter 3, Section 3.1.1. At the altitude of ~30 km above the ground, the Rayleigh backscattering coefficient,  $\beta_{R,532}(r)$ , can be estimated within about  $\pm 3\%$  uncertainty [51]. Using temperature and pressure meteorological data incorporated in the LITE or CALIPSO databases, the error for  $\beta_{R,532}(r)$  at lower altitude (e.g., 8 – 14 km) can be manageably small. For example, with molecular number densities calculated from pressure and temperature fields derived from

assimilated network measurements, the error of  $\beta_{R,532}(r)$  at these lower altitudes can be reasonably estimated within  $\sim 1.5\%$  [16, 51].

#### 4.3.4 Errors in the Estimates of $R_{\min}$

The estimated uncertainties in the backscatter ratio  $R(z)$  at a lower altitude  $z^*$ ,  $R_{\min}$ , are actually partially influenced/related to the error of the product,  $CT^2(z_c)$ , at a higher altitude ( $z = 30\sim 34$  km). Recall that the backscatter ratio,  $R(z)$ , is given by

$$R(z) = \frac{\beta_a(z) + \beta_R(z)}{\beta_R(z)} \quad (4.26)$$

The two-type scatterer approach, retrieval equation (2.27), can be used to retrieve the aerosol back scattering coefficients,  $\beta_a(z)$ . However, there is an unknown,  $S_a$ , in this equation. In the stratosphere and in much of the remote upper troposphere, the dominant constituent (whether from biogenic, anthropogenic, or volcanic sources) is a solution of sulfuric acid in water with an approximate mass ratio of 3:1 [85-87]. Mie calculations for this aerosol composition show that for the range of size distributions likely to be encountered in the stratosphere and upper troposphere, the extinction-to-backscatter ratio lies in the range 20-50 sr at 532 nm, the lower values being associated with larger particles [88]. Two values of  $S_a$ , 25 and 40, were selected for the investigation in this chapter. This choice reflects the fact that above the calibration reference height,  $z^*$ , the sky is generally clean for which the  $S_a$  values reasonably fall within the abovementioned range.

When doing the aerosol retrievals with the given  $S_a$  values (25, 40) and the retrieval relation, (2.27), it was observed that the retrieved aerosol backscattering

coefficients,  $\beta_a(z)$ , at some altitudes can be negative, a physically unrealistic situation. Kent et al. [88] did their aerosol retrievals by assuming a range of values for  $S_a$  in the troposphere in a search for a physically meaningful solution. But the values for  $S_a$  employed in the stratosphere still corresponded to a sulfuric acid solution ( $S_a = 20 \sim 50$ ). In addition, their investigation was more focused on the unrealistic solutions which appeared consistently in some of their aerosol retrievals (i.e., the scattering ratio,  $R$ , was equal or less than unity for a segment of  $R$  profile). For the investigations in this chapter, the aerosol retrievals are more focused on the clean region above the troposphere. Furthermore, the negative retrieval results occurred randomly rather than continuously compared to the retrieval results reported by Kent et al. [88]. One possible reason to account for these physically unrealistic solutions is because the random error of the signal can affect the total backscatter signal significantly at some altitudes, where the total backscatter signal can be smaller than the Rayleigh backscatter signal. This in turn can lead to a negative retrieval result at some altitude. One solution to avoid these negative retrieval results is to set the retrieved aerosol backscattering coefficients to be zero, which is a quite reasonable approach in dealing with the random errors of the signal.

The LITE data for orbits 24, 83, 103 and 146 have been investigated to recover estimates of  $R$  characteristic of clean air regions (i.e., regions where  $\beta_a(z)$  is near a minimum). The LITE signals were processed horizontally with a 100-shot average and vertically with a 300-meter average, which is equivalent to 20 range bins, to increase the signal to noise ratio, SNR. Errors in recovering  $R$  resulting from the uncertainties in the

calibration constant determined at a higher altitude and the two-way transmission from this calibration reference height were simulated and assessed.

With the obtained relative uncertainties of  $R_{\min}$ ,  $\beta_R(z)$ ,  $X(z)$  at the calibration height,  $z^*$ , the relative uncertainty of  $CT^2(z^*)$  for 532 nm can be evaluated. A flow chart is shown in Fig. 4.7 for the simulation of the relative uncertainty of  $CT^2(z)$  at the calibration reference height,  $z^*$ . Figs 4.8 to 4.11 show the errors of  $R_{\min}$ , which are influenced by the uncertainties of  $CT^2(z)$  at higher altitude ( $z = \sim 30$  km), lidar signal and Rayleigh backscattering coefficients. The results presented in these figures are for three aerosol types, continental (orbit 24, 103), Sahara dust layer (orbit 83) and biomass burning (orbit 146), insofar as the types of aerosols in the lower troposphere well below the height of  $R_{\min}$ . As such, the difference in these aerosol types should have little influence on the value of  $R_{\min}$ . At the lower altitude, the molecular backscattering error can be reduced due to better determination of the atmosphere density. Assuming the relative uncertainty of  $\beta_R(z)$  at  $z^*$  is  $\sim 2\%$ , the relative uncertainty of  $R_{\min}$  at  $z^*$  is  $\sim 3\%$  and the relative uncertainty of  $X(z)$  at  $z^*$  is  $\sim 1\%$ , the resultant relative uncertainty of  $CT^2(z^*)$  is  $\sim 3.7\%$ . This value is actually lower than the relative uncertainty of  $CT^2(z)$  at  $\sim 30$  km above the ground, which is  $\sim 3.9\%$  based on the error analysis in Chapter 3.

By averaging the parameters in Table 4.1, which correspond to  $S_a = 25$  and  $40$ , respectively, some mean values (i.e. averaged  $R_{\min}$  for  $S_a = 25$  and  $40$ ) are obtained to represent a typical value within the limits determined by  $S_a = 25$  and  $40$ . The results given in Table 4.1 have shown that for orbit 24 an averaging has been applied to a horizontal extent of  $\sim 1200$  km or over latitudes  $30.7$  to  $38.8$  N. The averaged  $R_{\min}$  for

orbit 24,  $S_a = 25$  and 40, is 1.02. For orbit 103, a horizontal average was applied over an extent of  $\sim 1100$  km, or over latitudes 30.4 to 37.5 N and the averaged  $R_{\min}$  for  $S_a = 25$  and 40 is 1.019. The mean value of  $R_{\min}$  for orbit 83,  $S_a = 25$  and 40, is 1.01 by averaging horizontally over  $\sim 1500$  km, or over latitudes 19.2 to 29.5 N. Similarly, the mean value of  $R_{\min}$  for orbit 146,  $S_a = 25$  and 40, is 1.04 by averaging horizontally over  $\sim 1200$  km, or over latitudes 26.6 to 17.9S.

In summary, the results given in Table 4.1 have shown that for most of the cases (orbit 24, 83 and 103) the mean value of  $R_{\min}$  is below 1.03 and the relative uncertainty of  $R_{\min}$  is lower than 3%. The relative uncertainty of the lidar signals,  $X(z^*)$ , is lower than 1% and the relative uncertainty of  $\beta_R(z^*)$  is  $\sim 2\%$ . The simulated relative uncertainty of  $CT^2(z^*)$  for most of the cases is lower than 3.9%, except that the relative uncertainty of  $CT^2(z^*)$  for orbit 146 ( $S_a = 40$ ) is a little higher. The  $R_{\min}$  values and their corresponding uncertainties, combined with the uncertainty analysis for other parameters (i.e. the uncertainty analysis for  $X(z^*)$ ,  $\beta_R(z^*)$  etc.), show that the Rayleigh normalization at a lower altitude,  $z^*$ , can be used as a backup or alternative check for the calibration of the 532 nm channel (the parallel polarization channel). The altitudes of  $R_{\min}$  in Table 4.1 are between 11 and 13 km, which are within the range,  $\sim 8$  to 16 km above ground where the minimum backscatter ratio is generally observed. Even though the  $R_{\min}$  value for orbit 146,  $S_a = 40$ , is a little higher ( $R_{\min} = 1.05$ ), the average relative uncertainty of  $CT^2$  at  $z^*$  for  $S_a = 40$  is 4.08%, which is still within an acceptable range compared to 3.9%. The average relative uncertainty of  $CT^2$  at  $z^*$  for  $S_a = 25$  and 40 is 3.57%, which is just below 3.9%.

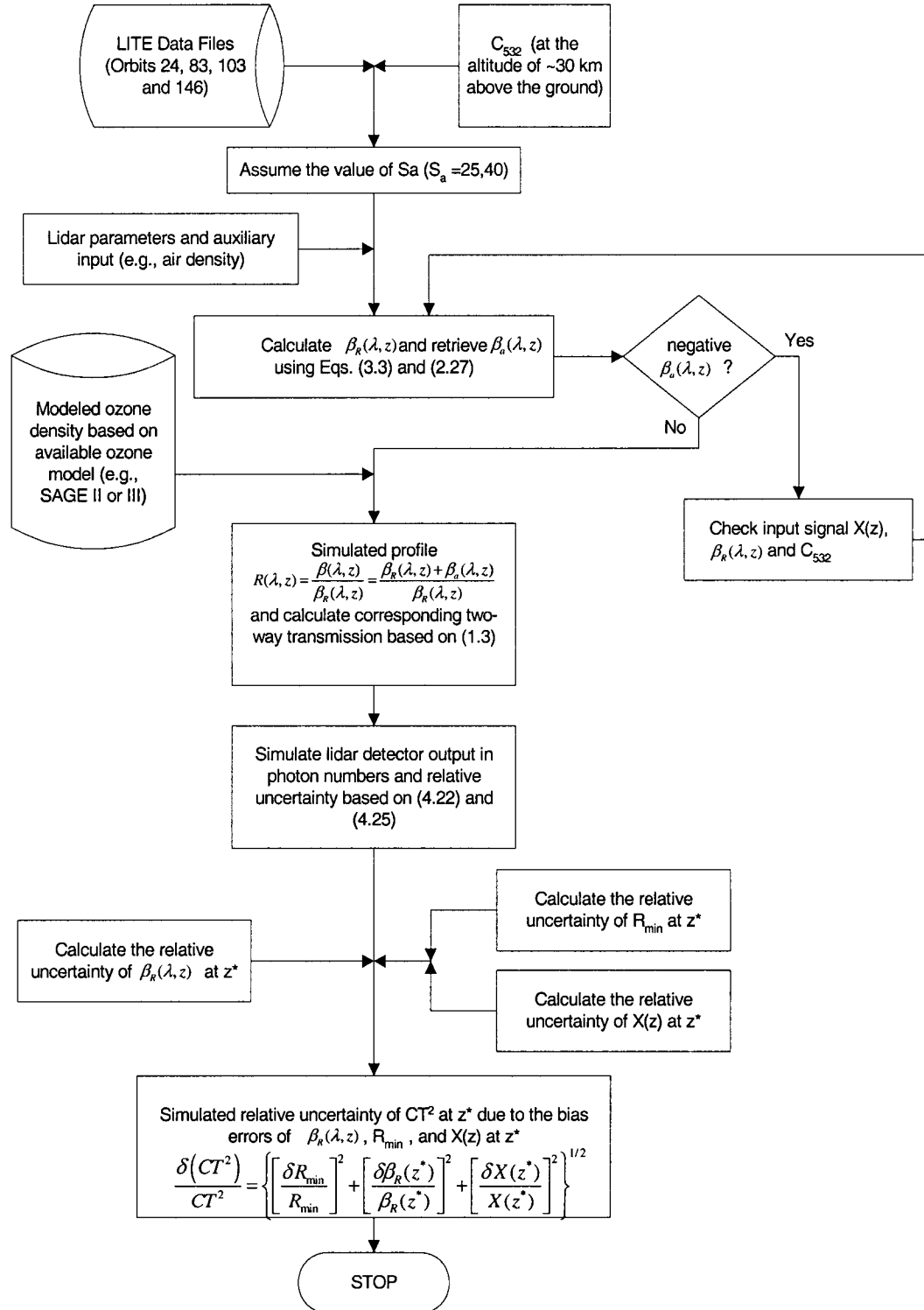


Fig. 4.7 Simulation procedure for evaluating the relative uncertainty of  $CT^2$  at  $z^*$ .

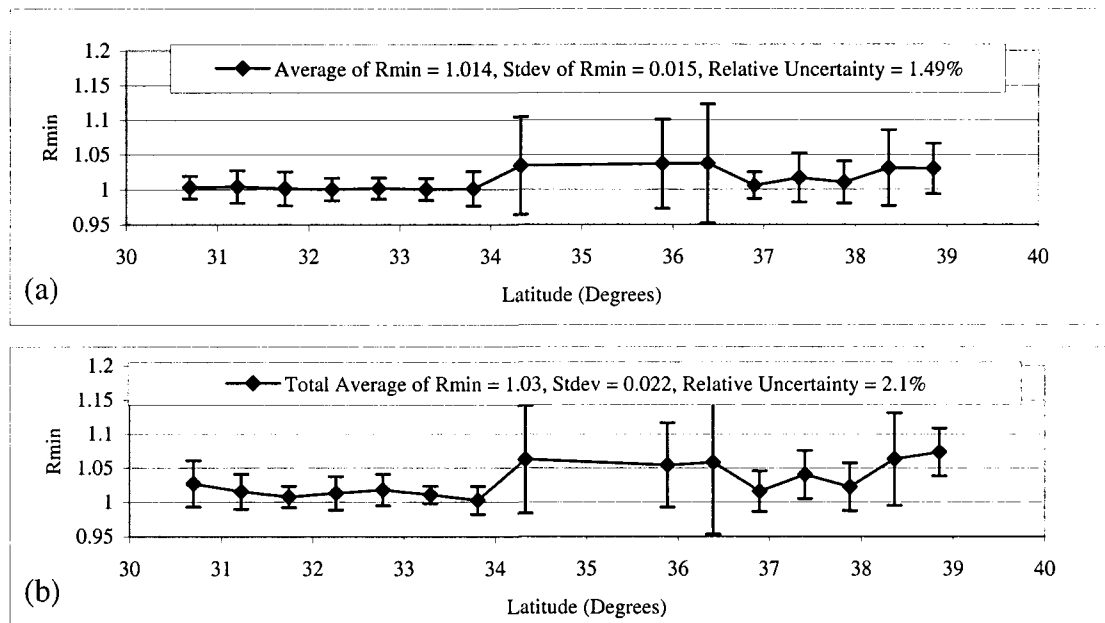


Fig. 4.8. The relationship of  $R_{min}$  versus latitudes with regard to different  $S_a$  values for orbit 24. (a)  $S_a=25$ ; (b)  $S_a=40$ .

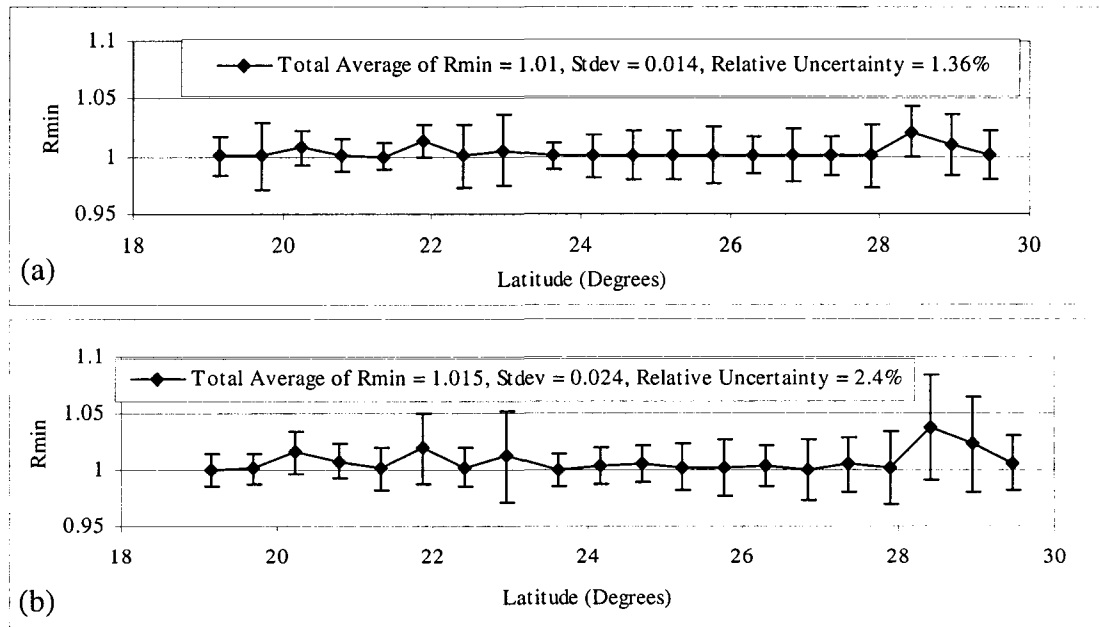


Fig. 4.9. The relationship of  $R_{min}$  versus latitudes with regard to different  $S_a$  values for orbit 83. (a)  $S_a=25$ ; (b)  $S_a=40$ .

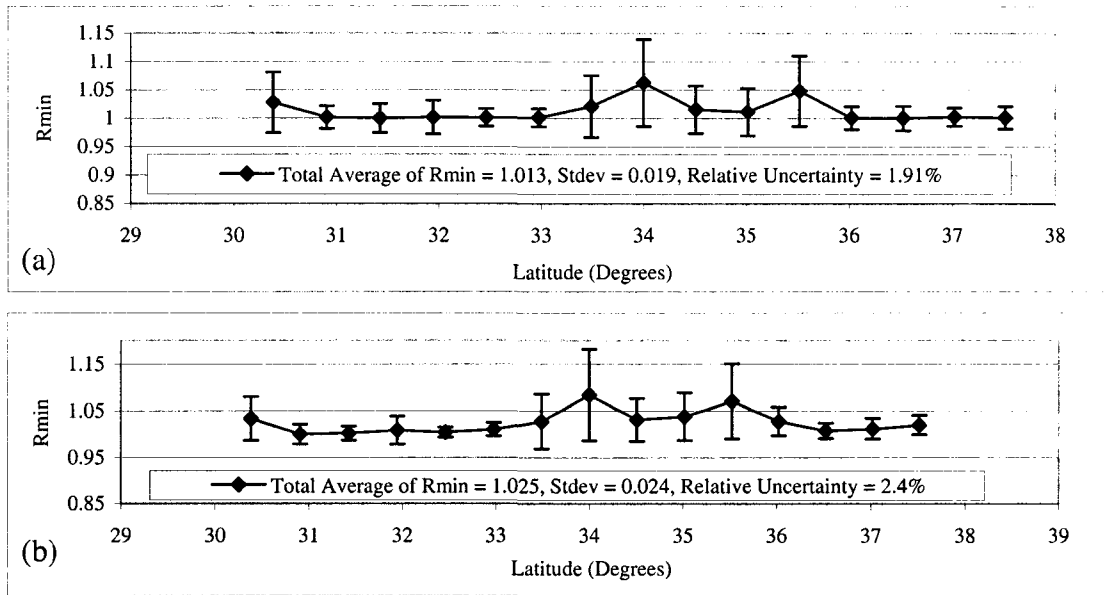


Fig. 4.10. The relationship of  $R_{min}$  versus latitudes with regard to different  $S_a$  values for orbit 103, (a)  $S_a=25$ ; (b)  $S_a=40$ .

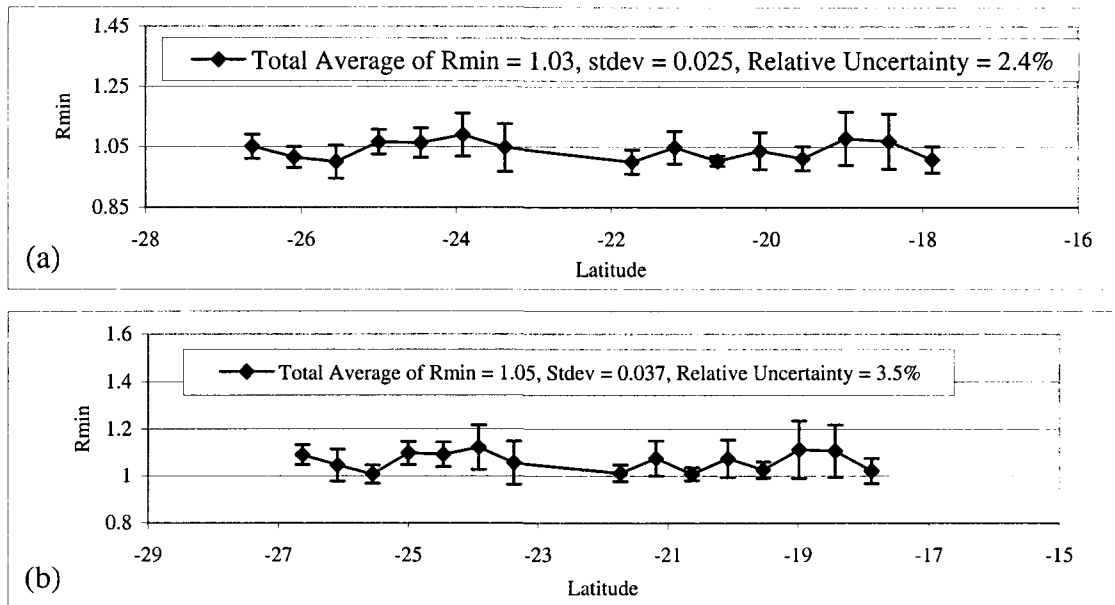


Fig. 4.11. The relationship of  $R_{min}$  versus latitudes with regard to different  $S_a$  values for orbit 146, (a)  $S_a=25$ ; (b)  $S_a=40$ .

Table 4.1. The relative uncertainties of  $R_{\min}(z^*)$ ,  $X(z^*)$ ,  $\beta_R(z^*)$  and  $CT^2(z^*)$  with  $S_a = 25$  and 40.

	<b>Orbit 24</b> <b>Latitude:</b> <b>30.7~38.8N</b> <b>Range:</b> <b>~1200 Km</b>	<b>Orbit 83</b> <b>Latitude:</b> <b>19.2~29.5N</b> <b>Range:</b> <b>~1500 Km</b>	<b>Orbit 103</b> <b>Latitude:</b> <b>30.4~37.5N</b> <b>Range:</b> <b>~1100 Km</b>	<b>Orbit 146</b> <b>Latitude:</b> <b>26.6~17.9S</b> <b>Range:</b> <b>~1200 Km</b>
Average of $R_{\min}$ , $S_a = 25$	1.014	1.01	1.013	1.03
Average of $R_{\min}$ , $S_a = 40$	1.03	1.015	1.025	1.05
Relative Uncertainty of $R_{\min}$ (%), $S_a = 25$	1.49	1.36	1.91	2.4
Relative Uncertainty of $R_{\min}$ (%), $S_a = 40$	2.1	2.4	2.4	3.5
<b>Average <math>R_{\min}</math> for <math>S_a = 25</math> and <math>S_a = 40</math></b>	1.02	1.01	1.019	1.04
<b>Average Relative Uncertainty of <math>R_{\min}</math> for <math>S_a = 25</math> and <math>S_a = 40</math> (%)</b>	1.8	1.88	2.2	2.95
<b>Average Altitude of <math>R_{\min}</math>, <math>z^*</math>, for <math>S_a = 25</math> and <math>S_a = 40</math> (km)</b>	11.51	11.74	12.01	12.95
Average Relative Uncertainty of Signal at $z^*$ , $S_a = 25$ (%)	0.99	0.97	0.94	0.94
Average Relative Uncertainty of Signal at $z^*$ , $S_a = 40$ (%)	1.0	1.0	0.95	0.94
<b>Average Relative Uncertainty of Signal at <math>z^*</math> for <math>S_a = 25</math> and <math>S_a = 40</math> (%)</b>	0.995	0.985	0.945	0.94
Relative Uncertainty of $\beta_R(z)$ at $z^*$ with $S_a = 25$ (%)	1.90	2.01	1.81	1.71
Relative Uncertainty of $\beta_R(z)$ at $z^*$ with $S_a = 40$ (%)	1.94	2.14	2.01	1.90
<b>Average Relative Uncertainty of <math>\beta_R(z)</math> at <math>z^*</math> for <math>S_a = 25</math> and <math>S_a = 40</math> (%)</b>	1.92	2.08	1.91	1.81
Relative Uncertainty of $CT^2$ at $z^*$ with $S_a = 25$ (%)	2.61	2.62	2.79	3.06
Relative Uncertainty of $CT^2$ at $z^*$ with $S_a = 40$ (%)	3.06	3.38	3.27	4.08
<b>Average Relative Uncertainty of <math>CT^2</math> at <math>z^*</math> for <math>S_a = 25</math> and <math>S_a = 40</math></b>	2.84	3.0	3.03	3.57

## 5. UNCERTAINTY ANALYSIS OF EXTINCTION-TO-BACKSCATTER RATIO IN LITE AEROSOL RETRIEVAL

In this chapter, the simulations to estimate various uncertainties in the aerosol retrieval are presented. Sensitivity of the retrievals for the aerosol backscattering coefficient caused by the use of an inaccurate assumed extinction-to-backscatter ratio,  $S_a$ , calibration factor,  $C$ , normalized lidar signal,  $X(z)$ , and Rayleigh backscattering profile,  $\beta_R(z)$ , are assessed and analyzed. By using revised calibration approaches and techniques/models, the range of  $S_a$  values was investigated with actual LITE data (orbits 24, 83 and 103) and simulated lidar signals for the typical aerosol elevated layer model and boundary layer model. In the following sections, the retrieval results from LITE for  $S_a$ ,  $\beta_a$  and  $\sigma_a$  do not account for or correct for multiple scattering, which are very significant and will be demonstrated in Chapter 7.

### 5.1 Aerosol Retrieval Uncertainty Analysis

Russell et al. [16] have extensively discussed and evaluated the major error sources affecting retrieval of the aerosol backscattering coefficient. For their treatment of the two types of scatterer atmosphere (i.e., both molecular and aerosol scattering important), they assumed the total relative error in the retrieved backscattering coefficient had contributions from the signal measurement error, the range error, the two-way transmission error, the molecular-density error, and the error in the assumed value of  $R_{\min}$ . However, the uncertainty in the aerosol extinction-to-backscatter ratio,  $S_a$ , which is usually known either poorly or not at all, was not included. The simulation method

introduced here includes the various  $S_a$  uncertainties, such as bias  $S_a$  and random  $S_a$  errors. Hence, it provides a more complete estimate of the uncertainty in the retrieved aerosol backscattering coefficient. In this aerosol retrieval uncertainty analysis, the aerosol backscattering coefficient is retrieved by using the general two types of scatterer solution to the lidar equation [67].

The uncertainty in the retrieved aerosol backscattering coefficient,  $\delta\beta_a(z)$ , can be simulated by using the aerosol retrieval relation, such as (2.27) or some equivalent relation, and introducing the uncertainties in the variables  $X(z)$ ,  $C$ ,  $S_a$  and  $\beta_R(z)$ , where  $z$  is the altitude. In performing the simulation of the uncertainty in  $\beta_a(z)$ , both random and bias errors must be considered.

For the simulation, it is assumed that any variable in the two-type scatterer solution (2.27) is composed of two parts: the true vector  $x$  of the quantity of interest and an error vector  $\mathcal{E}$ , such that the variable vector  $\hat{x}$  [e.g.,  $\hat{\beta}_R(z)$ ,  $\hat{S}_a$ ,  $\hat{X}(z)$ , etc.] is

$$\hat{x} = x + \mathcal{E} \quad (5.1)$$

Each random error  $\mathcal{E}_i$  is assumed to be drawn from a normal distribution with mean zero and standard deviation  $\mu_i$ .

Applying this notation to (2.27) yields

$$\hat{\beta}_a(z) = \frac{\hat{X}(z) \exp \left[ -2(\hat{S}_a - \hat{S}_R) \int_0^z \hat{\beta}_R(z') dz' \right]}{\hat{C} - 2\hat{S}_a \int_0^z \hat{X}(z) \exp \left[ -2(\hat{S}_a - S_R) \int_0^{z'} \hat{\beta}_R(z'') dz'' \right] dz''} - \hat{\beta}_R(z) \quad (5.2)$$

The calibration factor  $\widehat{C}$ , which is actually the product of  $CT^2(z_c)$  where  $z_c$  is the calibration reference height, can be obtained by (3.1) and the error  $\Delta C$  can be calculated by (4.15).

The aerosol extinction-to-backscattering ratio,  $S_a$ , can be treated in two ways: one is to assume that the relative uncertainty in  $S_a$  is due to a random error source represented by  $\widehat{S}_a$ , and the other is to assume  $S_a$  has some bias error. For a bias error,  $\delta S_a$ ,  $\widehat{S}_a = S_a \pm \delta S_a$ . The normalized signal is treated in similar fashion with a mean equal to the averaged signal  $X(z)$  and a standard deviation  $\mu_x(z)$ .

The Rayleigh backscattering profile  $\widehat{\beta}_R(z)$  was set equal to the exact value of  $\beta_R(z)$ , plus a random error that varies with  $z$ , which is drawn from a distribution with mean zero and specified standard deviation. As the uncertainties in  $X(z)$ ,  $C$ ,  $\beta_R(z)$ , and  $S_a$  should be independent, their contribution to the total uncertainty in estimating aerosol backscattering coefficient,  $\beta_a(z)$ , may be combined to yield

$$\mu_{\beta_a}(z) = \sqrt{\delta^2 \beta_a |_{\delta \beta_R} + \delta^2 \beta_a |_{\delta X} + \delta^2 \beta_a |_{\delta C} + \delta^2 \beta_a |_{\delta S_a}^{Random} + \delta^2 \beta_a |_{\delta S_a}^{bias}} \quad (5.3)$$

where  $\delta \beta_a |_{\delta \beta_R}$  is the random error of Rayleigh backscattering coefficient,  $\beta_R$ , which contributes to the total error of aerosol backscattering coefficient,  $\mu_{\beta_a}$ ;  $\delta \beta_a |_{\delta X}$ , is the random error of lidar signal,  $X$ , which contributes to  $\mu_{\beta_a}$ ;  $\delta \beta_a |_{\delta C}$  is the bias error of  $C$  that contributes to  $\mu_{\beta_a}$ ; and  $\delta \beta_a |_{\delta S_a}^{Random}$  and  $\delta \beta_a |_{\delta S_a}^{bias}$  are the random and bias errors of  $S_a$  that contribute to  $\mu_{\beta_a}$  respectively.

## 5.2 Uncertainty Analysis Results and the Investigation of $S_a$ Range

### 5.2.1 Saharan Dust Case

Saharan dust episodes occur in the North Atlantic region during the summer season. These dust events are a result of strong convective disturbances in West Africa producing lifting of dust through several kilometers which is then carried westward, typically at an altitude between one and five kilometers above the surface, by cyclical passages of easterly wave disturbances [89]. The LITE orbit 83, along which a Saharan dust layer is evident between 1 and 4.5 km for a segment of the orbit near/over West Africa, was selected to investigate different sources of errors.

Fig. 5.1 shows a segment of the flight track of orbit 83 during the LITE mission. The color image of attenuated backscatter (i.e.,  $V(z)$ ) for orbit 83 shown in Fig. 5.2 reveals significant Sahara dust structure extending to heights of about 5 km. The thin white-colored layer, speckled with red, underneath the Saharan dust layer marks the lidar beam saturation due to mixed layer clouds and aerosol. Fig. 5.2 also reveals the clean air and near aerosol free region in the upper tropospheric and lower stratospheric region (8 to 15km) where LITE calibrations can be performed.

These figures are composed of individual lidar profiles sampled at 10 Hz along the Space Shuttle orbit tracks during nighttime conditions. The intensities of the returned signal are measured in digitizer counts and correspond to the accompanying color scale which extends from black for the weakest signal through white for the strongest signal.

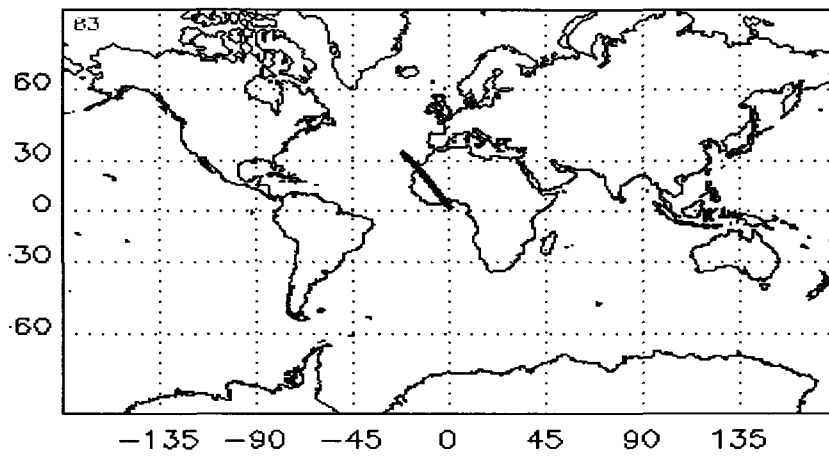


Fig. 5.1. The flight track of orbit 83 during LITE mission in 1994.

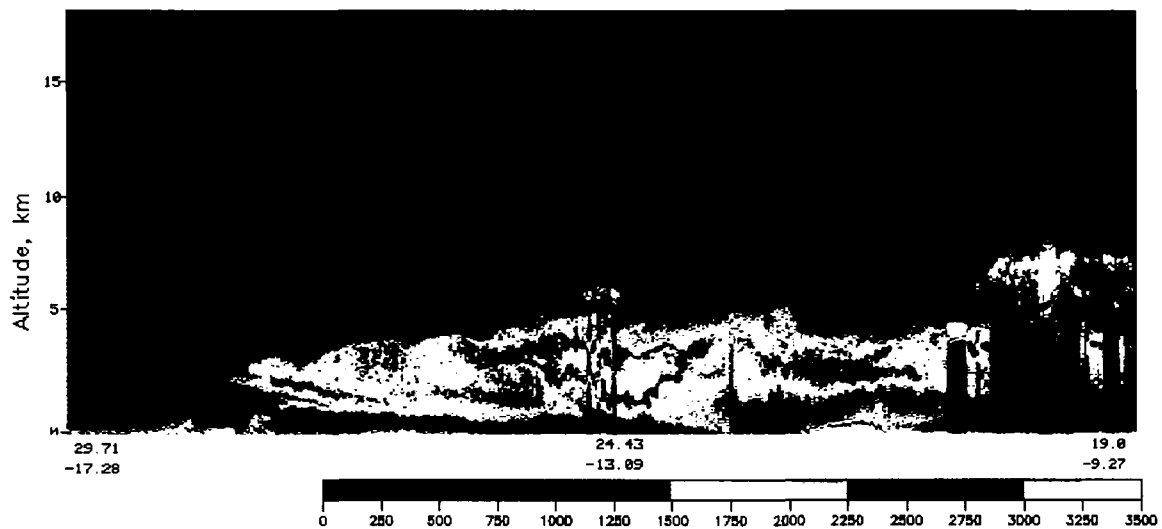


Fig. 5.2. A color image of the Saharan dust structure at different locations.

The value of  $S_a$  at 532 nm for the dust layer was assumed to be  $S_a = 35$  with a bias error of  $\pm 10$  and a random error with a standard deviation of  $\pm 5$ . For the clean air region above/below the dust layer, the value of  $S_a$  is set as  $S_a \approx 25$  with a bias error  $\pm 5$  and a random error with standard deviation of  $\pm 5$ . Error bars in Fig. 5.3 (a) and (b) show the retrieved uncertainty in  $\beta_a(z)$  due to  $\pm$ bias errors of  $C$  and  $\pm$ bias errors of  $S_a$ , where the bias errors of  $C$ , which is  $\sim 4.4\%$ , were calculated based on (4.15). The simulation results show that the uncertainty in  $\beta_a(z)$  due to  $\pm$ bias  $C$  is less than  $\sim 5\%$  and the uncertainty in  $\beta_a(z)$  due to  $\pm$ bias  $S_a$  for most of the dust layer is from  $\sim 5\%$  to  $\sim 20\%$ . The uncertainty in  $\beta_a(z)$  due to  $\pm$ bias  $S_a$  is relatively higher near the dust layer bottom, which could be nearly 30% to 50%.

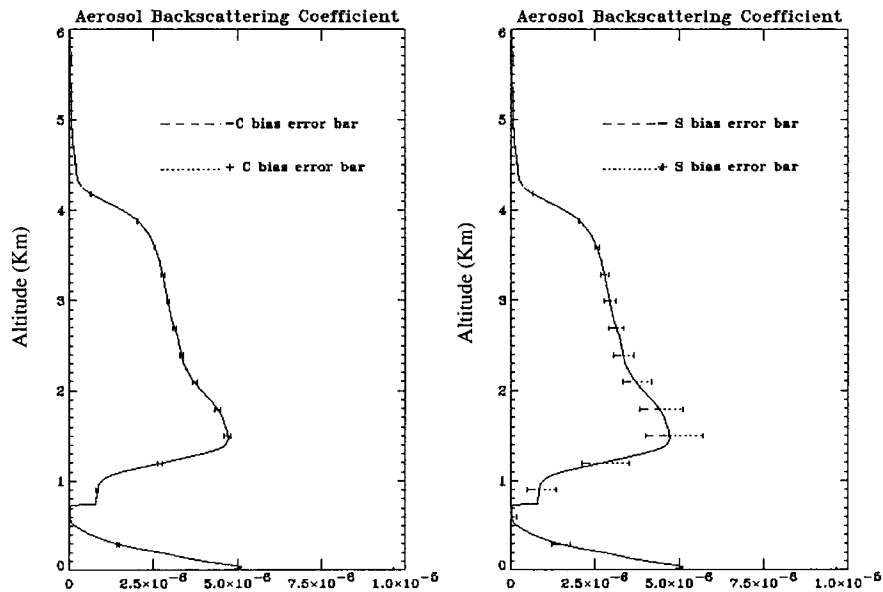


Fig. 5.3. Retrieved uncertainties in  $\beta_a(z)$  for the Saharan dust layer case due to (a)  $\pm$ bias error of  $C$  and (b)  $\pm$ bias error of  $S_a$ .

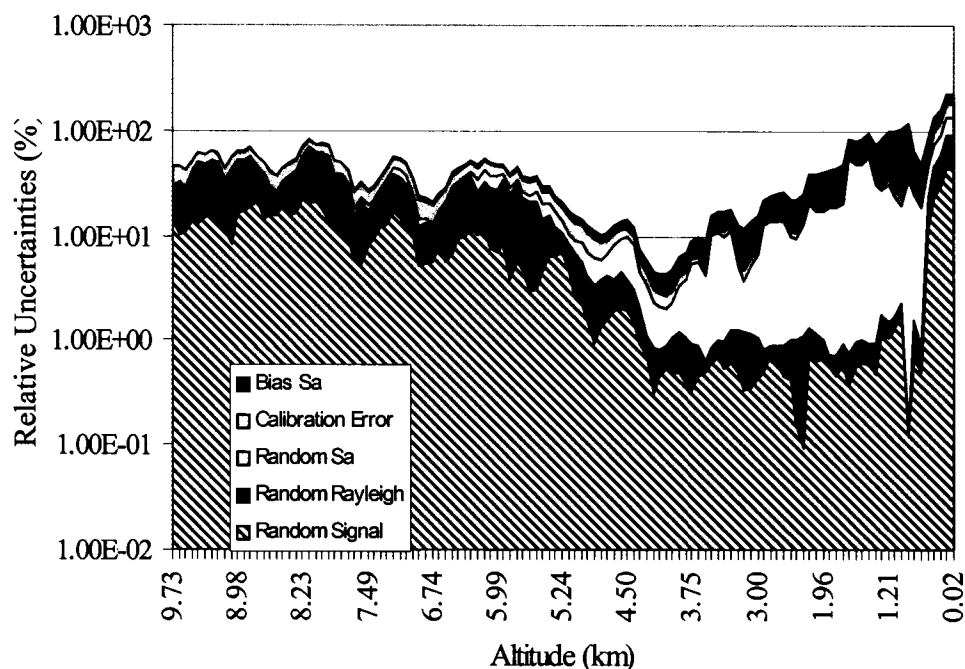


Fig. 5.4. Retrieved relative uncertainties (%) in aerosol backscattering coefficients for Sahara dust layer case broken down by sources, which were defined in Eq. (5.3).

Fig. 5.4 shows how the corresponding relative uncertainties in the retrieved aerosol backscattering profile are broken down due to different sources based on (5.3). The relative uncertainties due to different sources (i.e.,  $S_a$  bias/random error, random error of signals, bias error of  $C$ , random error of  $\beta_R$ ) are represented by different shaded area in Fig. 5.4. The total relative uncertainty in the Saharan aerosol layer (SAL) region, which is represented by the sum of all areas, ranges from about 5% to 100% when considering all errors/uncertainties, including both random error and  $\pm$ bias error in  $S_a$ . From Fig. 5.4, some conclusions can be drawn:

1. The retrieved aerosol backscattering coefficient is not sensitive to the numerical value of the assumed  $S_a$  over the range from the calibration reference height ( $\sim 9.7$ km)

down to the top height of the dust layer ( $\approx 4.3\text{km}$ ). However, in the dust layer and below, for  $S_a$  treated as the bias source, the uncertainty of  $S_a$  is the dominant factor contributing to uncertainty in the retrieval aerosol backscattering coefficient.

2. The calibration factor systematically affects the retrieved aerosol backscattering coefficient from the calibration reference height,  $z_c$ , to the ground and the C bias error is one of the most dominant errors from the calibration reference height,  $z_c$ , to the top of the SAL layer. The C bias error is within  $\pm 15\%$  in the SAL region.

3. Since the measured signal has been averaged over 100 shots which yields an rms SNR of 60 to 170 for heights between the calibration reference height and the ground, signal errors contribute to only a small portion of the total relative uncertainty for the retrieved  $\beta_a(z)$ . The uncertainty in the determined Rayleigh backscattering coefficient also has very little effect in the strong aerosol scattering region, (i.e., the SAL and below). Conversely, in the clean air, near aerosol free region, (i.e., above the SAL), it is the dominant source of error for the retrieved  $\beta_a(z)$ .

### 5.2.2 Continental Case

To verify the accuracy of the measurements made by LITE, a worldwide correlative measurement program was organized as a part of the LITE mission. The Atmospheric Remote Sensing Lab (ASRL) of the university of Arizona participated in this program and obtained correlative measurement results for LITE in several sites in California and Arizona. Measurements of spectral optical depth were made at selected sites under segments of LITE Orbits 24 and 103 by ground based solar radiometers [19]. These auxiliary optical depth measurements make it possible to retrieve aerosol

properties from the LITE 532 and 1064nm channel data, including estimating the aerosol extinction-to-backscatter ratio,  $S_a$ .

For doing the aerosol retrieval, there are many approaches that have been widely reported [9]. In this dissertation, three aerosol retrieval approaches are frequently used, which are Self-Transmittance/isolated layer approach, Aux-Transmittance approach and Modeled- $S_a$  approach. The Self-Transmittance/isolated layer approach is more suitable for the elevated aerosol layer (i.e., Saharan dust layer or biomass burning smoke layer). For this approach, the aerosol layer two-way transmittance,  $T_a^2(r_1 \rightarrow r_2)$ , is estimated from the difference in lidar signal above and below an elevated layer embedded in otherwise clean air. With the obtained  $T_a^2(r_1 \rightarrow r_2)$ , the aerosol backscattering coefficients at 532 nm,  $\beta_{a,532}(z)$ , can be retrieved iteratively by using (2.29) while the aerosol extinction coefficients at 1064 nm,  $\sigma_{a,1064}(z)$ , can be directly obtained by (2.41).

The Aux-Transmittance approach is almost the same as Self-Transmittance method. The only difference is that the estimates of transmittance through a layer are provided by auxiliary transmittance/optical depth retrievals such as those obtained from ground-based solar radiometer measurements (e.g. AERONET) or from passive satellite observations (e.g. MODIS) of upwelling solar reflected/scattered radiance over dark targets. The auxiliary aerosol transmittance is typically obtained for the aerosol mixed boundary layer over the surface.

For the Modeled- $S_a$  approach, a value for  $S_a$  is given based on well-known models. With the given  $S_a$  values, the aerosol backscattering coefficients,  $\beta_{a,532}(z)$ , can be

retrieved by (2.29) while the aerosol extinction coefficients at 1064 nm,  $\sigma_{a,1064}(z)$ , can be directly obtained by (2.40).

The measured aerosol optical depths for LITE orbit 103 ( $\sim 33.73^\circ\text{N}$ ,  $\sim 115^\circ\text{W}$ , where LITE passed over Ford Dry Lake) at 532nm and 1064nm were 0.052 and 0.028, respectively. Applying these optical depth values to the corresponding LITE Orbit 103 profiles, the aerosol extinction coefficients at 532nm and 1064nm were retrieved by the Aux-Transmittance approach and the results are shown in Fig. 5.5. An estimate of  $S_a = 35$  for 1064 nm retrieval was obtained by applying the solar radiometer estimated transmittance to (2.42). With the Modeled- $S_a$  approach, the aerosol backscattering coefficient  $\beta_a(z)$  for 532nm channel can be retrieved by assuming a value for  $S_a$  in (2.27). The aerosol extinction coefficient  $\sigma_a(z)$  can then be determined by  $\sigma_a(z) = S_a\beta_a(z)$ . Integrating  $\sigma_a(z)$  from top of the aerosol layer,  $z_t$ , down to the ground ( $z = 0$ ), yields a first estimate of the aerosol optical depth  $\tau_a$ . This estimated value is compared with  $\tau'_a$  obtained by solar radiometer measurements (in this case, it is 0.052), and  $\sigma_a(z)$  is then recalculated with different trial values of  $S_a$  until  $\tau_a = \tau'_a$ . The iteration procedure yielded  $S_a = 38$  and the corresponding aerosol extinction profile for 532 nm is shown in Fig. 5.5 as solid curve, while the dotted line refers to the extinction profile at 1064 nm.

With the revised relationship between the calibration factor of 1064 nm and 532 nm,  $C_{1064} \approx 87C_{532}$  [51], the aerosol optical depths at different sites for orbits 24 and 103 have been investigated. For orbit 103, the LITE retrieved aerosol optical depths at 532 nm have been calculated with  $S_a = 35$  and 40. The aerosol optical depths at 1064 nm for LITE orbit 103 were retrieved with  $S_a = 30$  and 35, and the results for both 532 and 1064

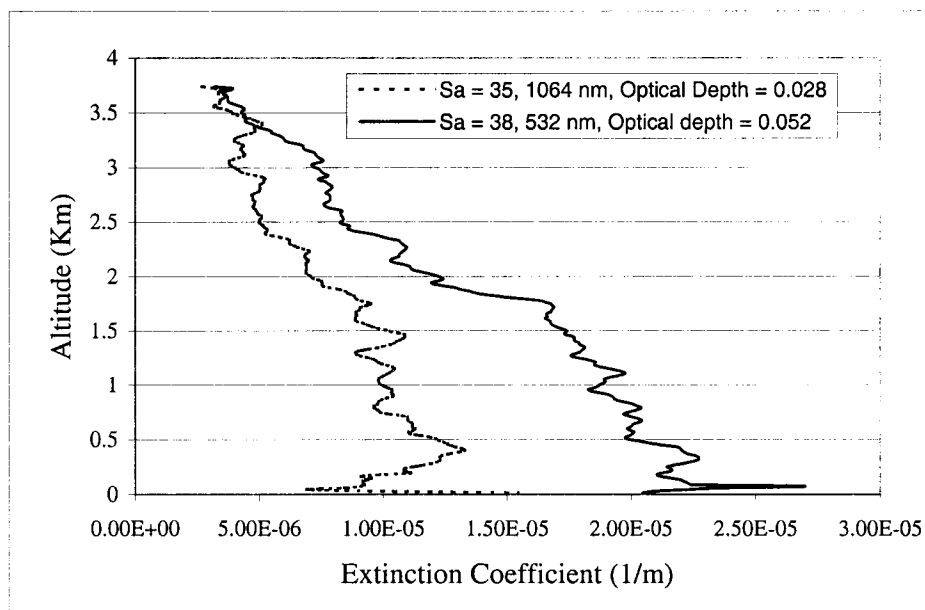


Fig. 5.5. Retrieved aerosol extinction profiles at 532 and 1064 nm for orbit 103.

nm are shown in Figs 5.6 and 5.7. In each figure the solar radiometer measured aerosol optical depths are also shown for comparison. As can be seen in the figures, the solar radiometer measurements and the LITE retrieved optical depths overlap very well within the  $S_a$  limits (e.g., the two  $S_a$  limits at 532 nm for LITE orbit 103 are 35 and 40). It reveals for this continental case that the  $S_a$  values at 532 nm are between 35 and 40, namely,  $S_{a,532} = 37.5 \pm 2.5$ . Similarly, the  $S_a$  values at 1064 nm can also be estimated as  $S_{a,1064} = 32.5 \pm 2.5$ . It should be noted that LITE measurements were made at night, while solar radiometer measurement were made during daytime. Hence, this time difference could mean that  $\tau_a$  changed somewhat over the time between when solar radiometer and LITE measurement were made.

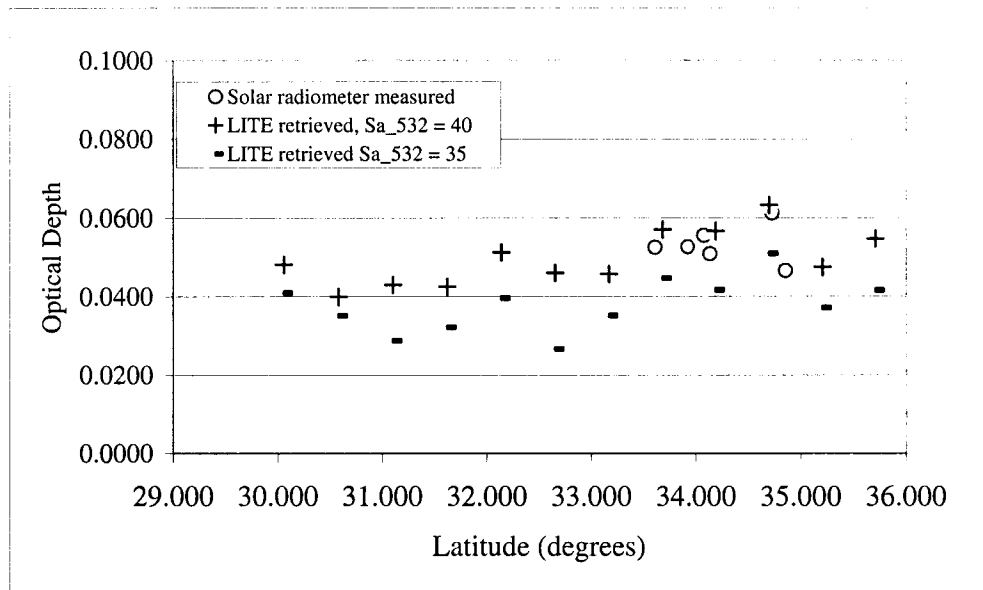


Fig. 5.6. Solar radiometer measured and LITE retrieved aerosol optical depths vs. latitudes.

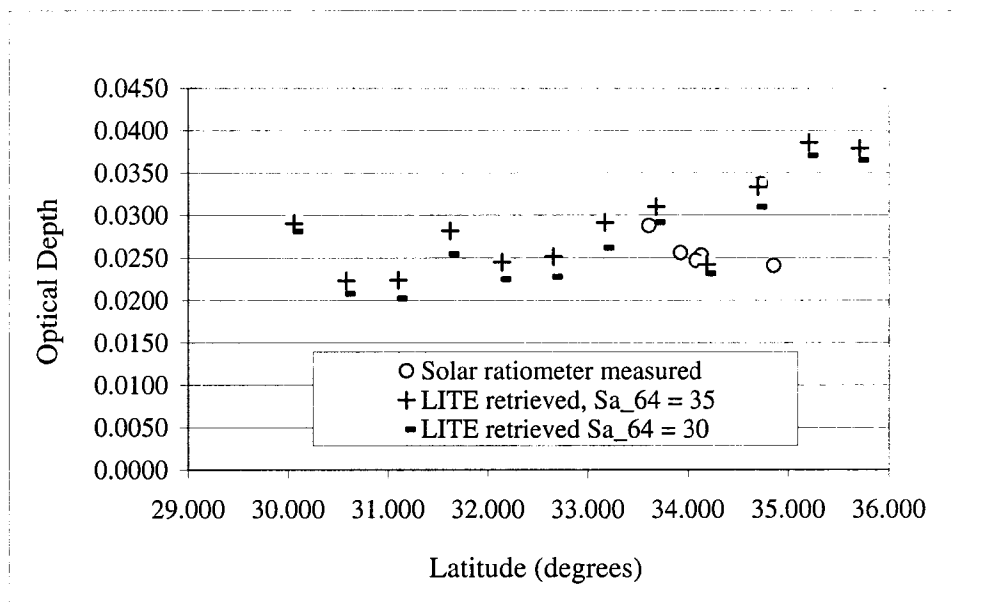


Fig. 5.7. Solar radiometer measured and LITE retrieved aerosol optical depths vs. latitudes.

The retrieved aerosol optical depths at 532 and 1064 nm for LITE orbit 24 are shown in Fig. 5.8 and Fig. 5.9. The  $S_a$  values used in the LITE retrieval for 532 nm are 24, 32 and 40, respectively. The  $S_a$  values for the 1064 nm LITE retrieval are 18, 26 and 34. The LITE retrieval results and the solar radiometer measurements are shown in Fig. 5.8 and Fig. 5.9. The range of overlap between the LITE retrievals and the solar radiometer measurements reveals that the  $S_a$  values at 532 nm for that portion of orbit 24 can be estimated fairly well as  $S_{a,532} = 32 \pm 8$ . Correspondingly, the  $S_a$  values at 1064 nm can be estimated as  $S_{a,1064} = 26 \pm 8$ . The solar radiometer measurements for orbit 24 were made the day before and the day after the LITE overpass. Again, the time difference could mean that  $\tau_a$  changed somewhat over the time.

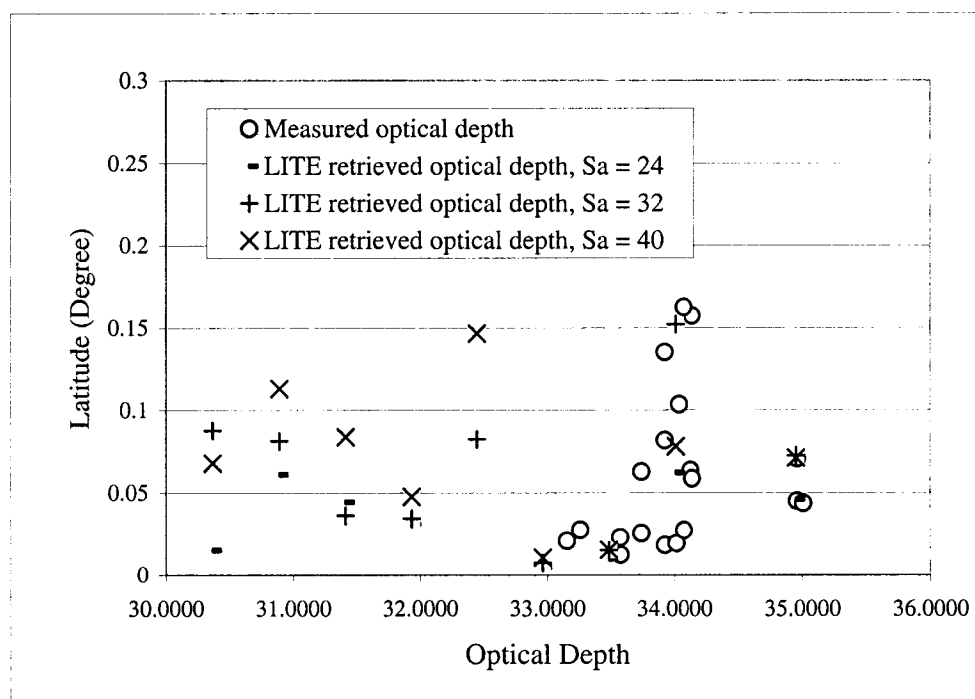


Fig. 5.8. Solar radiometer measured and LITE retrieved aerosol optical depths vs. latitudes.

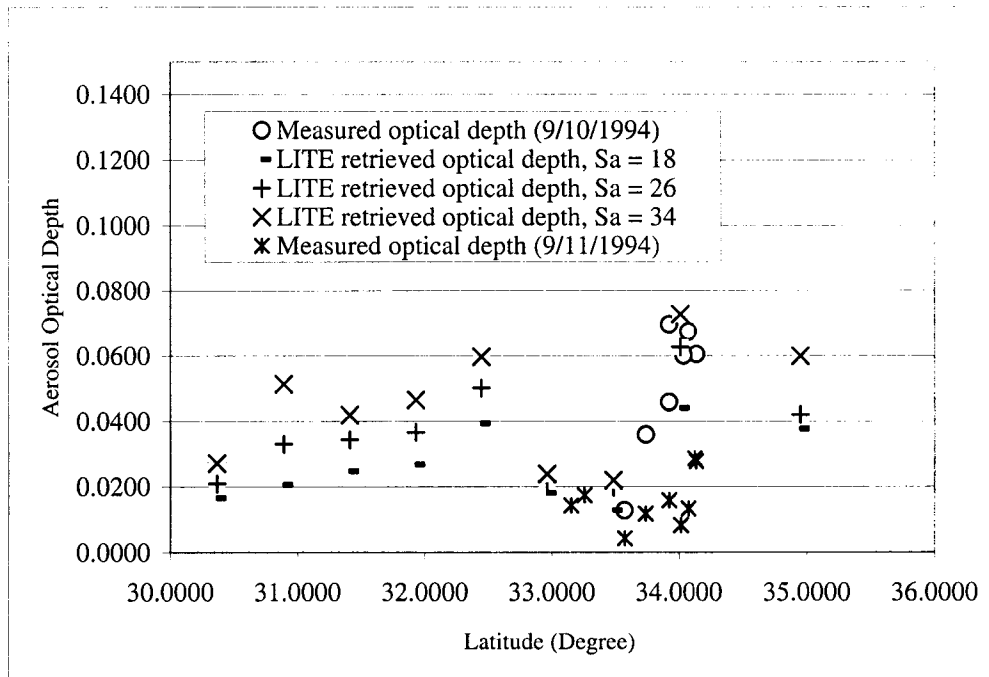


Fig. 5.9. Solar radiometer measured and LITE retrieved aerosol optical depths vs. latitudes.

### 5.3 Controlled Simulation for the Investigation of the $S_a$ and C Bias Error

The aerosol retrieval results in section 5.2.1 have shown that the  $S_a$  bias error for the actual LITE data is the most influential source among all the error sources that contribute to the total relative uncertainty of the retrieved aerosol backscattering coefficients. Section 5.2.2 further investigated the range of  $S_a$  for the continental case. In this section, some controlled simulations were applied to the simulated lidar signals to evaluate the impact of the  $S_a$  and C bias error on the retrieved aerosol backscattering coefficients and extinction coefficients.

Two typical aerosol types were selected for the investigation of the  $S_a$  and C bias errors with the simulated lidar signals at 532 nm. One of them is the elevated aerosol

layer type and the aerosol optical depth for the elevated aerosol layer is 0.5. The other one is the mixed boundary layer type and the aerosol optical depth for the boundary layer is 0.2. The assumed C bias error for both aerosol types is 4.4% and the assumed relative  $S_a$  bias errors for both aerosol types are  $\pm 15\%$  and  $\pm 30\%$ , respectively.

Fig. 5.10 shows the retrieved aerosol backscattering coefficients with the aerosol optical depth,  $\tau_a$ , as 0.5 and the relative  $S_a$  bias error as 15% and 30%, respectively, for parts (a) and (b). The simulation results for part (a) show that the relative uncertainty of the retrieved aerosol backscattering coefficients,  $\delta\beta_a(z)/\beta_a(z)$ , due to  $S_a$  bias error, is  $\sim 3\%$  near the top of the elevated aerosol layer and it increases to  $\sim 11\%$  in the middle of the layer. Near the layer bottom, the value of  $\delta\beta_a(z)/\beta_a(z)$  reaches  $\sim 21\%$  (at lower altitudes, it can be higher than 50%) and the averaged relative uncertainty of the retrieved aerosol backscattering coefficients through the whole aerosol layer is  $\sim 8\%$ . The

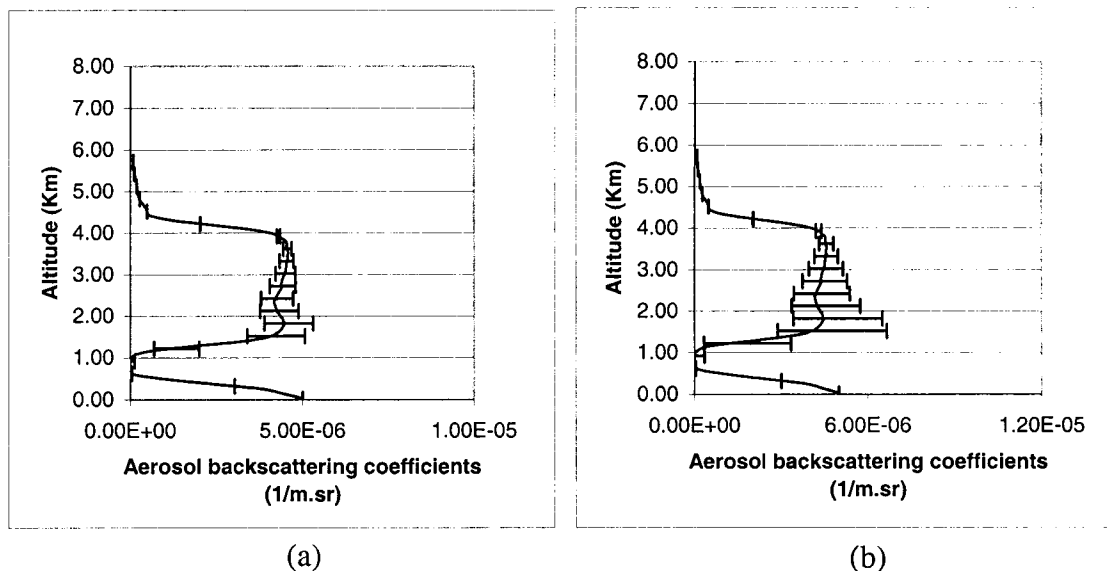


Fig. 5.10. Retrieved aerosol backscattering coefficients with  $\tau_a=0.5$ , relative  $S_a$  bias error as (a) 15% and (b) 30%.

simulation results for part (b) show the same pattern as part (a), which increases gradually from the layer top down to the layer bottom. But the values of  $\delta\beta_a(z)/\beta_a(z)$  are apparently larger than that for part (a). The value of  $\delta\beta_a(z)/\beta_a(z)$  is  $\sim 5\%$  near the top of the elevated aerosol layer and it increases to  $\sim 23\%$  in the mid-layer. The value of  $\delta\beta_a(z)/\beta_a(z)$  is  $\sim 46\%$  near the bottom of the layer (at lower altitudes, it can be up to 126%) and the averaged  $\delta\beta_a(z)/\beta_a(z)$  through the whole aerosol layer is  $\sim 18\%$ .

The retrieved aerosol extinction coefficients with  $\tau_a = 0.5$ , relative  $S_a$  bias error as 15% and 30% are shown in part (a) and (b) of Fig. 5.11, respectively. The relative uncertainty of the retrieved aerosol extinction coefficients,  $\delta\sigma_a(z)/\sigma_a(z)$ , is larger than that of the retrieved aerosol backscattering coefficients due to the multiple factor,  $S_a$ . In part (a), the simulation results show that  $\delta\sigma_a(z)/\sigma_a(z)$  is  $\sim 17\%$  near the top of the elevated aerosol

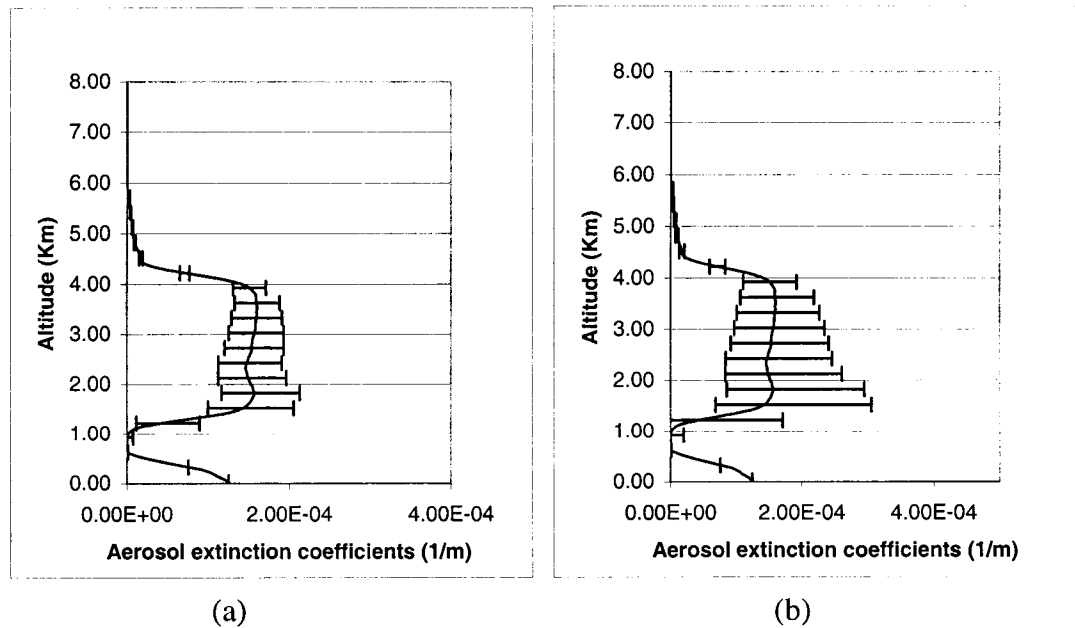


Fig. 5.11. Retrieved aerosol extinction coefficients with  $\tau_a=0.5$ , relative  $S_a$  bias error as (a) 15% and (b) 30%.

layer and near the bottom of the aerosol layer,  $\delta\sigma_a(z)/\sigma_a(z)$  reaches  $\sim 37\%$  (at lower altitudes, it can be  $\sim 90\%$ ). The averaged  $\delta\sigma_a(z)/\sigma_a(z)$  through the whole aerosol layer is  $\sim 23.2\%$ . In part (b) of Fig. 5.11, the relative uncertainty of the retrieved aerosol extinction coefficients is larger than those in part (a) through whole aerosol layer and the averaged  $\delta\sigma_a(z)/\sigma_a(z)$  is  $\sim 50\%$ .

With C bias error as 4.4%, the retrieved aerosol backscattering and extinction coefficients with  $\tau_a = 0.5$  are shown in part (a) and (b) of Fig. 5.12, respectively. It is noticed that the relative uncertainties of the retrieved aerosol backscattering coefficients in part (a) and aerosol extinction coefficients in part (b) are almost the same at each evaluated altitude. This is because when doing the simulation, the relative uncertainties due to the C bias error was evaluated independently from other error sources (i.e., without considering  $S_a$  bias error). It is observed in Fig. 5.12 that the relative uncertainty of the aerosol backscattering/extinction coefficients due to the C bias error also increases

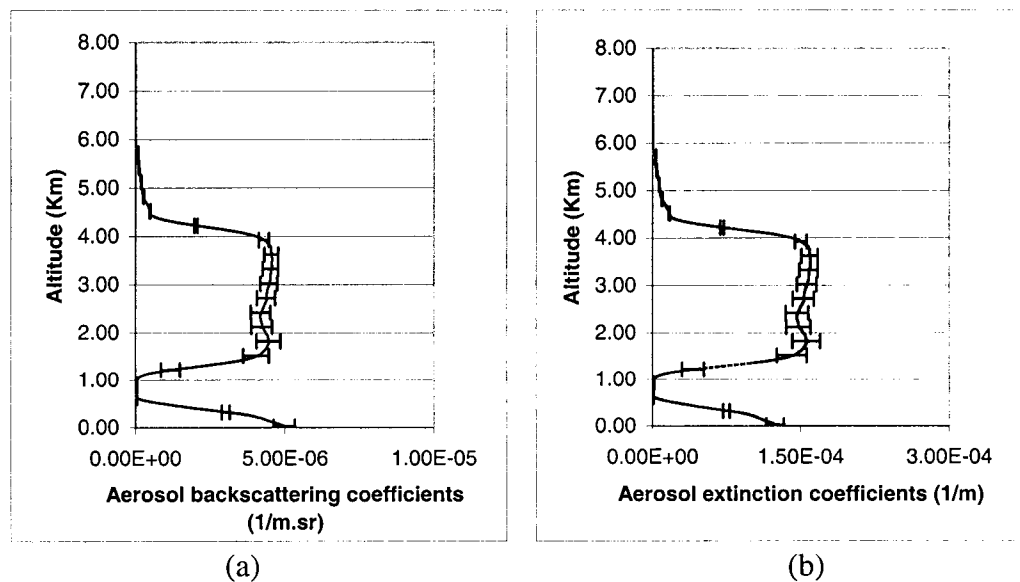


Fig. 5.12. Aerosol retrieval results with  $\tau_a=0.5$ , relative C bias error as 4.4%.

from the top through the bottom of the elevated aerosol layer. However, the change is relatively smooth compared with the changes in Figs. 5.10 and 5.11. The simulation results show that  $\delta\beta_a(z)/\beta_a(z)$  or  $\delta\sigma_a(z)/\sigma_a(z)$  is  $\sim 5\%$  near the top of the elevated aerosol layer and it increases to  $\sim 8\%$  in the middle of the layer. Near the bottom of the aerosol layer,  $\delta\beta_a(z)/\beta_a(z)$  or  $\delta\sigma_a(z)/\sigma_a(z)$  reaches  $\sim 11\%$  (at lower altitudes, it can be as large as  $\sim 26\%$ ). The averaged  $\delta\beta_a(z)/\beta_a(z)$  or  $\delta\sigma_a(z)/\sigma_a(z)$  through the whole aerosol layer is  $\sim 7\%$ .

Similarly, the impact of the  $S_a$  and C bias errors on the aerosol retrieval for the boundary aerosol layer type was investigated by running the simulations. Fig. 5.13 shows that the retrieved aerosol backscattering coefficients with  $\tau_a = 0.2$  and the relative  $S_a$  bias error as 15% and 30% for parts (a) and (b), respectively. The simulation results show that the relative uncertainty of the aerosol backscattering/extinction coefficients in part (a) or part (b) is smaller than that for the elevated aerosol layer type. In part (a) of Fig. 5.13, the averaged  $\delta\beta_a(z)/\beta_a(z)$  through the whole aerosol layer is  $\sim 3\%$ . Compared to part (a), the value of  $\delta\beta_a(z)/\beta_a(z)$  for part (b) is larger and the averaged  $\delta\beta_a(z)/\beta_a(z)$  is  $\sim 5\%$ .

In Fig. 5.14, the averaged  $\delta\sigma_a(z)/\sigma_a(z)$  is  $\sim 18\%$  for part (a) and  $\sim 35\%$  for part (b). By applying a relative C bias error of 4.4% to the simulations for the boundary aerosol layer type, the aerosol retrieval results with  $\tau_a = 0.2$  are shown in Fig. 5.15. As it was shown earlier, the change of  $\delta\beta_a(z)/\beta_a(z)$  or  $\delta\sigma_a(z)/\sigma_a(z)$ , due to the relative C bias error, is fairly smooth within the aerosol layer. The simulation results in Fig. 5.15 show that  $\delta\beta_a(z)/\beta_a(z)$  or  $\delta\sigma_a(z)/\sigma_a(z)$  is  $\sim 5\%$  near the top of the elevated aerosol layer and  $\sim 6\%$  in the middle of the layer. The  $\delta\beta_a(z)/\beta_a(z)$  or  $\delta\sigma_a(z)/\sigma_a(z)$  reaches  $\sim 7\%$  near the bottom of

the aerosol layer and the averaged  $\delta\beta_a(z)/\beta_a(z)$  or  $\delta\sigma_a(z)/\sigma_a(z)$  for both parts in Fig. 5.15 is  $\sim 5\%$ .

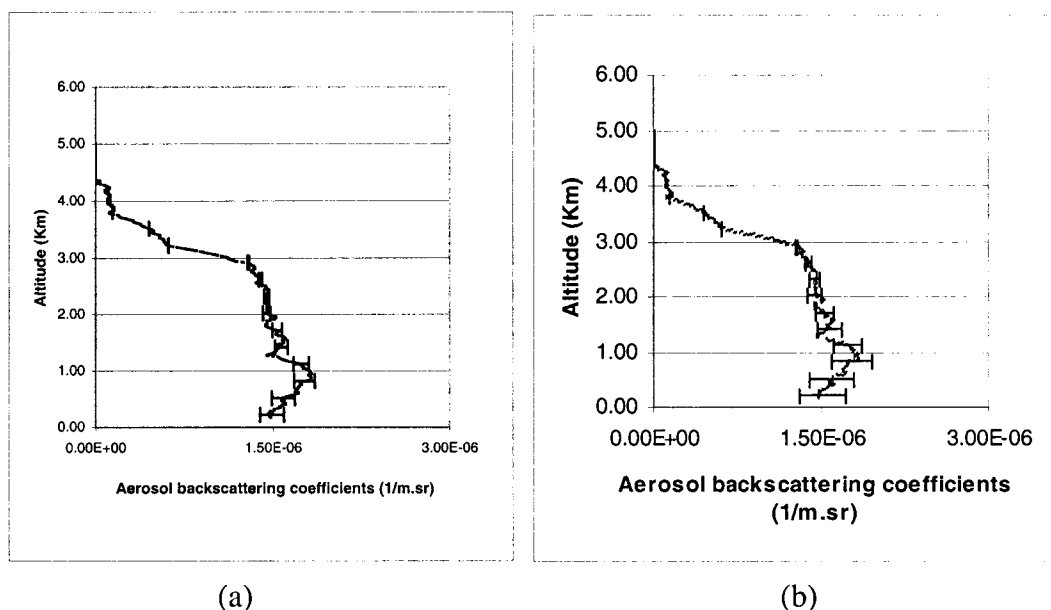


Fig. 5.13. Retrieved aerosol backscattering coefficients with  $\tau_a=0.2$ , relative  $S_a$  bias error as (a) 15% and (b) 30%.

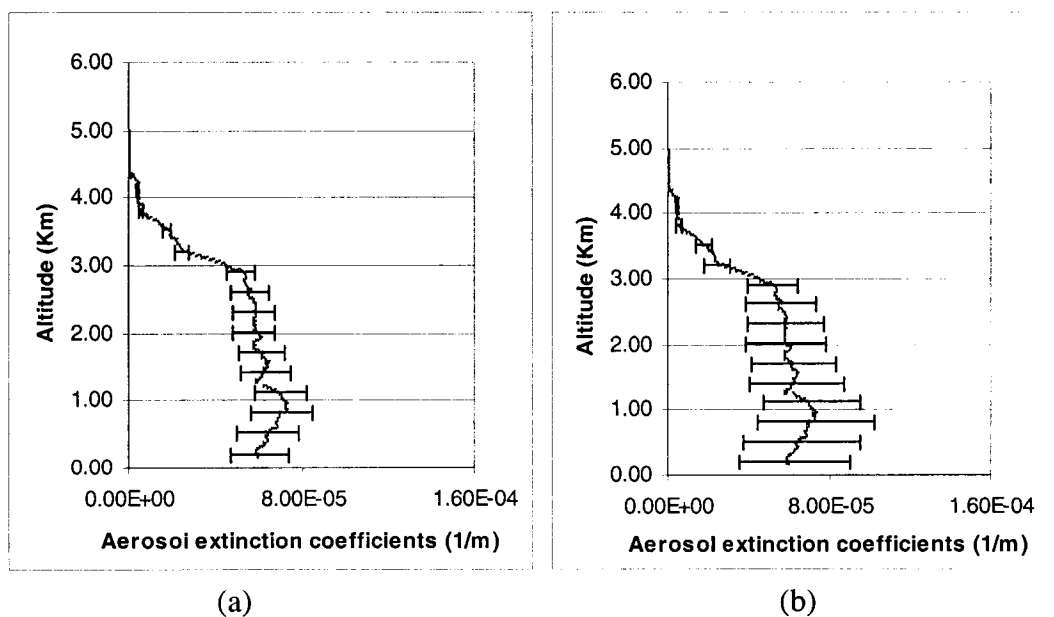


Fig. 5.14. Retrieved aerosol extinction coefficients with  $\tau_a=0.2$ , relative  $S_a$  bias error as (a) 15% and (b) 30%.

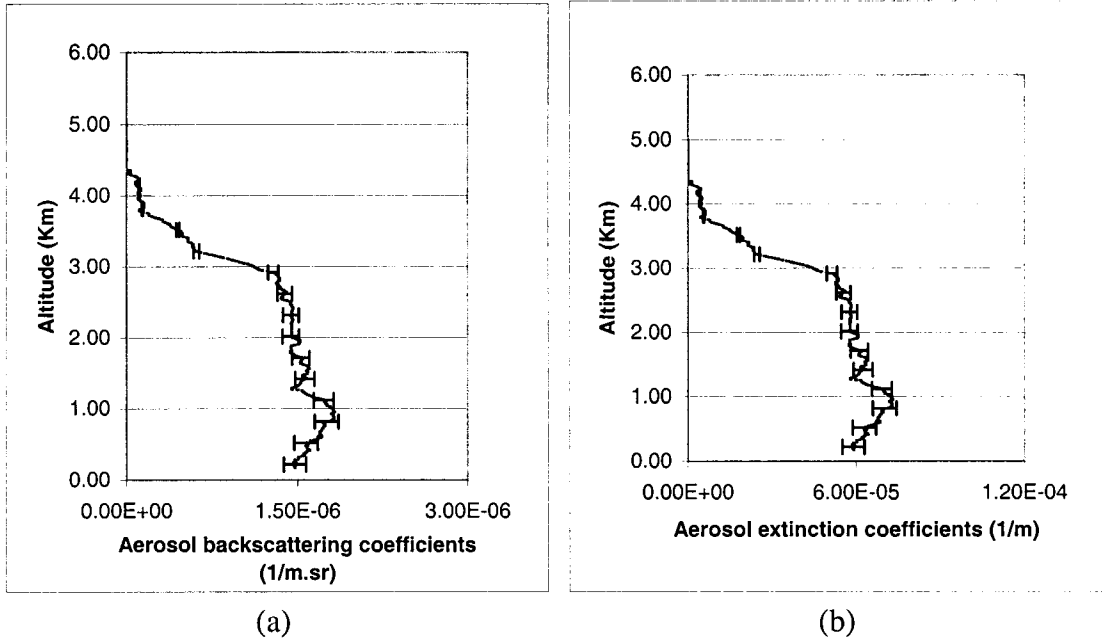


Fig. 5.15. Aerosol retrieval results with  $\tau_a=0.2$ , relative C bias error as 4.4%.

In summary, the LITE aerosol retrieval and the controlled simulation results for both aerosol types show that within the aerosol layer the relative uncertainty,  $\delta\sigma_a(z)/\sigma_a(z)$ , is larger than  $\delta\beta_a(z)/\beta_a(z)$  due to either  $S_a$  bias error or C bias error. Comparatively, the relative uncertainty,  $\delta\sigma_a(z)/\sigma_a(z)$  or  $\delta\beta_a(z)/\beta_a(z)$ , for the elevated aerosol layer type is larger than that for the boundary aerosol layer type. When the assumed relative  $S_a$  bias error changes from 15% to 30%,  $\delta\sigma_a(z)/\sigma_a(z)$  and  $\delta\beta_a(z)/\beta_a(z)$  for the elevated aerosol layer type and  $\delta\sigma_a(z)/\sigma_a(z)$  for the boundary aerosol layer type, become significantly larger. For both aerosol model types (elevated aerosol layer type and boundary aerosol layer type), the uncertainty of the aerosol backscattering/extinction coefficients, which is due to the C bias error, does not vary much through most of the aerosol layer. The value of  $\delta\sigma_a(z)/\sigma_a(z)$  or  $\delta\beta_a(z)/\beta_a(z)$  with the C bias error obtained for the two aerosol types is not more than 10%. In the following chapter, aerosol retrievals

based on more accurate  $S_a$  constraint will be introduced and more aerosol models will be studied based on a two-wavelength lidar constrained ratio aerosol model-fit (CRAM) retrieval approach.

## 6. SPACEBORNE LIDAR AEROSOL RETRIEVAL APPROACHES BASED ON AEROSOL MODEL CONSTRAINTS

Aerosol retrievals at 532 nm for the current GLAS and upcoming CALIPSO satellite lidar missions employ/will employ a look-up table approach to select climatologically based  $S_a$  model values for these retrievals when alternate, less uncertain methods for either defining  $S_a$  or providing the needed auxiliary information are unavailable. Reagan et al. [90] addressed a revised table look-up approach that incorporated two notable revisions for improved  $S_a$  selection, which, as a consequence, enable more bounded aerosol retrievals. One is a refined, more bounded set of  $S_a$  values, both for 532 nm and 1064 nm, representative of a definitive set of aerosol types/models determined from an extensive analysis of the AERONET data base [56]. The other is an accompanying set of key spectral ratio parameters (i.e., dual wavelength, 532 nm to 1064 nm, ratios of backscatter, extinction and  $S_a$ ) also derived from the AERONET data which offer additional ways to bound the lidar aerosol retrievals. Thus, aerosol retrievals can be obtained subject to the constraints that the lidar data yield retrievals with spectral ratio parameters consistent with a given aerosol model (or models), to confirm the model choice and better bound the retrievals. This chapter presents the results of simulations made by assuming different models in support of the two-wavelength lidar Constrained Ratio Aerosol Model-fit (CRAM) retrieval approach [90].

## 6.1 A Revised Table-Look up Approach for $S_a$ Selection

AERONET is a network of globally distributed sun and sky radiometers that has been in operation for over a decade, for the purpose of improving our knowledge of global aerosol optical properties. These radiometers measure the atmospheric transmittance and spectral sky radiance over a wide angular range from the sun at four wavelengths (440, 670, 865 and 1020 nm), providing sufficient information to determine aerosol optical and microphysical properties [91]. From a statistical point of view, Cattrall et al. [56] selected 26 sites from the over one hundred AERONET locations to compute the aerosol extinction-to-backscatter ratio (also called lidar ratio)  $S_a$  at 0.55 and 1.02  $\mu\text{m}$ , and the spectral backscatter and extinction ratios of the aerosols observed at these sites. For those selected locations, one aerosol type typically dominated the atmospheric column for a significant portion, if not most of the year. For example, during the biomass burning seasons in South America and Africa, one obtains results defining a Biomass Burning model; urban/industrial summer emissions into the boundary layer over cities characterize an Urban/Industrial model; and sites influenced by mineral dust during the summer months (when the desert is most arid and the diurnal heating strongest for dust production) yield results characterizing a Dust model. With the cloud-screened, quality assured AERONET retrievals of aerosol single-scattering albedo, scattering phase function, refractive index, and size distributions for the entire history of each selected site, Cattrall et al. [56] were able to obtain a well defined and bounded set of  $S_a$  values, and accompanying spectral backscattering and extinction ratios, for the relatively few aerosol models/types that predominantly characterize aerosols observed around the

world. The aerosol types thus obtained yielded parameters that also agreed very well with available measured values reported in the literature.

The results obtained from this AERONET study are shown in Table 6.1. The lidar ratio column lists the mean  $S_a$  and standard deviation at 550 nm for each aerosol type, while the remaining columns list the ratios for the parameter values at 550 nm divided by the corresponding values at 1020 nm. These wavelengths were chosen more from AERONET interest, but they are close enough to be assumed to apply with negligible error to the lidar wavelengths of 532 nm and 1064 nm. The aerosol types and  $S_a$  determinations given in Table 6.1 represent a significant, more quantitatively based extension of the modeling results first reported by Reagan et al. [92]. From Table 6.1, it is noted that Biomass Burning, Developing Nations, and Urban/Industrial are all fairly similar in  $S_a$ . So one  $S_a$  with somewhat larger SD would work for all of those models, such as  $S_a \approx 65 \pm 15$ . In Table 6.1, the SD's on  $S_a$  for all models are all less than 20%, which are certainly better than the estimates of  $S_a$  in Chapter 5. (e.g.,  $S_a \approx 35 \pm 10$ , ~30% SD). The tighter bounds (smaller SD's) on the  $S_a$  values insure less uncertain aerosol retrievals subject to assuming a given aerosol type applies, and the additional ratio information in Table 6.1 also provides a means for further bounding/reducing uncertainties in the retrievals. It should be noted that the Dust (spheroids) model, which includes modeling non-spherical particle shape effects, is taken as the realistic model that should be assumed for dust. The Dust (sphere) model is included mainly to demonstrate the significant difference caused by non-spherical particles. The geographic location of selected aerosol sites is shown in Fig. 6.1.

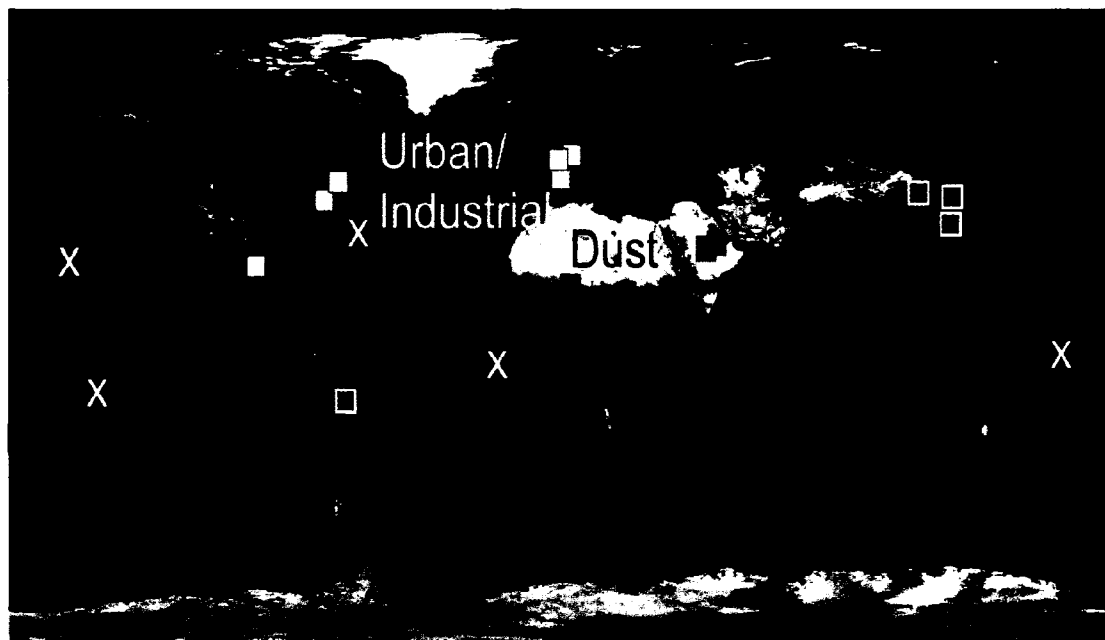


Fig. 6.1. Map of the AERONET sites used by Catrall et al. in their study. Oceanic sites are represented by an 'X' [56].

Table 6.1 Summary of lidar parameters retrieved from selected AERONET sites [56].

Aerosol type	550 nm Values		550 to 1020 nm Ratios		
	Reported in Literature	Lidar ratio (SD)*	S <sub>a</sub> ratio	β ratio	σ ratio
Biomass Burning	64(5)	60 (8)	2.1 (0.3)	1.8 (0.3)	3.8 (0.4)
Developing Nations	n/a	58 (11)	1.4 (0.2)	1.5 (0.2)	2.3 (0.3)
Urban/Industrial	64(4)	71 (10)	1.9 (0.3)	1.6 (0.2)	3.3 (0.5)
Oceanic	29(5)	28 (5)	1.0 (0.2)	1.4 (0.1)	1.5 (0.4)
Dust(spheres)	n/a	15 (2)	1.6 (0.2)	0.7 (0.1)	1.2 (0.1)
Dust(spheroids)	43(6)	42 (4)	1.2 (0.1)	0.9 (0.1)	1.2 (0.1)

\*SD = Standard deviation of Gaussian fit

## 6.2 Lidar Aerosol Retrieval Based on Modeled Constraints

The modeling and retrieval simulations in this chapter were applied to Biomass Burning, Urban/Industrial, Oceanic, Dust (spheroids) and Dust (sphere) models based on Table 6.1. With the available LITE database, the initial input for the simulations is the modeled aerosol backscattering coefficient profile that is based on LITE orbits 83, 103 and 146, respectively. Two LITE color images of the 532 nm calibrated backscatter profiles for orbits 83 and 146 are shown in Fig. 6.2 and Fig. 6.3, which exhibit strong backscatter signatures in the elevated dust and smoke layer region. These two figures are composed of individual lidar profiles along the Space Shuttle orbit tracks during nighttime conditions. Latitude and longitude are denoted along the abscissa. The intensities of the returned signal are measured in digitizer counts and correspond to the accompanying color scale which extends from black for the weakest signal through white for the strongest signal. Some strong return signals (e.g., the return signals from some clouds or the ground) will cause the lidar detector to saturate (digital counts equal to 4095). For orbit 83, a location, centered at  $\sim 26.8^\circ$  N,  $\sim 14.9^\circ$  W, was picked to do the simulation for the Dust (spheres) and Dust (spheroids) cases while a location, centered at  $24.3^\circ$  N and  $27.3^\circ$  W, was picked from orbit 146 for the Biomass Burning case.

Such elevated layers provide the opportunity for self-transmittance lidar retrievals (i.e., layer transmittance can be estimated by lidar signal difference above and below layer) wherein  $S_a$  can be retrieved using the layer transmittance as a boundary condition. This would provide an independent estimate of  $S_a$  to compare with the model values in Table 6.1. However, as the LITE signals are affected by multiple scattering, which

reduces the layer attenuation, a multiple scattering correction would be required [93] to obtain a true estimate of  $S_a$  for comparison with Table 6.1.

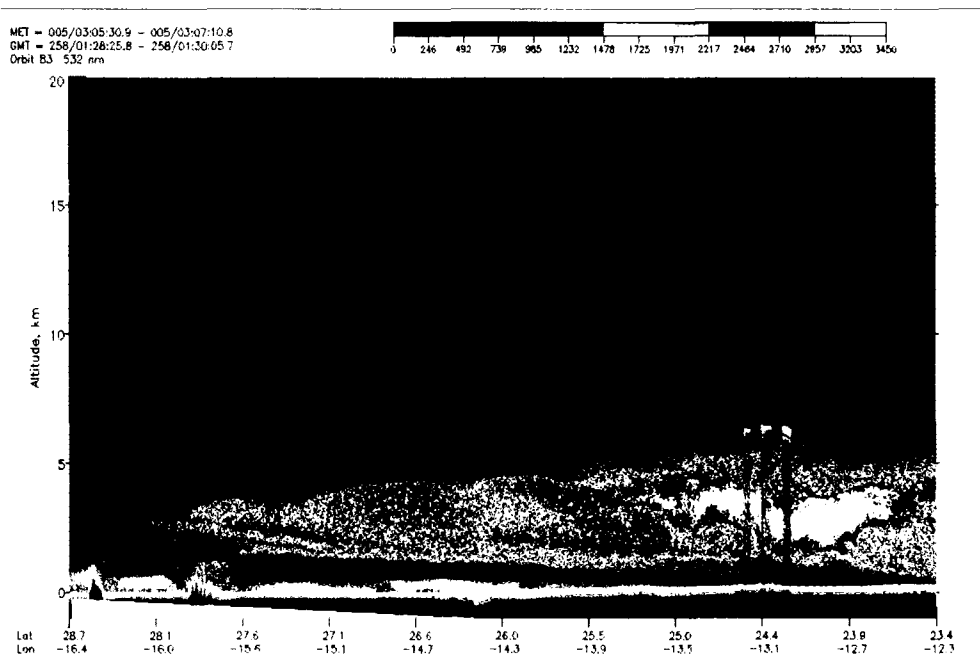


Fig. 6.2. Colored image of the Saharan dust layer from LITE orbit 83.

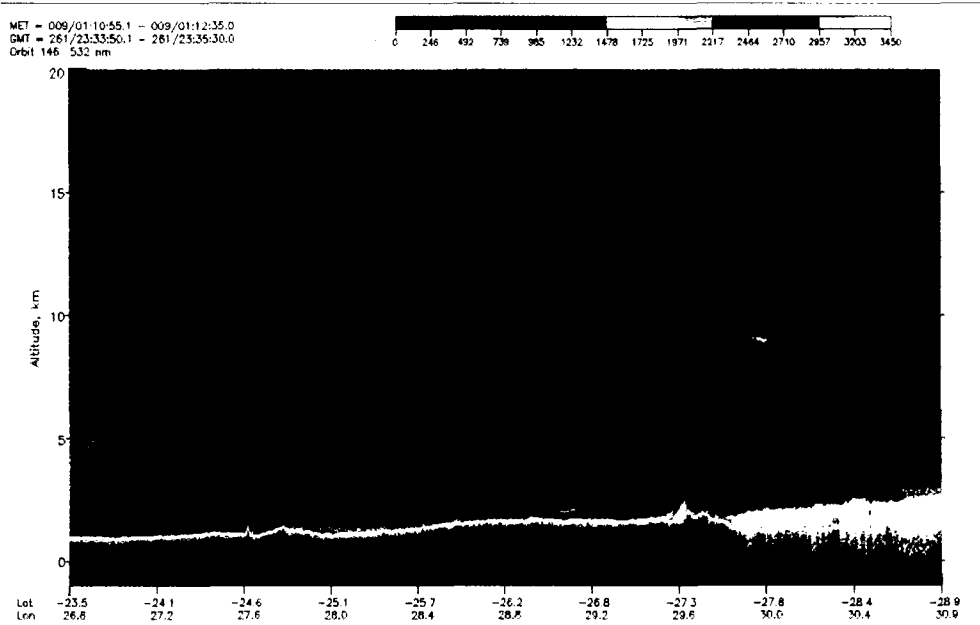


Fig. 6.3. Colored image of the smoke layer for biomass burning from LITE orbit 146.

As such, as a first cut approach, the uncorrected LITE aerosol backscatter retrievals are used as model profiles along with assumed model  $S_a$  values from Table 6.1 to define simulated lidar signals that are used in retrievals to test the agreement/consistency obtained assuming various aerosol models. Similarly, a location from LITE orbit 103 ( $\sim 33.73^\circ\text{N}$ ,  $\sim 115^\circ\text{W}$ ) was selected to get the aerosol backscattering coefficient profile for the Urban/Industrial model, while a location from LITE orbit 83 ( $\sim 29.45^\circ\text{N}$ ,  $\sim 17.1^\circ\text{W}$ ) was selected to get the aerosol backscattering coefficient profile for the Oceanic model. Two LITE color images of the 532 nm calibrated backscatter profiles for a segment of orbits 83 and 103 are shown in Figs. 6.4 and 6.5, respectively.

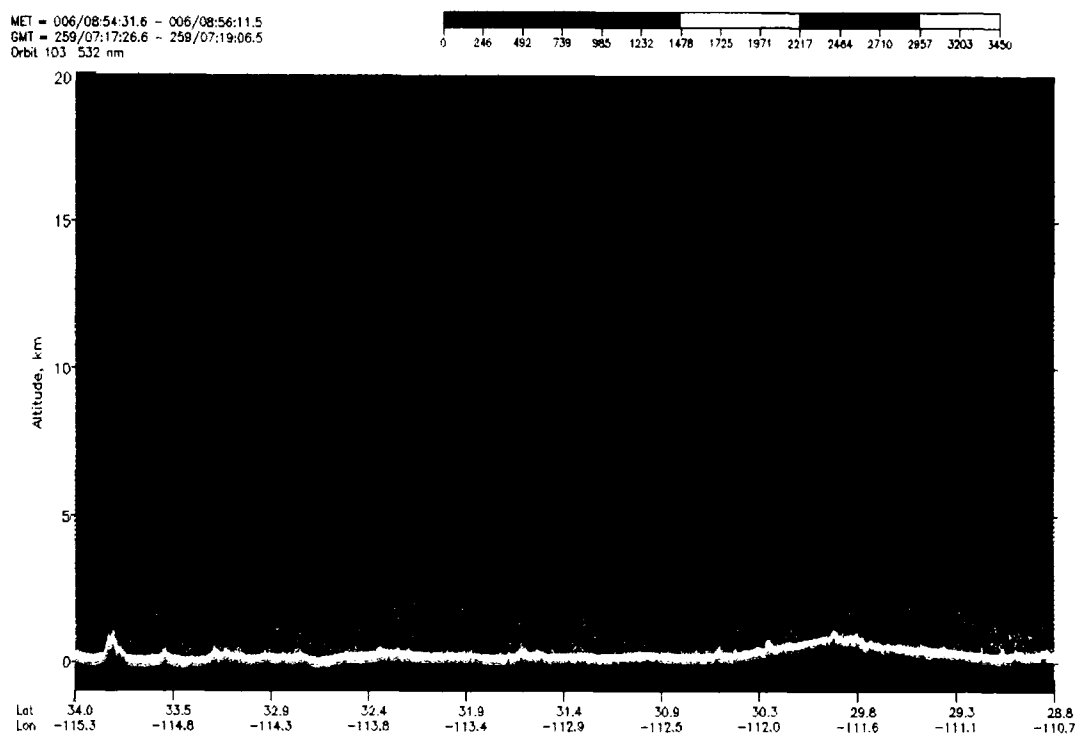


Fig. 6.4. Colored image of the boundary layer for urban/industrial from LITE orbit 103.

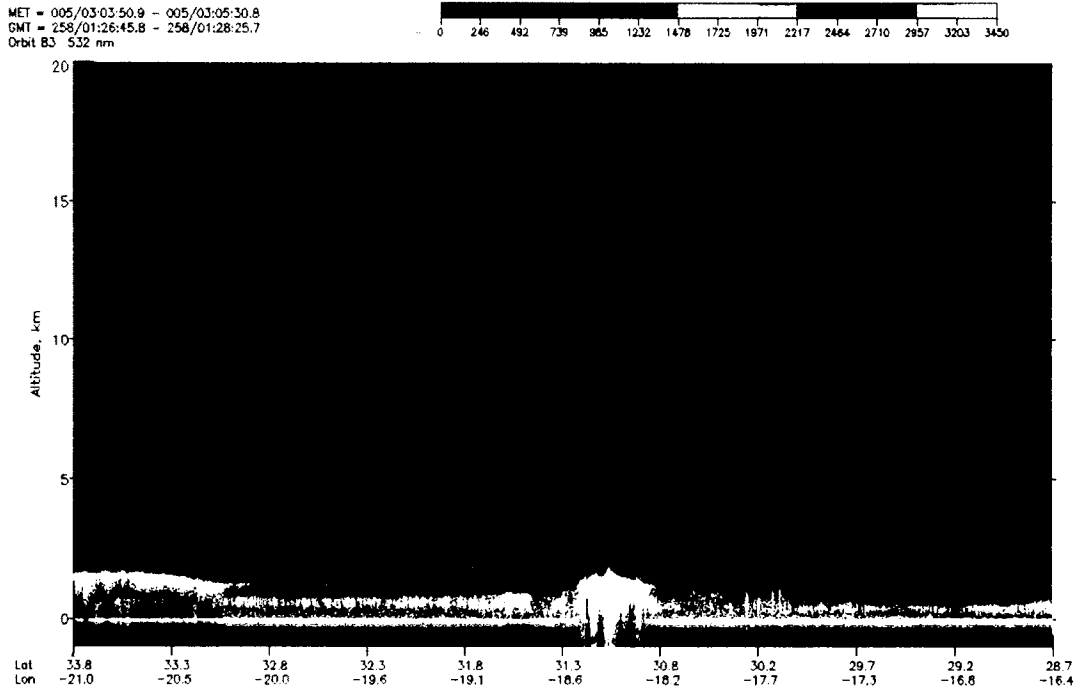


Fig. 6.5. Colored image of the marine boundary layer (MBL) from LITE orbit 83.

To define a signal for a given aerosol model, a value of  $S_{a,532}$  is selected from Table 6.1 for that model, and the corresponding 532 nm lidar signal is obtained by rewriting (2.7) as

$$X_{a,532}(r) = C_{532} \left[ \beta_{a,532}^M(r) + \beta_{R,532}(r) \right] \exp \left[ -2 \int_0^r \left[ S_{a,532} \beta_{a,532}^M(r') + S_R \beta_{R,532}(r') \right] dr' \right] \quad (6.1)$$

where  $\beta_{a,532}^M(r)$  is a modeled aerosol backscattering profile representing a selected structural feature (e.g., an elevated layer as often occurs with transported Saharan dust and horizontally advected biomass burning smoke plumes).

Similarly, the 1064 nm signal can also be derived from (2.7), by the relation

$$X_{a,64}(r) = C_{64} \left[ \beta_{a,64}^M(r) + \beta_{R,64}(r) \right] \exp \left[ -2 \int_0^r \left[ S_{a,64} \beta_{a,64}^M(r') + S_R \beta_{R,64}(r') \right] dr' \right] \quad (6.2)$$

where  $\beta_{a,64}^M(r)$  is determined from  $\beta_{a,532}^M(r)$  using the  $\beta$  ratio  $(\frac{\beta_{a,532}(r)}{\beta_{a,64}(r)})$  from Table 6.1 and  $S_{a,64}$  is also selected from Table 6.1 for the model in question. With the modeled aerosol signals for 532 and 1064 nm,  $\beta_a(r)$  and  $\sigma_a(r)$  at 532 and 1064 nm are obtained for each model set of assumed  $S_a$  values using a modeled/specified  $S_a$  approach for the retrieval relations for 532 nm and 1064 nm (e.g., Eqs.(2.27) and (2.38)). The resulting two-wavelength ratios of  $\beta_a(r)$  and  $\sigma_a(r)$  were then compared to the expected ratios for the assumed model type to determine if the retrievals were in agreement/consistency with the model assumption. Three model  $S_a$  values,  $S_{a,\text{mean}}$  and  $S_{a,\text{mean}} \pm \text{SD}$ , were assumed for each model type.

The agreement/consistency between the retrievals and the model assumption is also cross-examined by applying the  $S_a$  values ( $S_{a,532}$  and  $S_{a,64}$ ) of one model to the signals ( $X_{a,532}$  and  $X_{a,64}$ ) of another model. For example, the  $S_a$  values for Dust (spheroids) have been applied to the modeled Biomass Burning signals for doing the aerosol retrievals and, likewise, the  $S_a$  values for Biomass Burning model have also been applied to the Dust (spheroids) signals to check the agreement between the modeled assumption and the retrievals.

### 6.3 Performance Function, Q

A performance function, Q, was formulated to assess the agreement in a least squares sense between the ratios of  $\frac{\beta_{a,532}(r)}{\beta_{a,64}(r)}$  and  $\frac{\sigma_{a,532}(r)}{\sigma_{a,64}(r)}$  for a given aerosol model and

the corresponding ratios computed from the simulated  $X(r)$  signals, at 532 and 1064 nm, for different assumed  $S_a$  values:

$$Q = W_\beta \left( \frac{R_\beta^c - R_\beta^m}{R_\beta^m} \right)^2 + W_\sigma \left( \frac{R_\sigma^c - R_\sigma^m}{R_\sigma^m} \right)^2 + W_s \left( \frac{R_s^c - R_s^m}{R_s^m} \right)^2 \quad (6.3)$$

where  $R_\beta = \frac{\beta_{a,532}}{\beta_{a,1064}}$ ,  $R_\sigma = \frac{\sigma_{a,532}}{\sigma_{a,1064}}$  and  $R_s = \frac{S_{a,532}}{S_{a,1064}}$ . Also,  $W_\beta$ ,  $W_\sigma$  and  $W_s$  are

weighting constants, generally set to unity, although the  $R_s$  term cannot be used unless some auxiliary estimate of  $R_s^m$  is available (e.g., from independent determination of the Angstrom exponent,  $\alpha$ , which can provide a model fit to  $R_s^m$ ). It was set to zero for the simulation studies presented here. If the model assumption yields minimum  $Q$ , it means that the model assumption is the best estimated solution. However, multiple model solutions may be possible and acceptable if the  $Q$ 's for different models fall within the uncertainty range associated with the model spread in  $S_a$  (i.e.,  $S_{a,\text{mean}} \pm \text{SD}$ ).

## 6.4 Results and Discussions

The averaged aerosol backscatter and extinction ratios retrieved for four aerosol models (Dust (spheroids), Biomass Burning, Oceanic and Urban/Industrial cases), obtained by averaging the retrieved profiles over the whole aerosol layer, are shown in the Figs. 6.6 - 6.9. In Figs 6.6 and 6.7 there are nine groups of simulation results, which correspond to three aerosol models. For each aerosol model, there are three groups of simulation results, which were obtained by applying the  $S_a$  values and  $S_a$  ratio of one model (i.e., 532 nm  $S_a = 42 \pm 4$  and  $S_a$  ratio of 1.2 for Dust (spheroids); 532 nm  $S_a = 60 \pm$

8 and  $S_a$  ratio of 2.1 for Biomass Burning; 532 nm  $S_a = 71 \pm 10$  and  $S_a$  ratio of 1.9 for Urban/Industrial) to the three simulated model signals (i.e., Dust (spheroids), Biomass Burning and Urban/Industrial). Similarly, Figs. 6.8 and 6.9 show the averaged backscatter

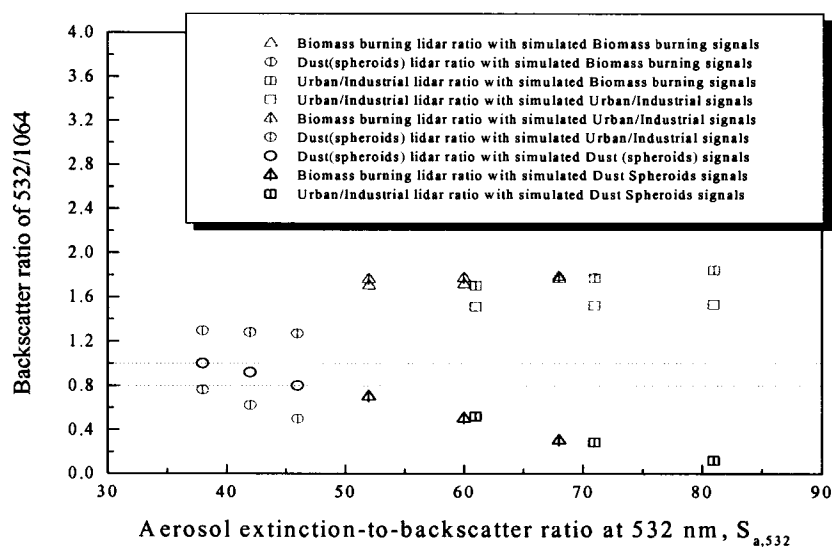


Fig. 6.6. Retrieved aerosol backscattering coefficient ratios of 532/1064 nm for Dust (spheroids), Biomass Burning and Urban/Industrial models.

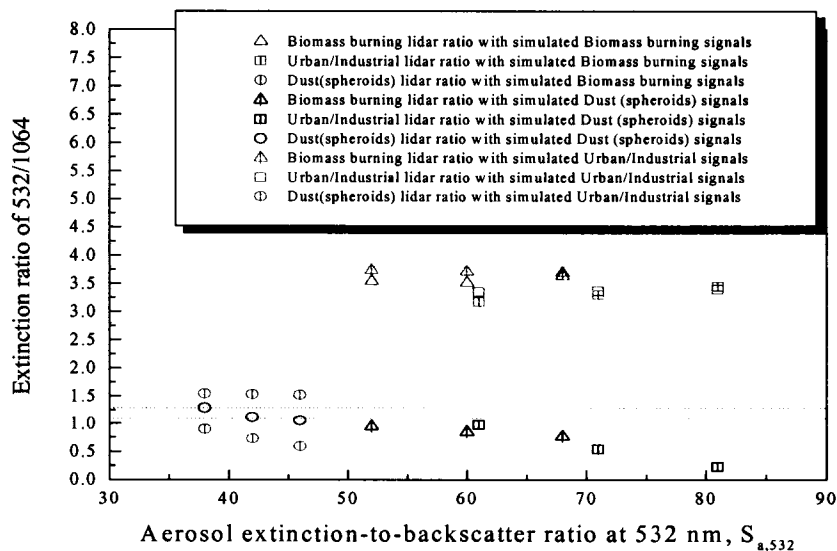


Fig. 6.7. Retrieved aerosol extinction coefficient ratios of 532/1064 nm for Dust (spheroids), Biomass Burning and Urban/Industrial models.

and extinction ratios retrieved for the Dust (spheroids), Urban/Industrial and Oceanic models assuming the Dust (spheroids) or Urban/Industrial or Oceanic model  $S_a$  and  $S_a$  ratio (e.g., 532 nm  $S_a = 28 \pm 5$  and  $S_a$  ratio of 1.0 for Oceanic model).

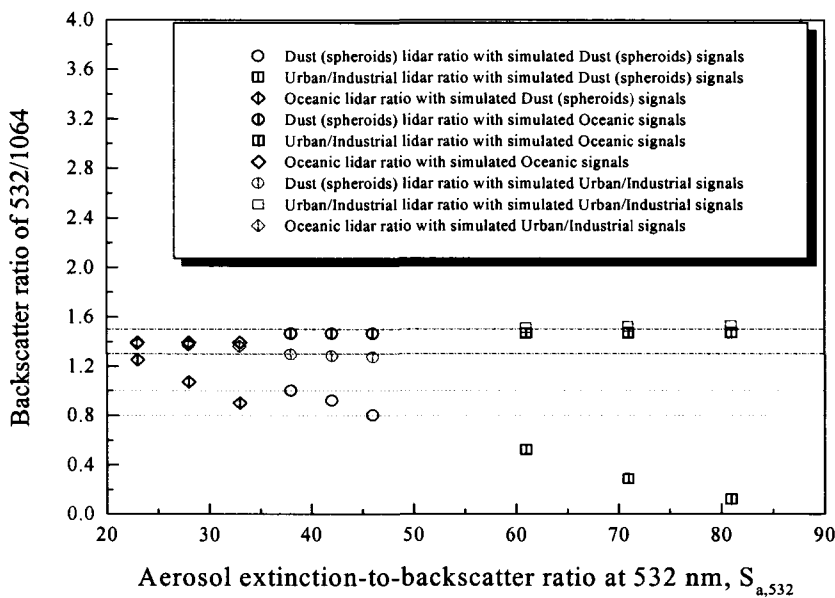


Fig. 6.8. Retrieved aerosol backscattering coefficient ratios of 532/1064 nm for Dust (spheroids), Oceanic and Urban/Industrial models.

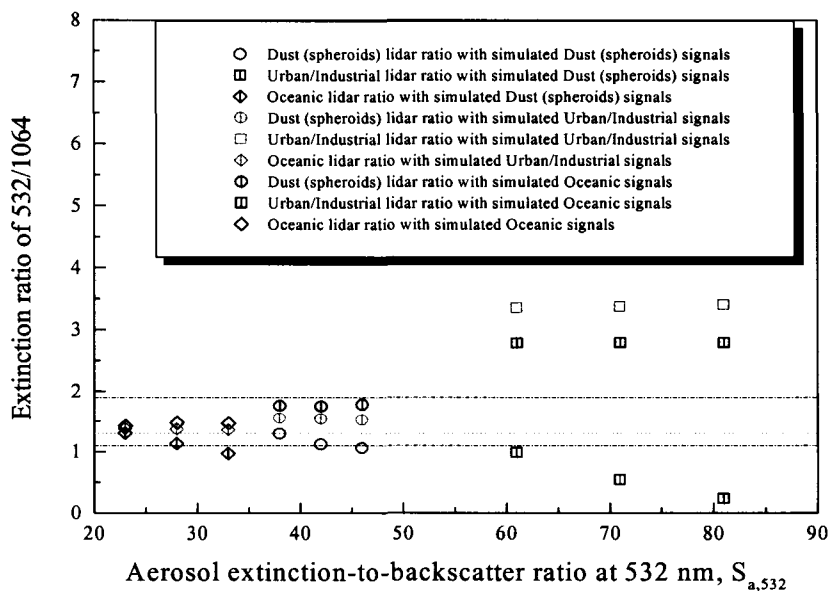


Fig. 6.9. Retrieved aerosol extinction coefficient ratios of 532/1064 nm for Dust (spheroids), Oceanic and Urban/Industrial models.

In Figs 6.6 – 6.9, the retrieved and model ratios for  $\frac{\beta_{a,532}(r)}{\beta_{a,64}(r)}$  and  $\frac{\sigma_{a,532}(r)}{\sigma_{a,64}(r)}$  are shown concurrently in these figures, where the mean model ratio ( $\frac{\beta_{a,532}(r)}{\beta_{a,64}(r)}$  or  $\frac{\sigma_{a,532}(r)}{\sigma_{a,64}(r)}$ )  $\pm$  SD for each model (e.g. Biomass Burning model) are represented by two window-like lines (e.g., in Fig. 6.6, the mean ratio of  $\frac{\beta_{a,532}(r)}{\beta_{a,64}(r)} \pm$  SD for the Biomass Burning model is represented by two dash-dot lines). Fig. 6.10 shows the simulation results of the performance function for Biomass Burning, Urban/Industrial, Dust (spheroids) and Oceanic models.

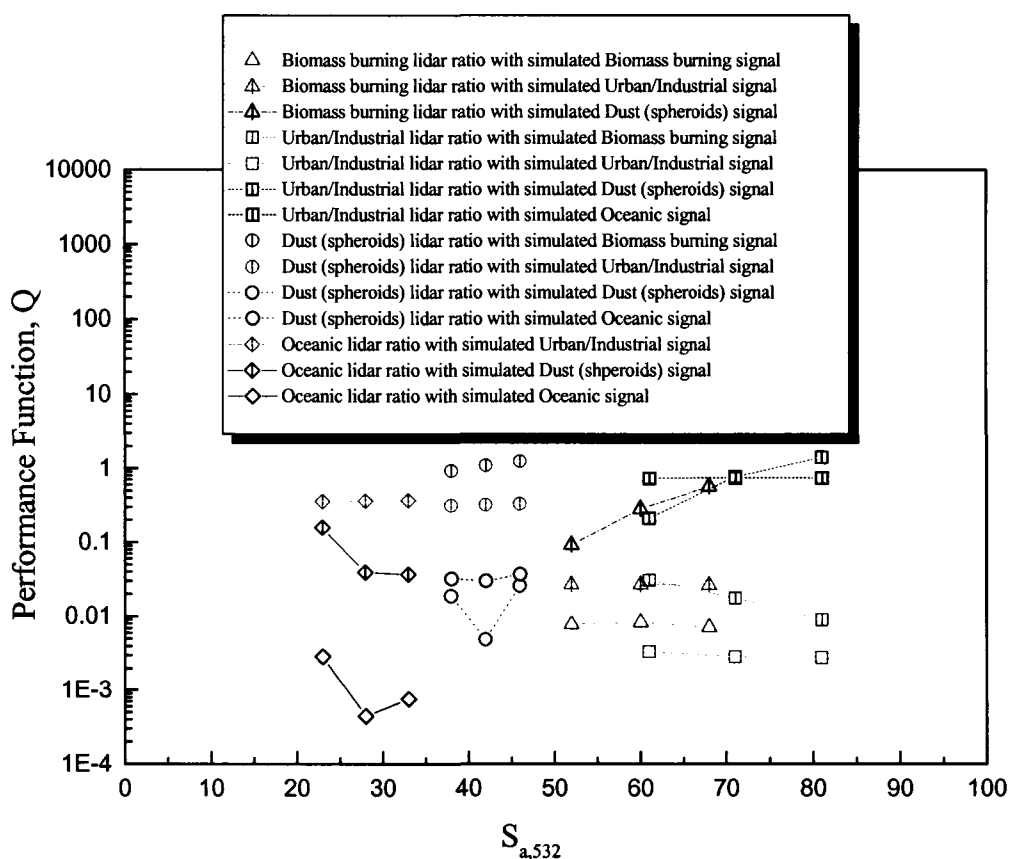


Fig. 6.10. Simulation results of performance function for Biomass Burning, Urban/Industrial, Dust (spheroids) and Oceanic models.

As can be seen from these figures, the retrieval results obtained by assuming the aerosol model  $S_a$  and  $S_a$  ratio values that correspond with the modeled signal (e.g., Dust parameters assumed for simulated Dust signal) are in excellent agreement with the corresponding ratios in Table 6.1. This is as expected. More importantly, the results from applying the  $S_a$  ratio from one aerosol type, such as Biomass Burning, to the simulated signals for another aerosol type (e.g., Dust case) show a significant disagreement between the retrieved backscatter/extinction ratios and the model backscatter/extinction ratios given in Table 6.1. This indicates that the table look-up approach, using improved, more defined  $S_a$  values and accompanying key spectral ratio parameters (i.e., 532 nm to 1064 nm ratios of backscatter and extinction), used as constraints, should be an effective aerosol retrieval approach, possibly definitively distinguishing between different aerosol types in different geographical locations and seasons.

As shown earlier in Chapter 5, the choice of the  $S_a$  ratio (lidar ratio) and the uncertainty in the choice significantly affects the value and accuracy of the retrieved aerosol backscatter and extinction profiles. Using more accurate lidar ratios provided by improved global aerosol models (e.g., Table 6.1) will help improve the accuracy of vertically resolved aerosol extinction and backscatter profiles retrieved from spaceborne lidar observations. This, in turn, should enable more accurate characterization of global aerosol properties and radiative effects, thereby assisting climate modelers in better assessing aerosol climate change influences.

The results presented in this chapter have demonstrated that by using a revised table look-up approach with improved, more definitive  $S_a$  selection, the aerosol retrievals

will be more bounded, plus, through the use of model constraints on the spectral ratios of retrieved backscatter and extinction profiles, the validity of an assumed aerosol model can be confirmed or rejected. Further studies are required to more fully evaluate this approach, including realistic estimates of signal noise and calibration error effects, but these preliminary results bode well for the quantitative aerosol information that can be expected from the upcoming CALIPSO mission. Finally, the use of ancillary combined inputs such as from AERONET and MODIS should enable even more accurate determination of global aerosol properties.

## 7. SIMULATION OF MULTIPLE SCATTERING EFFECTS IN AEROSOL RETRIEVALS WITH DIFFERENT APPROACHES

For measurements from very elevated platforms (e.g., polar orbiting satellites) where the receiver-to-scattering medium range is very large, more multiple scattering will occur than for surface based lidars with the same FOV. In view of this, careful consideration of multiple scattering effects is required for the CALIPSO mission. In most previous studies, lidar retrievals have been based on the approximate single scattering lidar equation. But for satellite lidar systems such as CALIPSO, multiple scattering is enhanced, due to the above-mentioned reasons, requiring multiple scattering corrections for even relatively low aerosol optical depths [54]. A schematic diagram showing the multiple scattering effect for an airborne/spaceborne lidar system is given in Fig.7.1.

Recall from Chapter 1, Section 1.2.6, that lidar multiple scattering can be treated to first order by making use of a multiple-scattering factor  $\eta$  [50], which reduces the aerosol extinction-to-backscatter ratio,  $S_a$ , to an effective value  $S_a^* = \eta S_a$ . Assessment of multiple scattering effects for a reasonable range of  $\eta$  values via a combination of retrieval methods will be presented in the following sections. As shown in what follows, given the value of  $\eta$ , the multiple scattering effects can be corrected based on the multiple/single scattering simulations for 532/1064 nm.

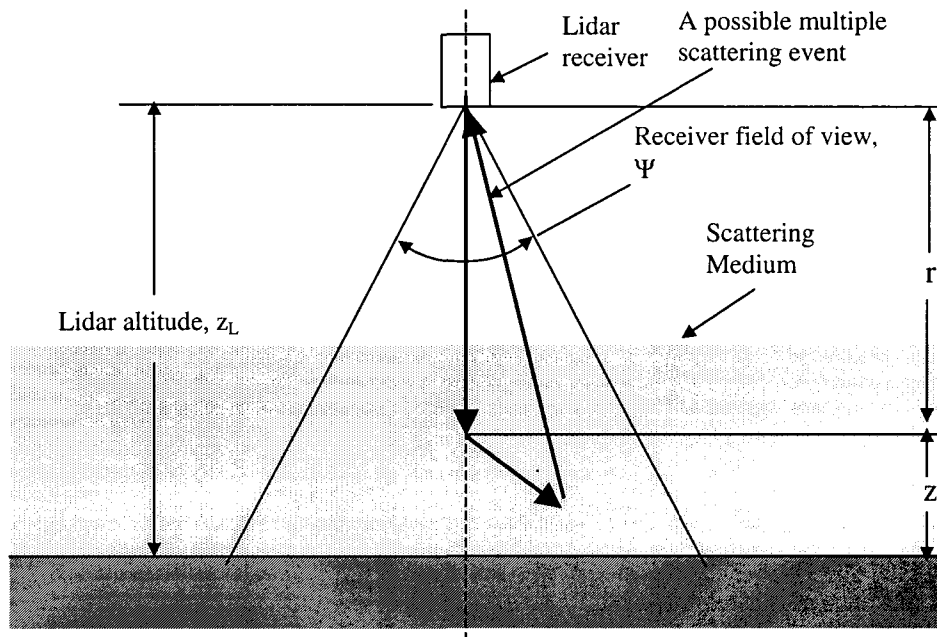


Fig. 7.1 A schematic diagram of the multiple scattering effect for a spaceborne lidar.

## 7.1 A Simple Analytic Algorithm for Aerosol Multiple Scattering Effects

To first order, lidar multiple scattering effects can be modeled with an effective aerosol extinction-to-backscatter ratio  $S_a^* = \eta S_a$ , where  $\eta$  is a multiple scattering factor less than 1 [55, 94], which reduces extinction to account for enhanced scattering in the forward direction (i.e.,  $\sigma_a^*(r) = \eta S_a \beta_a(r)$ ). Multiple scattering is enhanced for the implicit geometry of satellite lidar (where the distance from the lidar to the scattering region is large), causing what can be a significant influence even for nominally small aerosol optical depths ( $\tau_a < 1$ ). Values of  $\eta$  ranging from  $\sim 0.5$  to 1 [54] are assumed to be representative of multiple scattering effects expected for the LITE orbit height and receiver field-of-view for typical aerosol types and  $\tau_a < 1$ .

There are several important factors that can affect the selection of the  $\eta$  values which include the lidar sensing geometry (receiver's FOV and the distance from the lidar to the target being sensed), phase function of the scatterers and the number of scatterers (i.e., aerosol loading) [54, 55]. As given earlier in Tables 2.1 and 2.3, the receiver FOV for LITE and CALIPSO are 3.5 mrad and 130  $\mu$ rad, respectively, while the altitudes for LITE and CALIPSO are ~260 km and 705 km, respectively. As shown in Fig. 7.1, the volume of the acceptance cone for a lidar system is determined by the receiver's FOV,  $\psi$ , and the distance  $r$ . The distance  $r$  for LITE is shorter than that of CALIPSO, but the larger receiver FOV of LITE makes the volume of the acceptance cone of LITE greater than that of CALIPSO. Thus, the multiple scattering effect is more significant for LITE than CALIPSO. Several groups of  $\eta$  values predicted from Monte Carlo studies [95], which correspond to the LITE and CALIPSO geometries, are given in Figs 7.2 and 7.3. The results are for an elevated dust layer model (5 km thick) and a few different scatterer phase functions representative of dust. These two figures reveal that the  $\eta$  values for LITE are significantly lower than for CALIPSO, demonstrating the more serious multiple scattering contamination effects to be expected in LITE signals.

The approaches for solving the lidar equation introduced in previous chapters were based on the assumption of single scattering. Considering that multiple scattering effects could cause significant errors, corrections need to be developed to assess the impact of multiple scattering on these aerosol retrieval approaches, both for 532 and 1064 nm. Multiple scattering effects are investigated for the three typical solution approaches,

namely, the Auxiliary-Transmittance, Self-Transmittance and Modeled- $S_a$  approaches, for both 532 nm and 1064 nm [9, 53, 93]. Following the notations used in Chapter 1, the

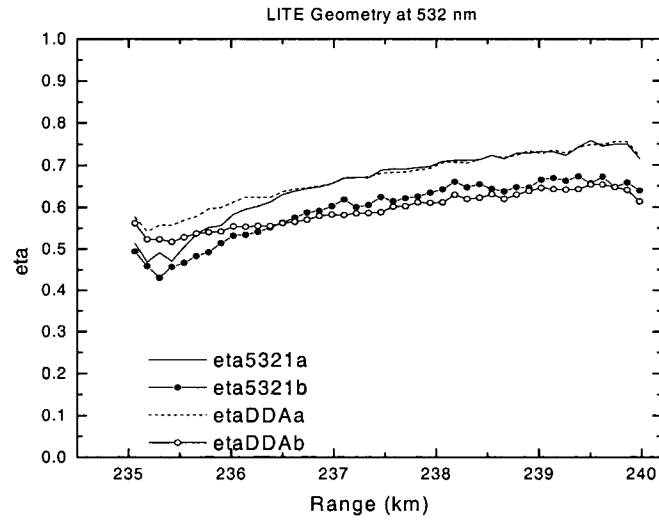


Fig. 7.2. The modeled LITE  $\eta$  values for elevated dust layer model with  $\sigma_a=0.2/\text{km}$  and  $0.6/\text{km}$  respectively at 532 nm [95].

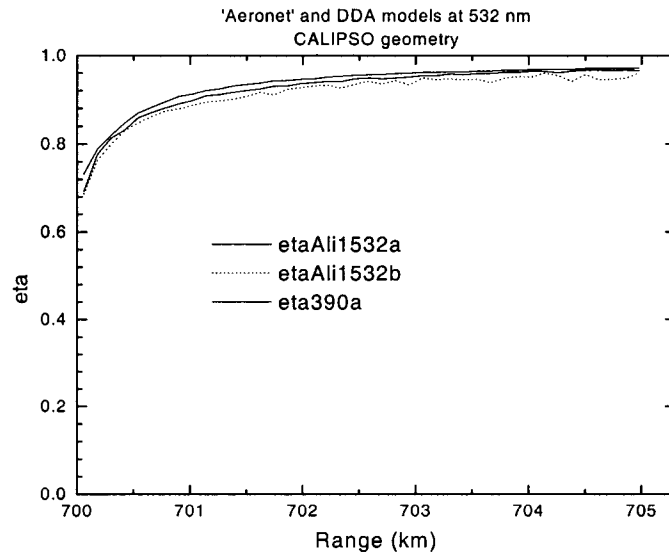


Fig. 7.3. The modeled CALIPSO  $\eta$  values for elevated dust layer model with  $\sigma_a=0.2/\text{km}$  and  $0.6/\text{km}$  respectively at 532 nm [95].

aerosol backscatter signals, extinction-to-backscatter ratio, extinction and backscattering coefficients for single scattering are hereafter expressed as  $X_a(r)$ ,  $S_a$ ,  $\sigma_a(r)$  and  $\beta_a(r)$ , while for multiple scattering they become  $X_a^*(r)$ ,  $S_a^*$ ,  $\sigma_a^*(r)$  and  $\beta_a^*(r)$ .

### 7.1.1 Aerosol Retrieval Approaches and General Considerations at 532 nm

The modeled aerosol structural features considered in this chapter are the elevated layer and mixed layer/boundary layer models, which were introduced earlier in Chapters 5 and 6. The effects of multiple scattering have been simulated for different assumed values of  $\eta$ . In these simulations,  $\beta_a(r)$  profiles were constructed, which are representative of what has typically been observed for aerosols around the world (e.g., as revealed in LITE observations).

#### *A. Elevated Dust Layer Model*

A nominal value of  $S_a = 35$  and different values of  $\eta$ , ranging from 0.5 to 1.0, have been assumed for the simulated multiple scattering signals of the elevated dust layer model, with aerosol optical depth  $\tau_a = 0.5$  for 532 nm. This falls within the range that has often been assumed for dust and relatively clean continental aerosols. Different aerosol optical depths ( $\tau_a = 0.2, 0.5, 0.8$ ) and a fixed  $\eta$  value ( $\eta = 0.7$ ) have also been employed in the simulation to further investigate how multiple scattering affects the retrieval errors with respect to different aerosol optical depths.

If we have a known calibration constant,  $C_{532}$ , a known backscattering coefficient profile  $\beta_a(r)$  and an assumed “true  $S_a$ ”, the single scattering signal,  $X(r)$ , from (2.9), is given by

$$X(r) = C_{532} [\beta_a(r) + \beta_R(r)] e^{-2 \int_0^r [S_a \beta_a(r) + S_R \beta_R(r)] dr} \quad (7.1)$$

The multiple scattering signals corresponding to different  $\eta$  values can then be expressed by

$$X^*(r) = C_{532} [\beta_a(r) + \beta_R(r)] e^{-2 \int_0^r [S_a \eta \beta_a^*(r) + S_R \beta_R(r)] dr} \quad (7.2)$$

The first aerosol retrieval approach considered here is the Self-Transmittance or isolated layer approach, using (2.27), wherein the aerosol layer two-way transmittance,  $T_a^2(r_1 \rightarrow r_2)$ , is estimated from the difference in lidar signal above and below an elevated layer embedded in otherwise clean air. The aerosol retrieval procedures, at 532 nm, with this Self-Transmittance approach and the following Aux-Transmittance and Modeled- $S_a$  approaches have been explained in detail in Chapter 5.

As mentioned earlier, the Aux-Transmittance approach is almost the same as the Self-Transmittance method. However, it is important to note that the aerosol transmittance/optical depth provided by these auxiliary observations is not affected by multiple scattering. The auxiliary aerosol transmittance is typically obtained for the aerosol mixed boundary layer over the surface. In the elevated dust layer case, the aerosol optical transmittance/optical depth is provided by the simulation, which gives a simulated two-way single scattering aerosol transmittance/optical depth through the dust layer (e.g.,

$T_a^2(r_1 \rightarrow r_2) = \exp[-2\tau_a(r_1 \rightarrow r_2)] = \exp\left[-2 \int_{r_1}^{r_2} S_a \beta_a(r) dr\right]$ , where  $r_1$  is the range from lidar to the dust layer top and  $r_2$  is the range from lidar to the dust layer bottom). A flow chart for the Self-Transmittance and Auxiliary-Transmittance approaches is shown in Fig.7.4.

Using the Modeled- $S_a$  approach, a value of 35 for  $S_a$  is substituted into (2.27) to get the aerosol backscattering coefficients,  $\beta_a^*(r)$ . The two-way aerosol transmittance through the dust layer,  $T_a^{2*}(r_1 \rightarrow r_2)$ , is obtained by  $T_a^{2*}(r_1 \rightarrow r_2) = \exp\left[-2 \int_{r_1}^{r_2} S_a \beta_a^*(r) dr\right]$ .

The aerosol backscattering signal at 532 nm again is given by

$$X_a^*(r) = C_{532} \beta_a(r) e^{-2 \int_0^r S_a(r) \eta \beta_a(r) dr} e^{-2 \int_0^r S_R(r) \beta_R(r) dr} \quad (7.3)$$

and  $S_a^*$  can be obtained from (2.42), which yields

$$S_a^* = \frac{C_{532} \left[1 - T_a^{2*}(r_1 \rightarrow r_2)\right]}{\int_{r_1}^{r_2} 2 X_a^*(r) dr} \quad (7.4)$$

### B. Boundary Layer Model

The multiple scattering effect for an aerosol mixed layer/boundary layer model was simulated with a value of 40 for  $S_a$  and  $\eta$  values ranging from 0.5~1.0. The aerosol optical depth assumed in the boundary layer model simulation is 0.2. Following the simulation procedure for the elevated dust layer model, different aerosol optical depths ( $\tau_a=0.03, 0.06, 0.1, 0.2, 0.3$ ) for the same  $\eta$  value ( $\eta = 0.7$ ) have also been applied in the simulation to extend the investigation of the relationship between the retrieval errors and the aerosol optical depths.

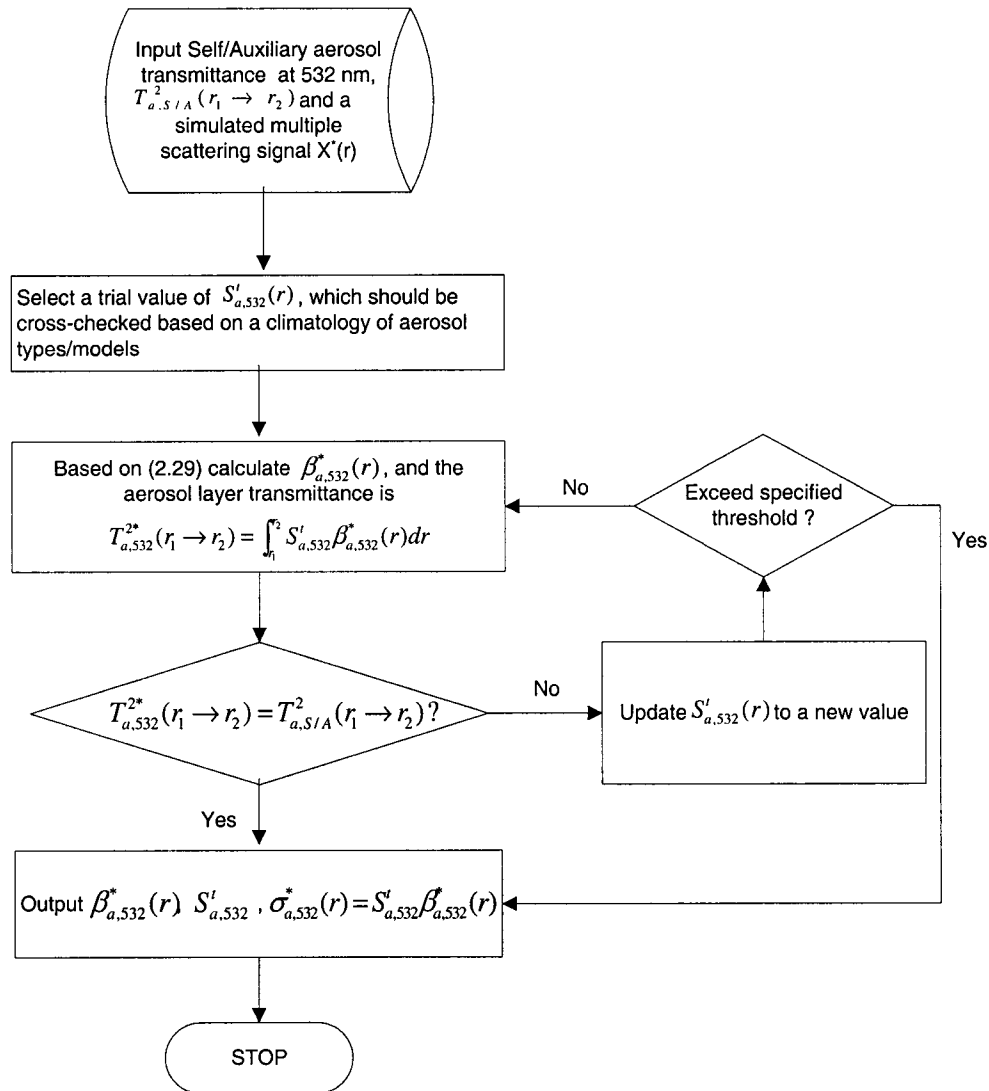


Fig. 7.4. A schematic flow chart of Self/Auxiliary-Transmittance approach at 532 nm.

The Auxiliary-Transmittance and the Modeled- $S_a$  approaches used for the boundary layer model are the same as that for the elevated dust layer model, which were described in detail in Chapter 5. For the boundary layer model, because there is no “clean

air” region which exists below the aerosol layer bottom, the transmittance through the boundary layer for the Self-Transmittance approach was obtained by

$$T_a^{2*}(r_1 \rightarrow r_2) = \exp\left[-2 \int_{r_1}^{r_2} S_a \eta \beta_a(r) dr\right].$$

### 7.1.2 Aerosol Retrieval Approaches at 1064 nm

The three different aerosol retrieval approaches applied for 532 nm are also used in the 1064 nm simulations, but as given earlier, the equations used for these three approaches at 1064 nm are different. The modeled- $S_a$  approach for retrieving  $\sigma_a^*(r)$  is based on (2.40), while both the Self-Transmittance and Aux-Transmittance approaches at 1064 nm use (2.41) to retrieve  $\sigma_a^*(r)$ . A retrieved  $S_a^*$  value was obtained for all these three approaches by use of (2.42) with the retrieved aerosol transmittance,

$$T_a^{2*}(r_1 \rightarrow r_2) = \exp\left[-2 \int_{r_1}^{r_2} \sigma_a^*(r) dr\right].$$

The same aerosol models, (boundary layer model and elevated layer model) were also selected for the 1064 nm simulations. For the purpose of investigating multiple scattering effects, the values of  $S_a$  for the 1064 nm simulations were assumed the same as those assumed for 532 nm in both the boundary layer model and elevated dust layer model. All the procedures for 532 nm aerosol retrieval approaches were repeated for 1064 nm with the same assumptions for the simulation parameters.

## 7.2 Simulation Results and Discussion

The simulation results based on Section 7.1.1, part A, are given in Figs. 7.5 and 7.6, which show the relationship for the average relative bias errors of  $S_a^*$ ,  $\sigma_a^*(r)$  and  $\beta_a^*(r)$  for the elevated aerosol layer model at 532 nm versus  $\eta$  and  $\tau_a$ , respectively. In addition, some simulation results based on Fig. 7.2 are also shown in these two figures. In Fig.7.2, the multiple scattering factor,  $\eta$ , is a variable rather than a constant, varying somewhat with altitude within the aerosol layer. The  $\eta$  values selected from Fig. 7.2 are for the elevated dust layer model with the LITE geometry. Two groups of  $\eta$  values were applied in the simulations:

1. etaDDAa model:  $\bar{\eta} \approx 0.67$  and  $\sigma_a=0.2/\text{km}$
2. etaDDAb model:  $\bar{\eta} \approx 0.59$  and  $\sigma_a=0.6/\text{km}$

and the simulation results ( $\eta$  as variable and an averaged constant value,  $\bar{\eta}$ ) are also shown in Figs 7.5 and 7.6.

The relationships for the averaged relative bias errors of  $S_a^*$ ,  $\sigma_a^*(r)$  and  $\beta_a^*(r)$  with regard to  $\eta$  and  $\tau_a$  at 1064 nm are shown in Figs 7.7 and 7.8, respectively, for the elevated aerosol layer model and boundary layer model. Figs. 7.9 through 7.12 show the retrieved aerosol extinction and backscattering profiles at 532 and 1064 nm for the constructed single scattering and multiple scattering affected retrieved signals.

The simulation results for Self-Transmittance method have shown that for both wavelengths the average relative bias errors for backscattering coefficients are within 5%.

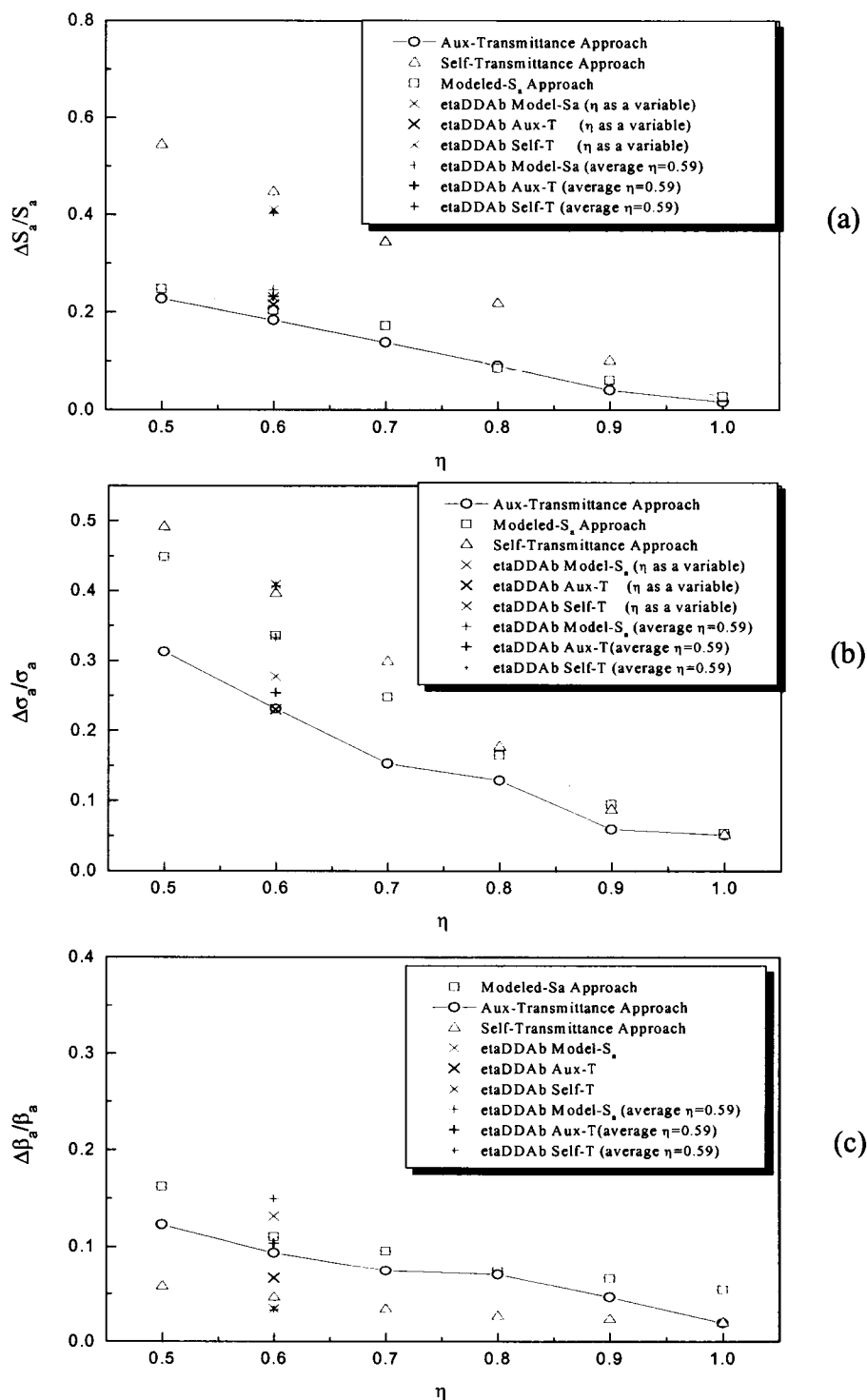


Fig. 7.5. The averaged relative retrieval uncertainties versus  $\eta$  for elevated aerosol layer model at 532 nm ( $\tau_a = 0.5$ ), (a)  $\Delta S_a/S_a$  vs.  $\eta$  (b)  $\Delta \sigma_a/\sigma_a$  vs.  $\eta$  (c)  $\Delta \beta_a/\beta_a$  vs.  $\eta$ .

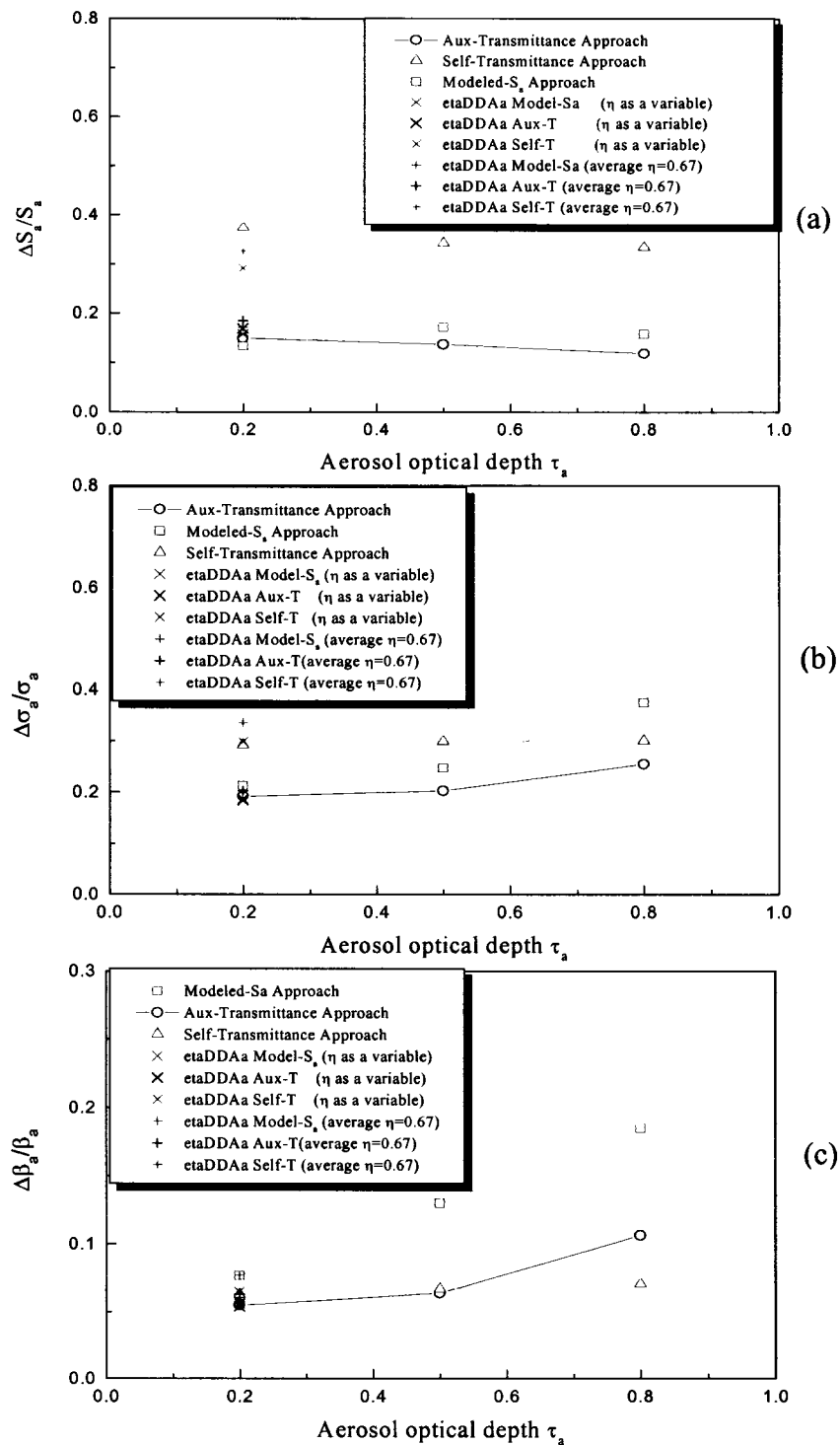


Fig. 7.6. The averaged relative retrieval uncertainties versus  $\tau_a$  for elevated aerosol layer model at 532 nm ( $\eta = 0.7$ ), (a)  $\Delta S_a/S_a$  vs.  $\tau_a$  (b)  $\Delta \sigma_a/\sigma_a$  vs.  $\tau_a$  (c)  $\Delta \beta_a/\beta_a$  vs.  $\tau_a$ .

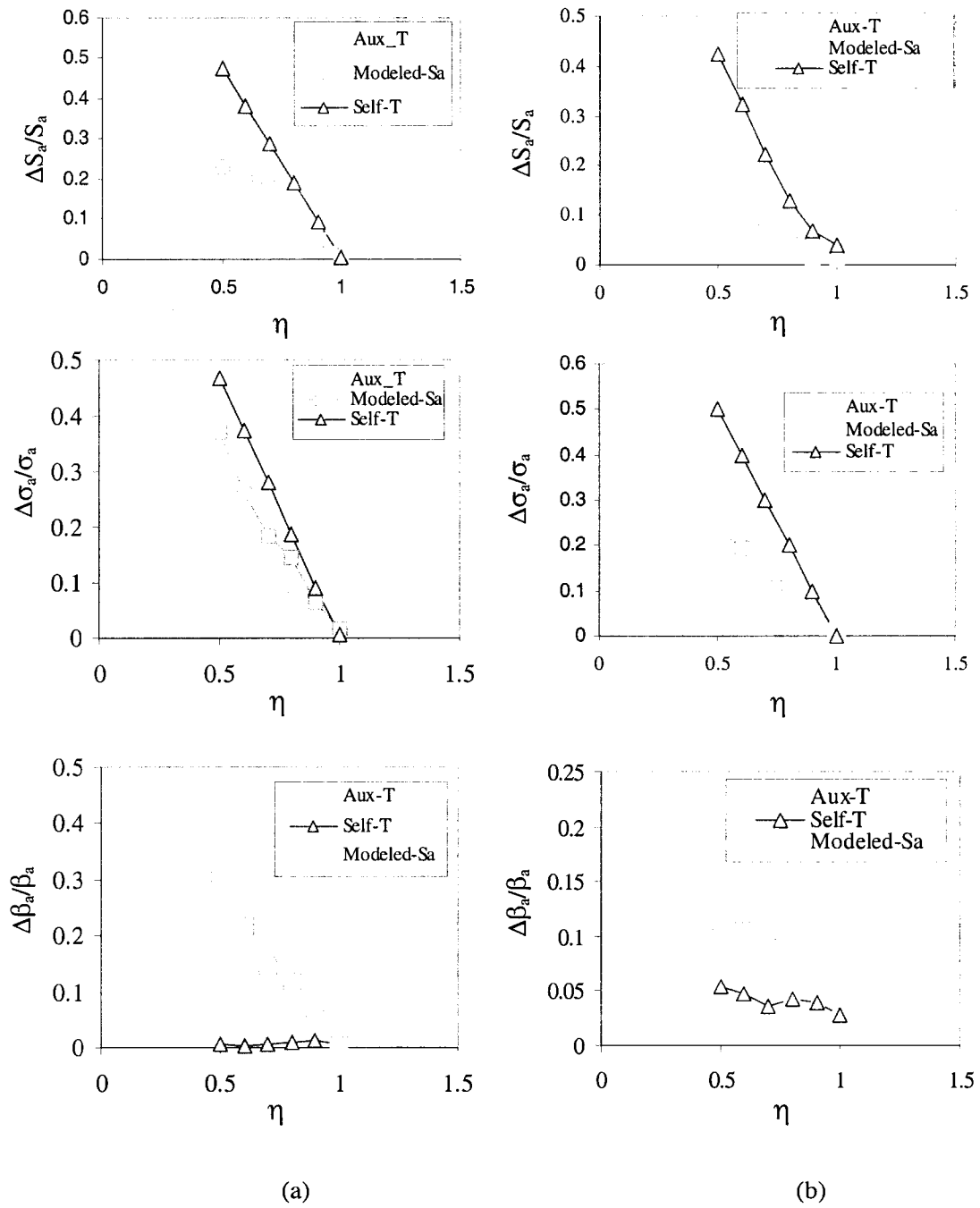


Fig. 7.7. The averaged relative retrieval uncertainties versus  $\eta$  at 1064 nm for (a) elevated aerosol layer model ( $\tau_a = 0.5$ ), (b) boundary layer model ( $\tau_a = 0.2$ ).

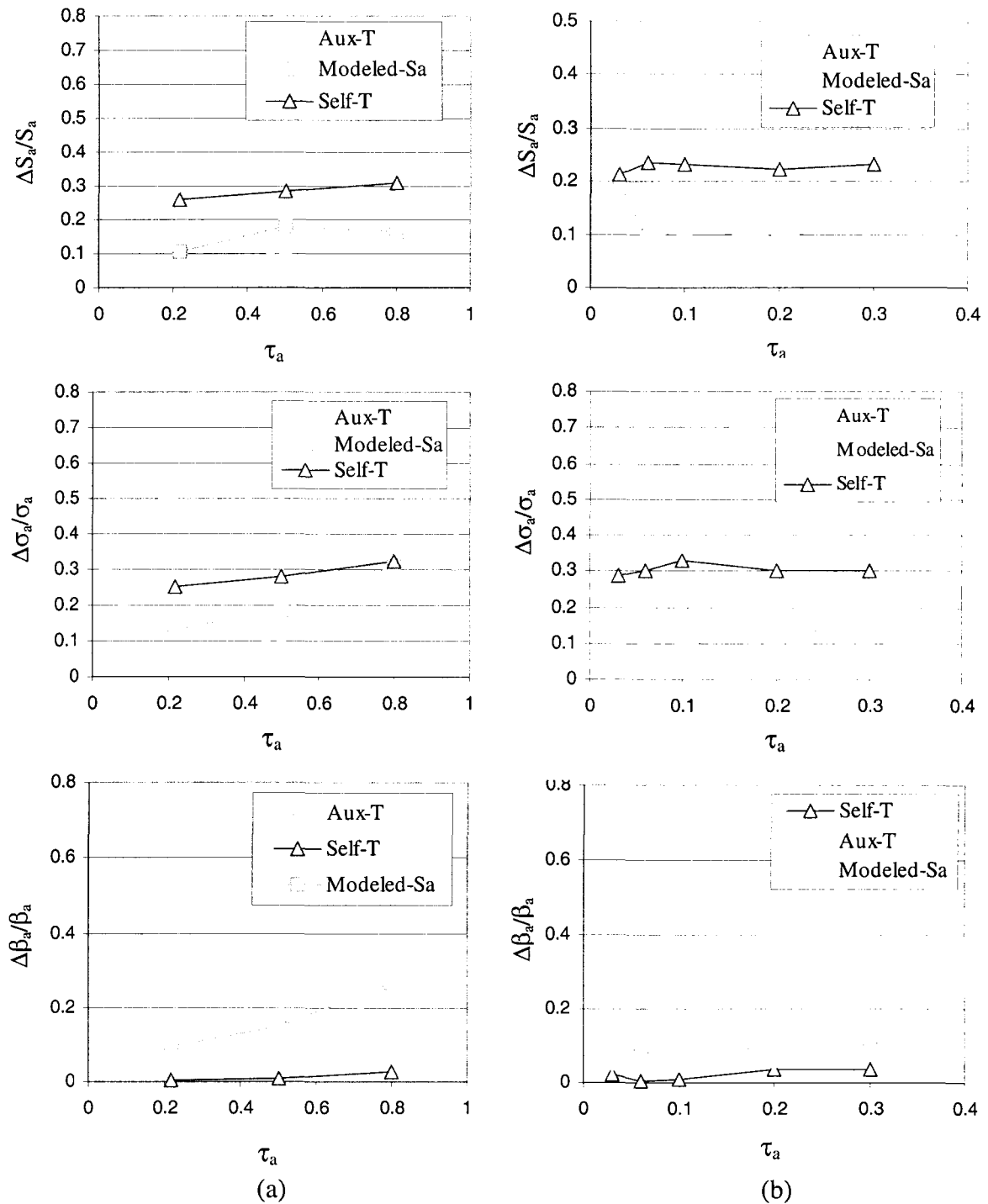


Fig. 7.8 The averaged relative retrieval uncertainties versus  $\tau_a$  at 1064 nm for (a) elevated aerosol layer model ( $\eta=0.7$ ), (b) boundary layer model ( $\eta=0.7$ ).

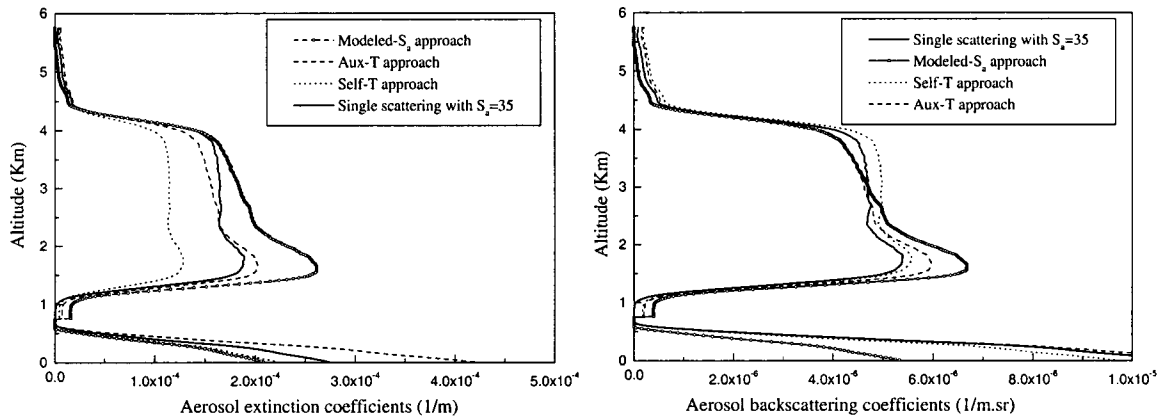


Fig. 7.9. Retrieved aerosol extinction and backscattering profiles from simulated single and multiple scattering signals ( $\eta=0.7$  and  $\tau_a=0.5$  at 532 nm, elevated layer model).

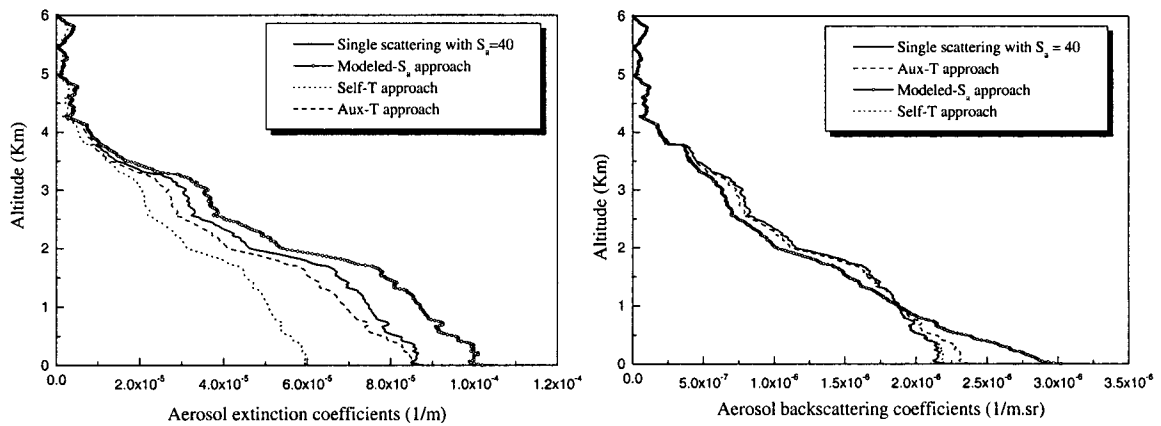


Fig. 7.10. Retrieved aerosol extinction and backscattering profiles from simulated single and multiple scattering signals ( $\eta=0.7$  and  $\tau_a=0.2$  at 532 nm, boundary layer model).

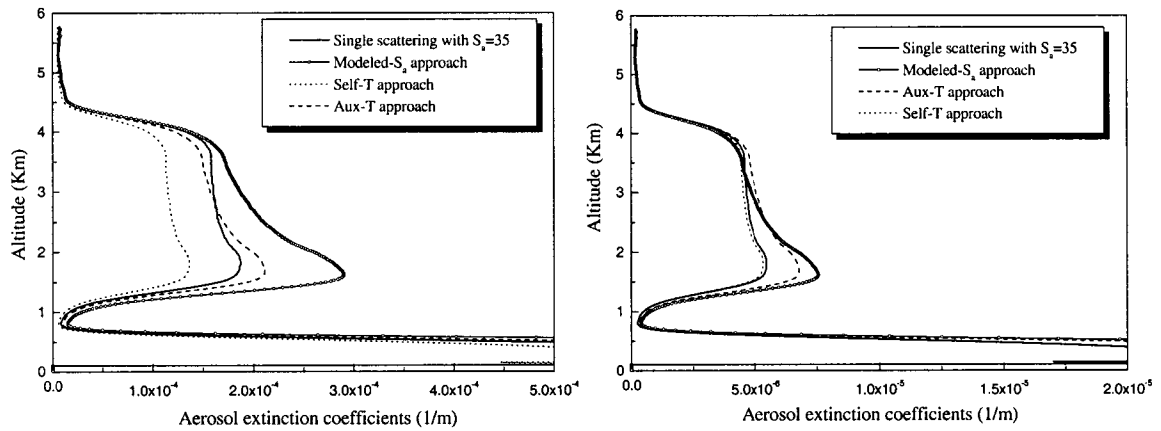


Fig. 7.11. Retrieved aerosol extinction and backscattering profiles from simulated single and multiple scattering signals ( $\eta=0.7$  and  $\tau_a=0.5$  at 1064 nm, elevated layer model).

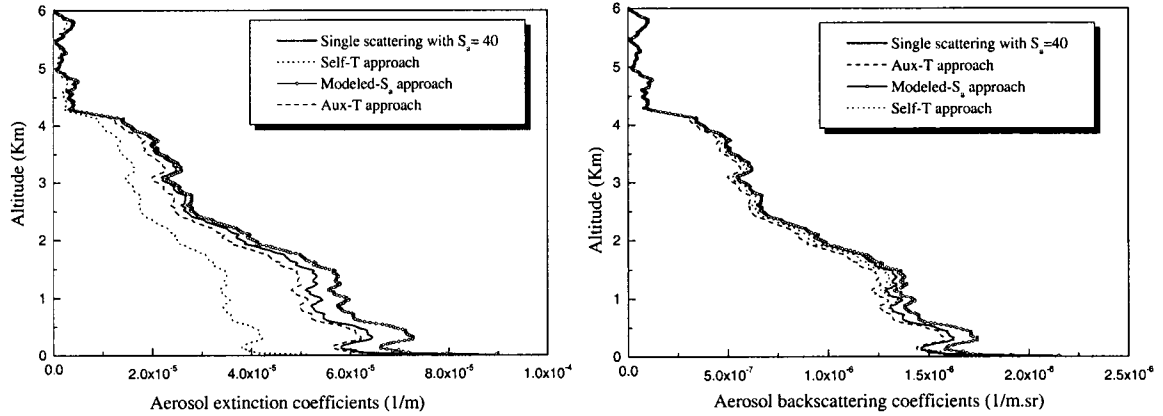


Fig. 7.12. Retrieved aerosol extinction and backscattering profiles from simulated single and multiple scattering signals ( $\eta=0.7$  and  $\tau_a=0.2$  at 1064 nm, boundary layer model).

The retrieved aerosol extinction-to-backscatter ratio and extinction coefficients,  $S_{a,Self}^*$  and  $\sigma_{a,Self}^*(r)$ , can be approximately corrected by multiplying by the factor  $1/\eta$ , where the subscript "Self" represents the Self-Transmittance method. Hereafter, "Aux" and "Mod" will also be used for Aux-Transmittance and Modeled- $S_a$  methods. As can be seen in the simulation results for the Aux-Transmittance approach, the retrieved backscattering coefficients,  $\beta_{a,Aux}^*(r)$ , extinction coefficients,  $\sigma_{a,Aux}^*(r)$ , and  $S_{a,Aux}^*$  for both aerosol models (elevated layer model and boundary layer model) and the two wavelengths (532 and 1064 nm) agree fairly well with the corresponding parameters of the constructed single scattering signals. If  $\eta > 0.7$ , the errors fall within ~10%.

For both aerosol models and wavelengths, the simulation results show that the Modeled- $S_a$  approach incurred the worst errors in  $\beta_{a,Mod}^*(r)$ . However, if the aerosol optical depth is less than 0.4 and the  $\eta$  value is greater than 0.7, the average relative bias errors for  $\beta_{a,Mod}^*(r)$ ,  $\sigma_{a,Mod}^*(r)$  and  $S_{a,Mod}^*(r)$  are still acceptable (within ~15%). For a fixed  $\eta$  value, such as  $\eta = 0.7$ , the variation of the errors in  $\beta_a^*(r)$ ,  $\sigma_a^*(r)$  and  $S_a^*(r)$  with regard to changing the aerosol optical depth is fairly flat, which suggests that the correction for multiple scattering effect will not be strongly affected by the aerosol optical depth.

With a fixed aerosol optical depth value (e.g.,  $\tau_a = 0.2$  or  $0.5$ ), the errors in  $\beta_a^*(r)$ ,  $\sigma_a^*(r)$  and  $S_a^*(r)$  with regard to the  $\eta$  values all increase significantly, in approximate linear fashion, as  $\eta$  decreases from 1. This clearly shows how important it is to specify a

fairly accurate  $\eta$  value when applying a correction algorithm for multiple scattering effects. Due to the error compensating effects, while the Self-Transmittance approach yields the largest error in  $\sigma_a^*(r)$  and  $S_a^*(r)$  versus  $\eta$ , the error in  $\beta_a^*(r)$  is the lowest among all three aerosol retrieval approaches. The results presented show that the Auxiliary-Transmittance approach is generally the best approach with the lowest errors in  $\sigma_a^*(r)$  and  $S_a^*(r)$ , while next to the lowest in  $\beta_a^*(r)$ . This suggests that it is possible to keep retrieval errors very low by use an approximate  $\eta$  correction with this approach. The simulation results show that errors in  $\beta_a^*(r)$ ,  $\sigma_a^*(r)$  and  $S_a^*(r)$ , even if  $S_a$  is known correctly, can be significant for the modeled  $S_a$  approach. Hence, it is important to employ a  $\eta$  correction algorithm when using this approach.

Correctional relations to correct  $S_a$ ,  $\sigma_a(r)$  and  $\beta_a(r)$  retrievals with known  $\eta$  were obtained for some examples. Fig. 7.13 shows the correctional relations ( $\Delta S_a/S_a$ ,  $\Delta\sigma_a/\sigma_a$  and  $\Delta\beta_a/\beta_a$  versus known  $\eta$ ) for the elevated aerosol layer model at 532 nm ( $\tau_a = 0.5$ ) and Fig. 7.14 shows the correctional relations for the aerosol boundary layer model at 1064 nm ( $\tau_a = 0.2$ ). The correctional relations shown in Figs. 7.13 and 7.14 are all quite linear, fitted by the lines shown in the figures. In Fig. 7.14, the linear fits follow the notation where “y” denotes  $\Delta S_a/S_a$  in part (a),  $\Delta\sigma_a/\sigma_a$  in part (b) and  $\Delta\beta_a/\beta_a$  in part (c), while notation “x” denotes  $\eta$  in parts (a), (b) and (c). Some examples can be employed here to demonstrate how to make the corrections for the multiple scattering effects. In Fig. 7.13, with  $\tau_a = 0.5$ , the fitted relationship,  $\Delta\sigma_a/\sigma_a = 0.819 - 0.793\eta$ , is for the Modeled- $S_a$  approach and the elevated aerosol layer model. Given  $\eta = 0.7$ , the corresponding relative

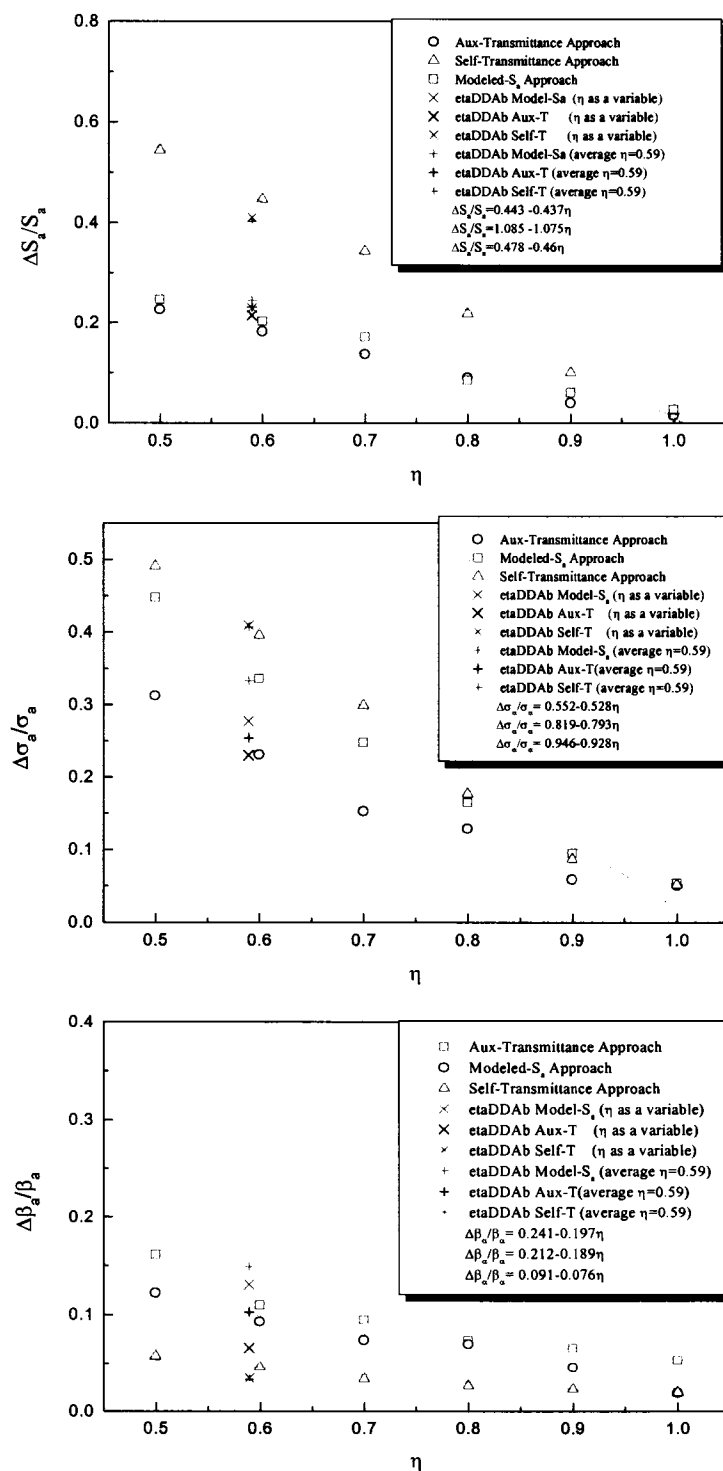


Fig. 7.13. The correctional relations for  $S_a$ ,  $\sigma_a(r)$  and  $\beta_a(r)$  with known  $\eta$  for the elevated aerosol layer model at 532 nm ( $\tau_a=0.5$ ).

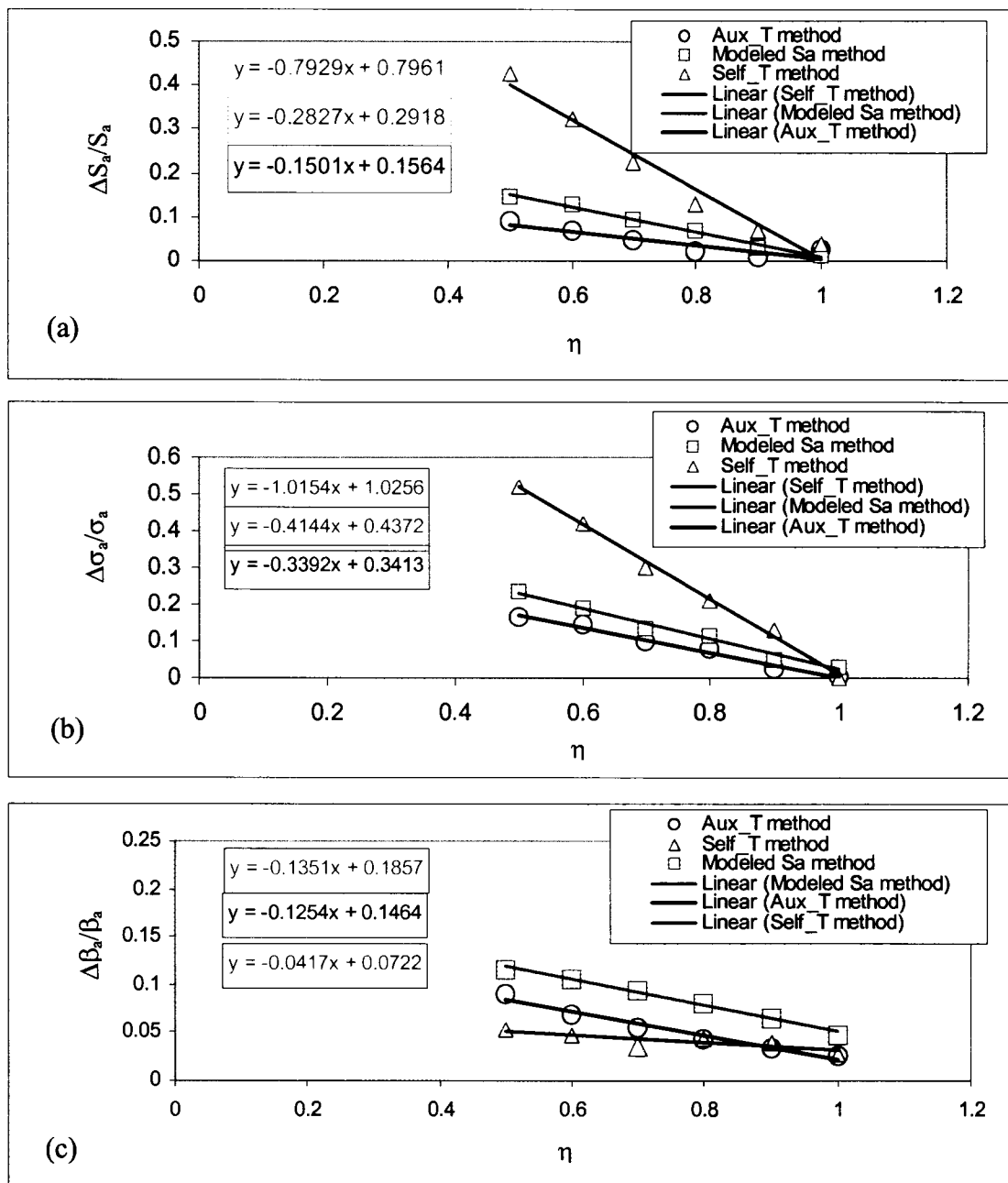


Fig. 7.14. The correctional relations for  $S_a$ ,  $\sigma_a(r)$  and  $\beta_a(r)$  with known  $\eta$  for the aerosol boundary layer model at 1064 nm ( $\tau_a=0.2$ ).

bias error for  $\Delta\sigma_a/\sigma_a$  is  $\sim 0.264$ , which can be used to correct the retrieved aerosol extinction coefficients from the signals with multiple scattering effects. Likewise, the bias error for the aerosol backscattering coefficients, caused by multiple scattering effects, can also be corrected by the fitted relationship,  $\Delta\beta_a/\beta_a = 0.241 - 0.197\eta$ , for the Modeled- $S_a$  approach and elevated aerosol layer model, for a given  $\eta$  value.

The corrections for the three aerosol retrieval approaches (Self-Transmittance, Aux-Transmittance and Modeled- $S_a$  approaches) and aerosol boundary layer model are the same as that for the elevated aerosol layer model. For example, in Fig. 7.14, the fitted relationship for the Aux-Transmittance approach is  $\Delta\sigma_a/\sigma_a = -0.3392\eta + 0.3413$ . Given  $\eta = 0.6$ , the value of  $\Delta\sigma_a/\sigma_a$  is 0.138.

The simulations for the three aerosol retrieval approaches with respect to two aerosol models (elevated layer model and boundary layer model) have shown that the difference between the use of  $\eta$  as a variable or a constant (mean value) can be neglected. In particular, the results show that using a mean  $\eta$  value in the three aerosol retrieval approaches will not make a big difference from treating  $\eta$  as a variable with the spatial behavior shown in Fig. 7.2, which is representative of what can be expected for other reasonable aerosol phase functions (i.e., for other reasonable aerosol types).

An actual 532 nm lidar signal profile, selected from LITE orbit 83 was also used in the simulation with  $\eta$  either to be a variable or a mean value. The Self-Transmittance approach was applied to the selected LITE signal profile, which includes the multiple scattering effects. The simulated single scattering aerosol extinction coefficients,  $\sigma_a(r)$ , were compared to the corrected multiple scattering aerosol extinction coefficients,

$\sigma'_a(r) = \sigma_a^*(r)/\eta$ . The results in Fig. 7.15 show that the relationship  $\sigma_a(r) = \sigma_a^*(r)/\eta$  is quite accurate for correcting multiple scattering effects (assuming correct  $\eta$  is employed).

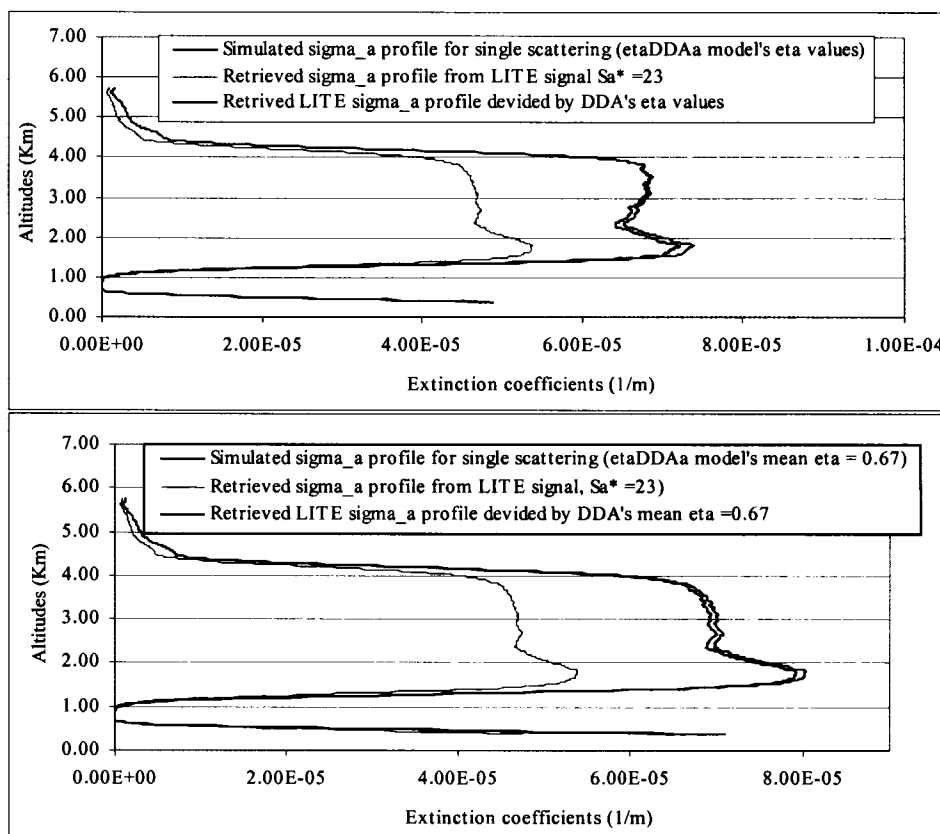


Fig. 7.15. Retrieved aerosol extinction profiles from LITE and simulated single scattering signals.

In summary, simulations have been presented in this chapter for different aerosol optical depths, different  $\eta$  values and different aerosol models (i.e.,  $\tau_a = 0.2$ ,  $\eta = 0.5\sim 1.0$  for the aerosol boundary layer model) to assess the effects of multiple scattering on aerosol retrievals made using single-scattering retrieval relations. While the simulation results show that multiple scattering can cause significant errors in the retrieved backscatter and extinction profiles, these errors can be corrected fairly accurately given

the value of  $\eta$ . In particular, it was found that the retrieval errors could be linearly related to  $\eta$ , thereby permitting formulation of general correction relationships for any  $\eta$  value within the practical range of  $\eta$ .

## 8. CONCLUSIONS AND FUTURE WORK

### 8.1 Conclusions

In this dissertation, techniques have been presented for on-orbit calibration of spaceborne lidar applicable for both shorter visible wavelengths, such as 532 nm, and longer near infrared wavelengths, such as 1064 nm. The shorter wavelength approach employs molecular (Rayleigh) scattering normalization at high altitudes (~30 km), while the longer wavelength approach determines the ratio of the longer to shorter wavelength calibration factors from selected cirrus cloud backscatter returns. These approaches have been demonstrated using example data from the LITE shuttle mission, including assessment of uncertainties. Analogous to what was done for the LITE shuttle mission, the calibration of the CALIPSO 532 nm channel by molecular normalization is quite feasible and should yield calibrations with uncertainties of  $\pm 5\%$  or less. Calibration of the CALIPSO 1064 nm channel in terms of, or as a ratio to, the 532 nm calibration factor by using cirrus cloud returns also appears quite feasible and the accuracy can be, conservatively,  $\pm 10\%$  or less by selecting strong signal returns from cirrus clouds.

The results in Chapter 4 showed that using the modeled depolarization factor for CALIPSO, 0.00394, made little difference from using the well-known depolarization factor, 0.0036, which is for Cabannes scattering. The depolarization factor affects the calibration constant by modifying the volume molecular backscattering cross section with the same constant factor (e.g., the same anisotropy correct factor,  $F_k$ , for orbits 24 and 83). In the 532 nm calibration of CALIPSO, compared to the use of 0.0036 as the

depolarization factor for the receiver filter bandwidth of CALIPSO, the use of 0.0279 and 0.0141 can cause errors as about 4% and 2%, respectively. Chapter 4 also presented the estimates of  $R$  characteristics of clean air regions, which are within ~8 to 16 km above ground where the minimum backscatter ratio is generally observed. Errors in recovering  $R$  resulting from the uncertainties in the calibration constant at a higher altitude and two-way transmission from the calibration reference height were simulated and assessed. With the obtained relative uncertainties of  $R_{\min}$ ,  $\beta_R(z)$ ,  $X(z)$  at the lower calibration height,  $z^*$ , the relative uncertainty of  $C^*T^2(z^*)$  at 532 nm has been evaluated. The simulations have shown that the relative uncertainties of  $C^*T^2(z^*)$  can be constrained lower than 5%, demonstrating that the Rayleigh normalization at a lower altitude can be used as a backup or alternative check for the calibration of the 532 nm channel.

With revised calibration approaches and techniques/models, some actual LITE data (i.e., orbits 24, 83 and 103) were used in simulations to estimate various uncertainties in the aerosol retrievals. The retrieval results from LITE data in Chapter 5 do not account for or correct for multiple scattering effects, which can be very significant and have been discussed in more detail in Chapter 7. Different error sources in the aerosol retrieval were assessed and analyzed, which included analyses of an inaccurate assumed extinction-to-backscatter ratio ( $S_a$ ), calibration error, random error in the normalized lidar signals and random error in Rayleigh backscattering. The LITE simulation results for the Saharan dust layer case showed that within the dust layer the relative uncertainty of the aerosol backscattering coefficient,  $\Delta\beta_a(z)/\beta_a(z)$ , due to the bias  $S_a$  error is more dominant compared to the  $\Delta\beta_a(z)/\beta_a(z)$  caused by other error sources.

Some controlled simulations for the two selected aerosol models (elevated aerosol layer model and boundary aerosol layer model) have shown that within the aerosol layer the relative uncertainty in aerosol extinction,  $\delta\sigma_a(z)/\sigma_a(z)$ , is larger than that of aerosol backscatter,  $\delta\beta_a(z)/\beta_a(z)$ , due to either  $S_a$  bias error or C bias error. Comparatively, the relative uncertainty  $\delta\sigma_a(z)/\sigma_a(z)$  or  $\delta\beta_a(z)/\beta_a(z)$  for the elevated aerosol layer type is larger than that for the boundary aerosol layer type. When the assumed relative  $S_a$  bias error changes from 15% to 30%,  $\delta\sigma_a(z)/\sigma_a(z)$  and  $\delta\beta_a(z)/\beta_a(z)$  for the elevated aerosol layer type and  $\delta\sigma_a(z)/\sigma_a(z)$  for the boundary aerosol layer type become significantly larger. For both aerosol model types (elevated aerosol layer type and boundary aerosol layer type), the uncertainty of the aerosol backscattering/extinction coefficients, due to the C bias error, does not vary much through most of the aerosol layer. The value of  $\delta\sigma_a(z)/\sigma_a(z)$  or  $\delta\beta_a(z)/\beta_a(z)$ , due to the C bias error ( $\sim 5\%$ ), obtained for the two aerosol types is not more than 10%.

As shown earlier in Chapter 5, the choice of the  $S_a$  ratio (lidar ratio) and the uncertainty in the choice significantly affects the value and accuracy of the retrieved aerosol backscatter and extinction profiles. In Chapter 6, aerosol retrievals based on more accurate  $S_a$  estimates were introduced, and several aerosol models (i.e., Urban/Industrial, Dust (spheroids), Biomass burning and Oceanic etc.) were studied based on a two-wavelength lidar Constrained Ratio Aerosol Model-fit (CRAM) retrieval approach [90]. The results presented in this chapter have demonstrated that by using a revised table look-up approach with improved, more definitive  $S_a$  selection, the aerosol retrievals will be more bounded, plus, through the use of model constraints on the spectral ratios of

retrieved backscatter and extinction profiles, the validity of an assumed aerosol model can be confirmed or rejected.

A modeled multiple scattering factor,  $\eta$ , less than 1, which reduces  $S_a$  to an effective value  $S_a^* = \eta S_a$ , has been used to make an approximate, but quantitatively useful multiple scattering correction. In Chapter 7, by combining three aerosol retrieval approaches (Self-Transmittance, Auxiliary-Transmittance and Modeled- $S_a$ ), the multiple scattering effects for a reasonable range of  $\eta$  values were assessed with simulated multiple/single scattering signals at 532/1064 nm. Simulations have been presented in this chapter for different  $\eta$  values and different aerosol models (i.e.,  $\eta = 0.5\sim 1.0$  for the aerosol boundary layer and elevated layer models) to assess the effects of multiple scattering on aerosol retrievals made using single-scattering retrieval relations. It was found that the retrieval errors could be linearly related to  $\eta$  and the general correction relationships permit the errors caused by multiple scattering to be corrected fairly accurately given the value of  $\eta$ .

## 8.2 Future Work

In this dissertation research, significant contributions have been made to studies of spaceborne lidar calibration (532/1064 nm) at high (30-34 km above the ground) and lower altitude (8-16 km above the ground), the uncertainty and benefit of constraints of the aerosol extinction-to-backscatter ratio,  $S_a$ , on retrievals of aerosol backscatter and extinction, and the effects of multiple scattering, including correctional approaches, on these retrievals. With the approaches and results presented and discussed in previous

chapters, some further improvement and validation is to be expected when a more complete database is available. First, the upcoming CALIPSO and current GLAS missions will provide an opportunity to test the algorithms developed in this dissertation, such as the lidar calibration algorithm for 532/1064 nm, and the uncertainty analysis of  $CT^2(z^*)$  at a lower altitude. Second, the data from the upcoming CALIPSO and current GLAS missions will also provide a testbed to extend the aerosol retrieval error analysis due to aerosol extinction-to-backscatter ratio based on LITE data base. Third, further studies are required to more fully evaluate the spaceborne lidar aerosol retrieval approaches based on aerosol model constraints, including realistic estimates of signal noise and calibration error effects. The use of ancillary combined inputs such as from AERONET and MODIS should enable even more accurate characterization of global aerosol properties and radiative effects. Finally, more collaborative work (i.e., with NASA Langley research center) will be needed to establish improved estimates of  $\eta$  values and ranges for different aerosol types, profile types and lidar system parameters to implement effective algorithms for correcting multiple scattering effects.

## REFERENCES

- [1] P. Warneck, *Chemistry of the natural atmosphere*. San Diego, USA: Academic Press Inc., 1988.
- [2] W. E. K. Middleton and A. F. Sphillhaus, *Meteorological Instruments*. Toronto, Canada: University of Toronto Press, 1953.
- [3] G. G. Goyer and R. Watson, "The laser and its application to meteorology," *Bull. Amer. Meteorol. Soc.*, vol. 44, pp. 564-570, 1963.
- [4] G. Fiocco and L. D. Smullin, "Detection of scattering layers in upper atmosphere (60-140 km) by optical radar," *Nature*, vol. 199, pp. 1275-&, 1963.
- [5] G. Fiocco and G. Grams, "Observations of the aerosol layer at 20-km by optical radar," *Journal of the Atmospheric Sciences*, vol. 21, pp. 323-324, 1964.
- [6] M. G. H. Ligda, "Meteorological observations with pulsed laser radar," presented at Proc. 1st Conf. on Laser Tech., U.S. Navy, 1963.
- [7] R. T. H. Collis and M. G. H. Ligda, "Laser radar echoes from clear atmosphere," *Nature*, vol. 203, pp. 508-&, 1964.
- [8] R. T. H. Collis, M. G. H. Ligda, and F. G. Fernald, "Laser radar echoes from stratified clear atmosphere," *Nature*, vol. 203, pp. 1274-&, 1964.
- [9] J. A. Reagan, M. P. McCormick, and J. D. Spinhirne, "Lidar sensing of aerosols and clouds in the troposphere and stratosphere," *IEEE Proc.*, vol. 77, pp. 433-448, 1989.
- [10] D. M. Winker, R. H. Couch, and M. P. McCormick, "An overview of LITE: NASA's lidar in-space technology experiment," *IEEE Proc.*, vol. 84, pp. 164-180, 1996.
- [11] S. T. Shipley, D. H. Tracy, E. W. Eloranta, J. T. Trauger, J. T. Sroga, F. L. Roesler, and J. A. Weinman, "High spectral resolution lidar to measure optical-scattering properties of atmospheric aerosols .1. theory and instrumentation," *Applied Optics*, vol. 22, pp. 3716-3724, 1983.
- [12] J. T. Sroga, E. W. Eloranta, S. T. Shipley, F. L. Roesler, and P. J. Tryon, "High spectral resolution lidar to measure optical-scattering properties of atmospheric aerosols .2. calibration and data-analysis," *Applied Optics*, vol. 22, pp. 3725-3732, 1983.
- [13] F. F. Hall and H. Y. Ageno, "Absolute calibration of a Laser system for atmospheric probing," *Applied Optics*, vol. 9, pp. 1820-&, 1970.

## REFERENCES - Continued

- [14] J. A. Reagan, J. D. Spinhirne, T. V. Bruhns, and R. L. Peck, "Digital detector for monitoring lidar output energy," *Rev. Sci. Instrum.*, vol. 47, pp. 1527-1530, 1976.
- [15] E. W. Barrett and O. Ben-Dov, "Application of the lidar to air pollution measurements," *J. Appl. Meteorol.*, vol. 6, pp. 500-515, 1967.
- [16] P. B. Russell, T. J. Swissler, and M. P. McCormick, "Methodology for error analysis and simulation of lidar aerosol measurements," *Applied Optics*, vol. 18, pp. 3783-3796, 1979.
- [17] T. W. Cooley and J. A. Reagan, "Calibration of 1064 nm channel of LITE and other uses of ocean surface returns," *Proc. IGARSS'93, IEEE Publication 93CH3294-6*, vol. 2, pp. 869-871, 1993.
- [18] T. W. Cooley and J. A. Reagan, "Calibration of 1064 nm channel of LITE using playa surface returns," *Proc. IGARSS' 95, IEEE Publication 95CH35770*, vol. 3, pp. 2326-2328, 1995.
- [19] J. A. Reagan, H. Liu, and T. W. Cooley, "LITE surface returns: assessment and application, advances in atmospheric remote sensing with lidar," *Advances in Atmospheric Remote Sensing with Lidar -selected papers from 18th ILRC (A. Ansmann, R. Neuber, P. Rairoux and U. Wandinger, Eds.)*, Springer-Verlag, Berlin, Germany, pp. 177-180, 1997.
- [20] A. T. Young, "Rayleigh-scattering," *Applied Optics*, vol. 20, pp. 533-535, 1981.
- [21] A. T. Young, "Revised depolarization corrections for atmospheric extinction," *Applied Optics*, vol. 19, pp. 3427-3428, 1980.
- [22] A. T. Young, "On the rayleigh-scattering optical depth of the atmosphere," *Journal of Applied Meteorology*, vol. 20, pp. 328-330, 1981.
- [23] A. T. Young, "Rayleigh-scattering," *Physics Today*, vol. 35, pp. 42-48, 1982.
- [24] E. J. McCartney, *Optics of the atmosphere, scattering by moleculars and particles*, 1st ed. New York: Wiley, 1976.
- [25] A. Bucholtz, "Rayleigh-scattering calculations for the terrestrial atmosphere," *Applied Optics*, vol. 34, pp. 2765-2773, 1995.
- [26] *Hand Book of Geophysics and the Space Environment*: Air Force Geophysics Lab, Air Force System Command, U.S. Air Force.
- [27] P. M. Teillet, "Rayleigh optical depth comparisons from various sources," *Applied Optics*, vol. 29, pp. 1897-1900, 1990.

## REFERENCES - Continued

- [28] R. Penndorf, "Tables of the refractive index for standard air and the rayleigh scattering coefficient for the spectral region between 0.2 and 20.0-Mu and their application to atmospheric optics," *Journal of the Optical Society of America*, vol. 47, pp. 176-182, 1957.
- [29] B. Edlen, "The dispersion of standard air," *Journal of the Optical Society of America*, vol. 43, pp. 339-344, 1953.
- [30] *U.S. Standard Atmosphere 1962*. Washington, D. C.: U.S. Government Printing Office, 1962.
- [31] L. Elterman, "Atmospheric attenuation model, in the ultraviolet, the visible, and the infrared windows for altitudes to 50 km," *Environ. Res. Paper 46*, 1964.
- [32] L. Elterman, "UV, visible, and IR attenuation for altitudes to 50 km," *AFGL-68-0158*, 1968.
- [33] W. A. Margraf and M. Griggs, "Aircraft measurements and calculations of the total downward flux of solar radiation as a function of altitude," *J. Atmos. Sci.*, vol. 26, pp. 469-476, 1969.
- [34] F. X. Kneizys, E. P. Shettle, W. O. Gallery, J. H. Chetwynd, J. Abreu, L. W., J. E. A. Selby, R. W. Fenn, and R. A. McClatchey, "Atmospheric transmittance/rediance: computer code LOWTRAN 5," *AFGL-TR-80-0067*, 1980.
- [35] F. X. Kneizys, E. P. Shettle, W. O. Gallery, J. H. Chetwynd, J. Abreu, L. W., J. E. A. Selby, S. A. Clough, and R. W. Fenn, "Atmospheric transmittance/rediance: compute code LOWTRAN 6," *AFGL-TR-83-0178*, 1983.
- [36] F. X. Kneizys, E. P. Shettle, J. Abreu, L. W., J. H. Chetwynd, J. Anderson, G. P., W. O. Gallery, J. E. A. Selby, and S. A. Clough, "Users Guide to LOWTRAN 7," *AFGL-TR-88-0177*, 1988.
- [37] D. V. Hoyt, "Redetermination of rayleigh optical depth and its application to selected solar-radiation problems," *Journal of Applied Meteorology*, vol. 16, pp. 432-436, 1977.
- [38] *U.S. Standard Atmosphere Supplement 1966*. Washington, D. C.: U.S. Government Printing Office, 1966.
- [39] C. Frohlich and G. E. Shaw, "New determination of rayleigh-scattering in the terrestrial atmosphere," *Applied Optics*, vol. 19, pp. 1773-1775, 1980.

## REFERENCES - Continued

- [40] B. Edlen, "The refractive index of air," *Meteorology*, vol. 2, pp. 71-80, 1966.
- [41] J. F. Potter, "Two-frequency lidar inversion technique," *Appl. Opt.*, vol. 26, pp. 1250-1256, 1987.
- [42] J. Ackermann, "Two-wavelength lidar inversion algorithm for a two-component atmosphere," *Appl. Opt.*, vol. 36, pp. 5134-5143, 1997.
- [43] J. Ackermann, "Two-wavelength lidar inversion algorithm for a two-component atmosphere with variable extinction-to-backscatter ratios," *Appl. Opt.*, vol. 37, pp. 3164-3171, 1998.
- [44] J. Ackermann, "Analytical solution of the two-frequency lidar inversion technique," *Applied Optics*, vol. 38, pp. 7414-7418, 1999.
- [45] D. G. Collis and M. R. Wells, *Monte Carlo codes for the study of light transport*, vol. 1 and 2 RRA-T54. Fort Worth, Tex: Radiation Research Associates Inc., 1965.
- [46] G. N. Plass and G. W. Kattawar, "Reflection of light pulses from clouds," *Applied Optics*, vol. 10, pp. 2304-&, 1971.
- [47] K. E. Kunkel, "Monte Carlo analysis of multiply scattered lidar returns," in *Dept. of Meteorology*. Madison: University of Wisconsin, 1974, pp. 91.
- [48] J. A. Weinman, "Effects of multiple-scattering on light-pulses reflected by turbid atmospheres," *Journal of the Atmospheric Sciences*, vol. 33, pp. 1763-1771, 1976.
- [49] G. B. Rybicki, "Searchlight problem with isotropic scattering," *Journal of Quantitative Spectroscopy & Radiative Transfer*, vol. 11, pp. 827-&, 1971.
- [50] C. M. R. Platt, "Remote sounding of high clouds .3. Monte-Carlo calculations of multiple-scattered lidar returns," *Journal of the Atmospheric Sciences*, vol. 38, pp. 156-167, 1981.
- [51] J. A. Reagan, X. Wang, and M. T. Osborn, "Spaceborne lidar calibration from cirrus and molecular backscatter returns," *IEEE Transactions on Geoscience and Remote Sensing*, vol. 40, pp. 2285-2290, 2002.
- [52] J. A. Reagan, X. Wang, and H. Fang, "LITE aerosol retrievals revisited in support of CALIPSO and GLAS," *Proc. IGARSS'02 Symposium (IEEE)*, vol. 3, pp. 1379-1381, 2002.
- [53] J. A. Reagan and D. M. Winker, "PICASO-CENA: Combined active-passive sensing from space," *Proc. IGARSS'99 Symposium (IEEE)*, pp. 240-242, 1999.

## REFERENCES - Continued

- [54] J. D. Spinhirne, "Lidar clear atmosphere multiple-scattering dependence on receiver range," *Applied Optics*, vol. 21, pp. 2467-2468, 1982.
- [55] J. Ackermann, P. Volger, and M. Wiegner, "Significance of multiple scattering from tropospheric aerosols for ground-based backscatter," *Appl. Opt.*, vol. 38, pp. 5195-5201, 1999.
- [56] C. Catrall, "Variability of aerosol lidar, backscatter and extinction ratios of key aerosol types derived from selected AERONET locations," *Journal of Geophysical Research-Atmospheres*, 2004.
- [57] B. N. Holben, T. F. Eck, I. Slutsker, D. Tanre, J. P. Buis, A. Setzer, E. Vermote, J. A. Reagan, Y. J. Kaufman, T. Nakajima, F. Lavenu, I. Jankowiak, and A. Smirnov, "A federated instrument network and data archive for aerosol characterization," *Remote Sensing of the Environment*, vol. 66, pp. 1-16, 1998.
- [58] S. Twomey, *Atmospheric Aerosols*. New York: NY:Elsevier, 1977.
- [59] G. Mie, "A contribution to the optics of turbid media, especially colloidal metallic suspensions," *Ann. Physik*, vol. 25, pp. 377-445, 1908.
- [60] D. Deirmendjian, *Electromagnetic scattering on spherical polydispersions*. New York: American Elsevier Publishing Co., Inc., 1969.
- [61] P. A. Davis, "Analysis of lidar signatures of cirrus clouds," *Applied Optics*, vol. 8, pp. 2099-&, 1969.
- [62] W. Hitschfeld and J. Bordan, "Errors inherent in the radar measurement of rainfall at attenuating wavelengths," *Journal of Meteorology*, vol. 11, pp. 58-67, 1954.
- [63] W. B. Johnson and E. E. Uthe, "Lidar study of keystone stack plume," *Atmospheric Environment*, vol. 5, pp. 703-&, 1971.
- [64] W. Viezee, E. E. Uthe, and R. T. H. Collis, "Lidar observations of airfield approach conditions: An exploratory study," *J. Appl. Meteorol*, vol. 8, pp. 274-283, 1969.
- [65] F. G. Fernald, "Analysis of atmospheric lidar observations - some comments," *Applied Optics*, vol. 23, pp. 652-653, 1984.
- [66] J. D. Klett, "Stable analytical inversion solution for processing lidar returns," *Applied Optics*, vol. 20, pp. 211-220, 1981.

## REFERENCES - Continued

- [67] F. G. Fernald, B. M. Herman, and J. A. Reagan, "Determination of aerosol height distributions by lidar," *Journal of Applied Meteorology*, vol. 11, pp. 482-489, 1972.
- [68] J. A. Ferguson and D. H. Stephens, "Algorithm for inverting lidar returns," *Applied Optics*, vol. 22, pp. 3673-3675, 1983.
- [69] H. G. Hughes, J. A. Ferguson, and D. H. Stephens, "Sensitivity of a lidar inversion algorithm to parameters relating atmospheric backscatter and extinction," *Applied Optics*, vol. 24, pp. 1609-1613, 1985.
- [70] Measures, *Laser Remote Sensing Fundamentals and Applications*. Malaba, Florida: Krieger Publishing Company, 1992.
- [71] B. Hunt, "Lidar Instrument Overview," Science Team Meeting, NASA LaRC, Hampton August 1, 2001.
- [72] M. T. Osborn, "Calibration of LITE data," *Proc. 19<sup>th</sup> International Laser Radar Conference*, pp. 245-247, 1998.
- [73] F. Cairo, G. D. Donfrancesco, A. Adriani, L. Pulvirenti, and F. Fierli, "Comparison of various linear depolarization parameters measured by lidar," *Appl. Opt.*, vol. 38, pp. 4425-4432, 1999.
- [74] M. T. Osborn, "An operational spaceborne lidar calibration algorithm for 1064 nm," *Proc. 21<sup>th</sup> Intl. Laser Radar Conference*, pp. 791-794, 2002.
- [75] P. Yang and K. N. Liou, "Finite-difference time domain method for light scattering by small ice crystals in three-dimensional space," *Journal of the Optical Society of America a-Optics Image Science and Vision*, vol. 13, pp. 2072-2085, 1996.
- [76] P. Yang and K. N. Liou, "Geometric-optics-integral-equation method for light scattering by nonspherical ice crystals," *Applied Optics*, vol. 35, pp. 6568-6584, 1996.
- [77] R. F. Pueschel and J. M. Livingston, "Aerosol spectral optical depths - jet fuel and forest-fire smokes," *Journal of Geophysical Research-Atmospheres*, vol. 95, pp. 22417-22422, 1990.
- [78] D. L. Hlavka, "personal communication for the ESSP3 lidar algorithm peer review." Hampton, VA, 2001.

## REFERENCES - Continued

- [79] C. Y. She, "Spectral structure of laser light scattering revisited: bandwidths of nonresonant scattering lidars," *Appl. Opt.*, vol. 40, pp. 4875-4884, 2001.
- [80] G. Tenti, C. D. Boley, and R. C. Desai, "On the kinetic model description of Rayleigh-Brillouin scattering from molecular gases," *Can. J. Phys.*, vol. 52, pp. 285-290, 1974.
- [81] S. Chandrasekhar, *Radiative Transfer*. New York: Dover, 1960.
- [82] W. Heller and M. Nakagaki, "Light scattering of spheroids. III. Depolarization of the scattered light," *J. Chemical Physics*, vol. 61, pp. 3619-3621, 1974.
- [83] Y. Beers, *Introduction to the Theory of Error*. Mass.: Addison-Wesley, Reading, 1953.
- [84] P. R. Bevington, *Data Reduction and Error Analysis for the Physical Sciences*. New York: McGraw-Hill, 1969.
- [85] J. Rosen and V. A. Ivanov, "Stratospheric aerosols," *Aerosol Effects on Climate*, pp. 304, 1993.
- [86] T. Deschler, D. J. Hofmann, B. I. Johnson, and W. R. Rozier, "Balloonborne measurements of the Pinatubo aerosol size and volatility at Laramie, Wyoming, during the summer of 1991," *Geophys. Res. Lett.*, vol. 19, pp. 199-202, 1992.
- [87] R. F. Pueschel, J. M. Livingston, G. V. Ferry, and T. E. DeFelice, "Aerosol abundances and optical characteristics in the Pacific basin free troposphere," *Atmos. Environ.*, vol. 28, pp. 951-960, 1994.
- [88] G. S. Kent, C. R. Trepte, K. M. Skeens, and D. M. Winker, "LITE and SAGE II measurements of aerosols in the southern hemisphere upper troposphere," *Journal of Geophysical Research*, vol. 103(D15), pp. 19111-19127, 1998.
- [89] V. M. Karyampudi and T. N. Carlson, "Analysis and numerical simulations of the Saharan air layer and its effects on easterly wave disturbances," *J. Atmos. Sci.*, vol. 45, pp. 3102-3136, 1988.
- [90] J. A. Reagan, X. Wang, C. Cattrall, and K. J. Thome, "Spaceborne Lidar Aerosol Retrieval Approaches Based on Aerosol Model Constraints," *CDProc. IGARSS 2004 Symposium (IEEE)*, 2004.
- [91] O. Dubovik and M. D. King, "A flexible inversion algorithm for retrieval of aerosol optical properties from Sun and sky radiance measurements," *Journal of Geophysical Research-Atmospheres*, vol. 105, pp. 20673-20696, 2000.

## REFERENCES - Continued

- [92] J. A. Reagan, K. J. Thome, and D. M. Powell, "Lidar aerosol ratio: measurements and models," *Proc. IGARSS'2001 Symposium (IEEE)*, pp. 84-87, 2001.
- [93] J. A. Reagan and X. Wang, "LITE aerosol retrievals at 1064 nm with improved aerosol retrieval approaches in support of CALIPSO," *Proc. IGARSS'03 Symposium (IEEE)*, vol. 3, pp. 1531-1533, 2003.
- [94] P. Volger, Z. Y. Liu, and N. Sugimoto, "Multiple scattering simulations for the Japanese space lidar project ELISE," *IEEE Transactions on Geoscience and Remote Sensing*, vol. 40, pp. 550-559, 2002.
- [95] D. M. Winker, "Multiple scattering models and effects." Williamsburg, VA: The CALIPSO Algorithm Workshop & Science Team Meeting, 2003.